Mobility and Recombination Dynamics of Charges in Low-Dimensional Van Der Waals Materials

Bhaskar, Prashant

DOI
10.4233/uuid:fc706f7e-2c02-4e1f-b9a7-691d41293a6c

Publication date
2019

Document Version
Final published version

Citation (APA)
Bhaskar, P. (2019). *Mobility and Recombination Dynamics of Charges in Low-Dimensional Van Der Waals Materials*. [Dissertation (TU Delft), Delft University of Technology]. https://doi.org/10.4233/uuid:fc706f7e-2c02-4e1f-b9a7-691d41293a6c

Important note
To cite this publication, please use the final published version (if applicable).
Please check the document version above.

Mobility and Recombination Dynamics of Charges in Low-Dimensional van der Waals Materials

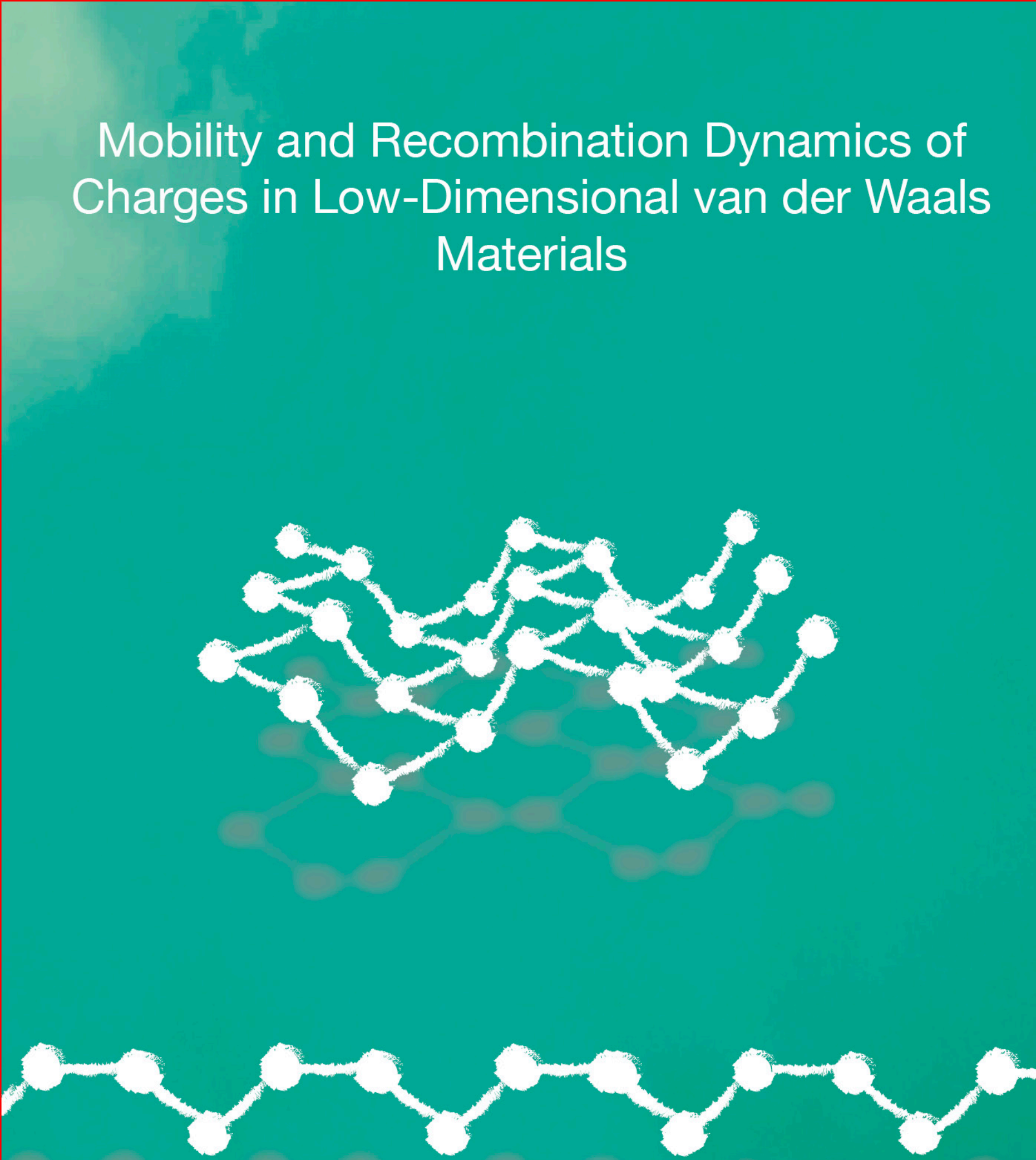

Prashant Bhaskar

Mobility and Recombination Dynamics of Charges in Low-Dimensional van der Waals Materials

Mobility and Recombination Dynamics of Charges in Low-Dimensional van der Waals Materials

Dissertation

for the purpose of obtaining the degree of doctor
at Delft University of Technology
by the authority of the Rector Magnificus prof. dr. ir. T. H. J. J. van der Hagen
chair of the Board for Doctorates
to be defended publicly on
Tuesday 28 May 2019 at 10:00 AM

by

Prashant BHASKAR
Master of Science (MS) in Physics
Indian Institute of Science Education and Research, Pune, India
born in Patna, India

This dissertation has been approved by the promoter:

Prof. dr. L. D. A. Siebbeles

Composition of the doctoral committee:

Rector Magnificus,	chairperson
Prof. dr. L. D. A. Siebbeles	Delft University of Technology, promoter

Independent members:

Prof. dr. P. Dorenbos	Delft University of Technology
Prof. dr. W. J. Buma	University of Amsterdam
Prof. dr. P. Schall	University of Amsterdam
Dr. E. L. von Hauff	Vrije Universiteit Amsterdam
Prof. dr. F. M. Mulder	Delft University of Technology
Dr. F. C. Grozema	Delft University of Technology

This research work was financially supported by *The Netherlands Organisation for Scientific Research (NWO)*.

Printed by Ridderprint BV, The Netherlands

ISBN: 978-94-6375-413-2

Graphic designed by the author

An electronic version of this dissertation is available at http://repository.tudelft.nl

Confidence and hard work is the best
medicine to kill the disease called failure.
It will make you a successful person.
Dr. A.P.J. Abdul Kalam

Dedicated to my family.

Contents

1. Introduction

Solid state materials can be classified into three categories, namely metals, insulators and semiconductors. Metals, such as gold, silver and copper, are known for their conductive properties due to the presence of abundant free electrons, which can move under the influence of an external electric field resulting into a net current. In contrast to metals, insulators, e.g. glass, do not have free electrons to conduct electricity under an external electric field. Interestingly, a class of materials known as semiconductors, such as silicon and germanium show both properties, which means it can conduct electricity upon external excitation leading to generation of free charges, while, it can act as an insulator in absence of an external excitation.

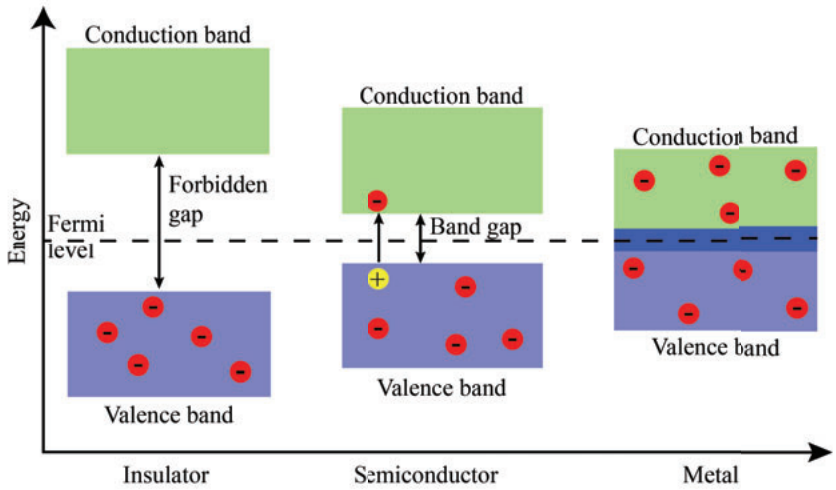

Figure 1.1 Schematic energy band diagram depicting differences in conduction band and valence band in insulators, semiconductors and metals.

In terms of energetic bands (see figure 1.1), in insulators the conduction band and valence band are separated by a large forbidden energy gap, which cannot be readily overcome by external (optical) excitations. In metals, the conduction band is partly filled or the conduction band and valence band overlap with each other resulting in availability of mobile free charges. In semiconductors, the energy band gap between conduction band and valence band is rather small as compared to insulators, and this energy gap is comparable to energies of photons in the range of near infrared *via* visible to near ultraviolet.

1.1 Semiconductors

As briefly described above, semiconductors possess conducting properties between those of metals and insulators. These materials can be classified into

elemental as well as compound semiconductors. Silicon, germanium, black phosphorus, tellurium and selenium are examples of elemental semiconductors, while gallium arsenide, zinc sulphide and zinc selenide are examples of compound semiconductors.

Furthermore, semiconductors can also be classified in terms of the presence of external impurities or dopants. Intrinsic semiconductors are materials with no external impurity or dopant. Extrinsic semiconductors contain impurities or controlled amounts of a specific dopant, and consequently the densities of electrons and holes are different from the intrinsic charge carrier concentration. The intrinsic electron and hole concentration in a bulk (or three-dimensional) semiconducting material n_i^{3D} is given by

$$n_i^{3D} = \sqrt{\frac{1}{2}\left(\frac{m_e^* m_h^* k_B^2 T^2}{\pi^2 \hbar^4}\right)^{3/2}} \exp\left[-\frac{E_g}{2k_B T}\right], \qquad (1.1)$$

where m_e^* and m_h^* are the effective masses of electrons and holes, k_B is the Boltzmann constant, T is the temperature and E_g is the bandgap of the semiconductor.[1]

Semiconducting materials are of huge interest due to applications in transistors, computers, lasers and photovoltaics including solar cells. The most widely used semiconductor material for most of these applications is silicon. Apparently, even being ubiquitously accepted for most of the applications, silicon does possess certain limitations, for instance, in solar cell applications. It has been used in solar cells for decades, but the efficiency of the power conversion of the solar radiation to usable electricity in most common commercially available solar cells is just around 8 % for amorphous silicon cells and from 14 % to 19 % for multicrystalline silicon cells.[2] Few of the various limiting factors leading to low power conversion efficiency in silicon cells are low light absorption cross-section, limited electron (hole) mobility and the narrow limit of energy harvest from the broad solar spectrum. According to the Shockley-Queisser limit, which takes into consideration the various losses e.g. charge carrier recombination and spectrum losses, the maximum efficiency of a solar cell with a band gap of 1.1 eV is estimated to be 30 %.[3]

However, this limit can further be increased with the process of carrier multiplication, where a photon of energy higher than the band-gap can be used to effectively generate two or multiple pairs of charge carriers across the band gap, thus reducing the loss of energy into thermal relaxation.[4-5] This process has been studied in nanostructures and superlattices of lead chalcogenides[4, 6-10] as well as cadmium chalcogenides[11] and recently, van der Waals materials[5] have shown a prospective candidature for carrier multiplication studies and applications.

Comparatively, van der Waals materials exhibit very interesting properties covetous for optoelectronic and photovoltaic application, e.g. monolayer black phosphorus (BP) exhibits a charge carrier mobility of the order 10^4 $cm^2V^{-1}s^{-1}$,[12] which is almost 7, and $10^3 - 10^4$ fold higher than the mobility of electrons in crystalline Si[13] and amorphous Si,[14] respectively. A material with high charge carrier mobility would exhibit possibility of faster collection of free charges by the electrodes in a solar cell, thus enhancing the overall power-conversion efficiency. The combination of possibility of carrier multiplication, high charge mobility and high absorption cross-section[15-16] makes van der Waals materials a prospective material for future generation efficient solar cells.

Another application of semiconductors in modern day devices is transistors, where Si is extensively used as the core material. These transistors are integral part of integrated circuits (ICs), ubiquitously used in digital electronics. As per the Moore's law and recent developments in semiconductor industry, the rate of doubling of transistors in an IC with time will saturate and the size of future generation transistors can no longer be reduced to fabricate either equally or better performing transistors as the fundamental barrier of the size would soon be approached for lithographically made chips. Therefore, 1D atomic chains with high intrinsic charge carrier mobility can be a good replacement for these applications as well as for use in nano-electronic devices. Interestingly, atomic chains of 1D van der Waals materials can be obtained by liquid exfoliation, which would be economically preferable over lithographical production.

Therefore, in-line with the demand of future-generation electronic applications, e.g. in transistors and solar cells, van der Waals materials exhibit potential for application in future generation devices and thus it is important to study their fundamental properties.

1.2 Van der Waals Materials

Van der Waals Materials are layered materials, where the extended crystalline sheets or chains of covalently bound elements are held together by weak van der Waals forces. These stacked chains or sheets can be separated by exfoliation techniques, which lead to modification of their optical and electronic properties.

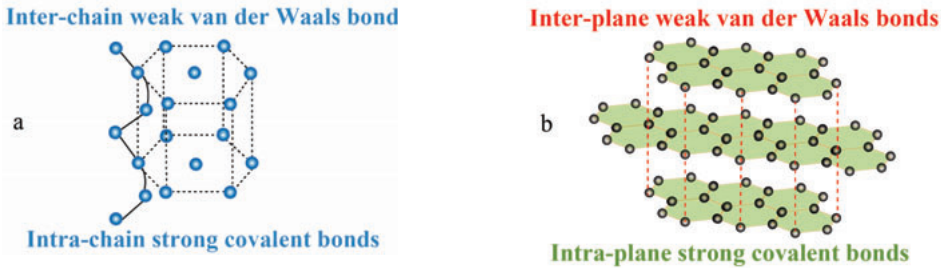

Figure 1.2 Schematic structures of a 1D (a) and 2D (b) van der Waals material.

The discovery of graphene, which exhibits exceptionally high carrier mobilities,[17-19] led to the exploration of more layered materials with a band gap and consequently semiconducting properties, unlike graphene. Fortunately, a plethora of materials are available which fall in the category of layered 2D and 1D materials. Among the 2D materials, transition-metal dichalcogenides (TMDs) include a number of semiconducting materials possessing band gaps in the range from 0.5 eV to 3 eV.[20] Other well-known 2D semiconductors belong to the III-VI and BP family. Some materials from these families are tabulated in Table 1.1.

Family	*Semiconducting materials*
TMDs	MoS_2, WS_2, SnS_2, ReS_2, $SnSe_2$, $ReSe_2$, *etc*.
III-VI	InSe, GaS, *etc*.
BP	P, SnS, SnSe, *etc*.

Table 1.1 Examples of layered 2D materials from various families of 2D van der Waals materials.

Similarly, among 1D van der Waals materials, two of the most widely known elemental van der Waals materials are trigonal selenium (Se)[21-25] and trigonal tellurium (Te).[25-29]

1.3 Low-Dimensional Semiconducting Materials

In a bulk or three-dimensional system, the electrons and holes are free to move in all the three dimensions while in low-dimensional materials, their degree of freedom is restricted in 1-3 dimensions. A material with restriction along one-dimension results into a two-dimensional material with degree of freedom along two dimensions. Similarly, a material with restriction along two-dimensions results into a one-dimensional system and a material with restriction along three dimensions results into a zero-dimensional system. This restriction in charge carrier movement along various dimensions can give rise to quantum confinement effects, which affect the electronic and optical properties of the material.

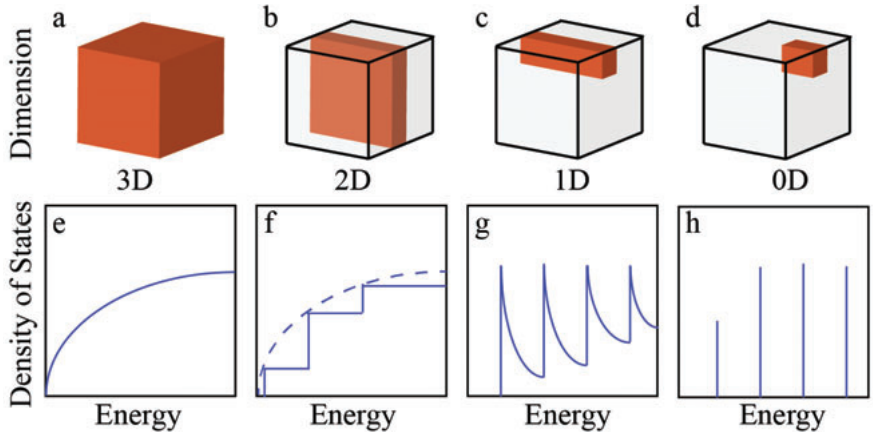

Figure 1.3 The relation between the density of electronic states (e, f, g, h) in 3D, 2D, 1D and 0D materials (a, b, c, d).

As a consequence of quantum confinement, the electronic band properties of the semiconducting materials are changed and this enables one to engineer their electronic and optical properties by changing dimensionality, shape and size. Changing dimensions of a semiconductor has direct influence on the energetic bands, their separation and the density of states (DOS) as a function of energy. Figure 1.3 depicts that the electronic density of states depends strongly on the dimensionality of the system. For instance, in a 3D system, the DOS in an electronic band increases with energy (see figure 1.3e). While, in 2D and 1D systems, the DOS of the electronic sub-band remains constant (see figure 1.3f) and decreases (see figure 1.3g) with energy, respectively. For a 0D system, the DOS becomes discrete (see figure 1.3h), similar to atomic or molecular energy levels.

1.4 Optoelectronic Properties and Applications

Semiconductors are of great interest due to their applications in devices like light-emitting diodes (LEDs), solar cells, transistors, photovoltaics and so on. In these aforesaid applications or devices, the underlying fundamental particles that govern their applicability are charge carriers, which can be either free electrons and holes or bound electrons and holes, known as excitons. Depending upon the types of applications, the performance of optoelectronic devices broadly depends upon two factors, which are the mobility of charge carriers and the recombination dynamics of charges, e.g. in a solar cell or transistor, a material with higher charge carrier mobility would result into better performance of the device, while in a LED, a material with high radiative recombination would lead to better performance.

In this thesis, we focus on studying fundamental properties of free charges, which are the mobility and recombination dynamics in van der Waals materials, using a contactless method. The mobility (μ) is defined as the ability of a free electron (or hole) to move with an average velocity (ν_{d}) through a semiconductor in the presence of an electric field (E), as shown below.

$$\mu = \frac{\nu_{\mathrm{d}}}{E} \tag{1.2}$$

Since neither mobility nor drift velocity are a directly measurable entity, these values can be estimated experimentally by measuring electrical conductivity (σ), which is directly proportional to the density of free charges (n or p) and the elementary charge (e) in SI units, as shown below.

$$\sigma = e\left[\mu_n n + \mu_p p\right] \tag{1.3}$$

The transient electrical conductivity studies in this thesis were done using a contactless microwave technique, as discussed in section 1.5, whereas the relation between transient conductivity and transient charge densities of electrons and holes is described by equation (1.5).

1.5 Pulse-Radiolysis Time Resolved Microwave Conductivity (PR-TRMC)

Pulse-radiolysis is a process where a sample is irradiated with pulses of high-energy electrons. The high-energy primary electrons pass through the sample without causing a net charging of the sample. These primary electrons lose a fraction of their energy to the sample yielding equal densities of electrons and

holes in the sample, which can be probed with microwaves to study the transient conductivity. A schematic diagram of the technique is shown in figure 1.4 and a detailed illustrative diagram is shown in the appendix A2.

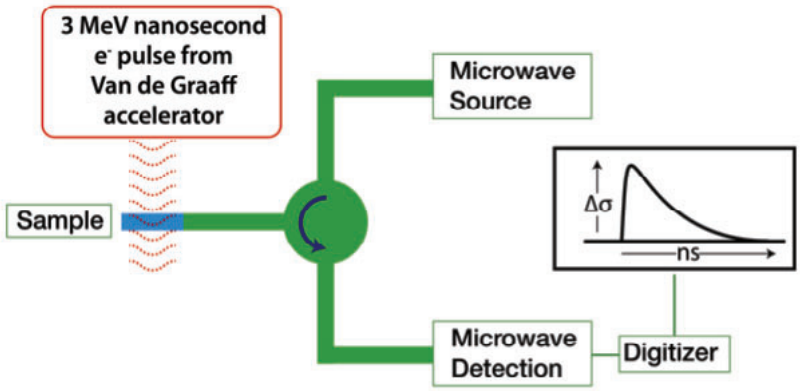

Figure 1.4 A schematic diagram of the PR-TRMC experimental set-up.

The time-resolved microwave conductivity (TRMC) technique is a contactless method used to study charge carrier mobility and decay dynamics. In the presence of the oscillating microwave field, free positive (negative) charges in a sample collectively oscillate parallel (opposite) to the field direction. The movement of charges in the external field results into absorption of incident microwave power, causing a reduction in the field amplitude transmitted through the sample, as shown in figure 1.5.

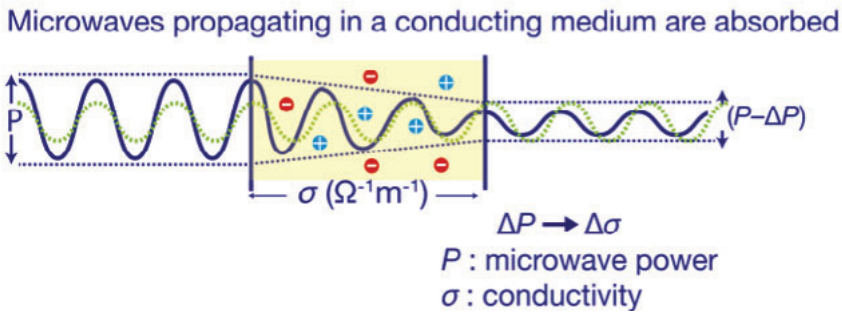

Figure 1.5 Microwave power absorbed during passing through a conducting medium.

The reduced microwave power is directly proportional to the change in conductivity of the sample. The proportionality constants as shown in equation (1.4) are called “sensitivity factors”, which depend upon the properties of

material, microwave cell dimensions and heterogeneity of the sample, as described elsewhere.[30-32] The change in the conductivity is directly proportional to the transient densities of charges and their mobility. The mobility is an intrinsic property, which depends upon the shape, size, dimensionality and electronic band-structure of the materials. The aforementioned relations are shown in the following equations.

$$\frac{\Delta P(t)}{P} = -AB\Delta\sigma(t) \tag{1.4}$$

$$\Delta\sigma(t) = e\left[\mu_n \Delta n(t) + \mu_p \Delta p(t)\right] \tag{1.5}$$

In the above equations, $\Delta P(t)$ is the transient change in the microwave power, P is the total microwave power originating from the diode gun, $\Delta\sigma(t)$ is the transient microwave conductivity, A and B are the sensitivity factors, e is the elementary charge, μ_n and μ_p are the electron and hole mobility, Δn and Δp are the transient densities of electrons and holes in the sample.

1.6 Decay Kinetics

From equation (1.5), it is understood that the mobility of free charges, their time-dependent densities and decay kinetics can be experimentally studied using the PR-TRMC technique. Upon external excitation of a semiconductor using optical excitation or high-energy particle irradiation, charge carriers in the valence band are promoted to a higher energy state in the conduction band. If the excitation energy is equal to the band gap, the excited electron is promoted from the top of the valence band to the bottom of the conduction band. If the energy is higher than the band gap, electrons can be excited higher in the conduction band and holes may be produced deeper in the valence band. In the latter case, the excess energy of the charges may be released in the form of heat *via* thermalization (i.e. by phonon emission).

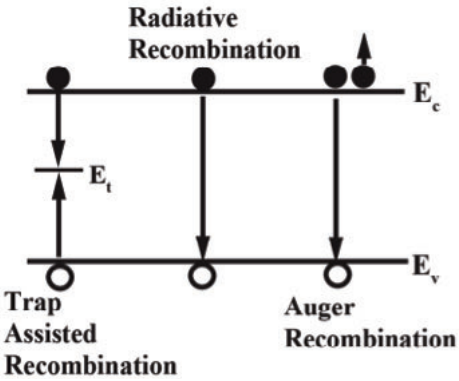

Figure 1.6 Illustrative diagram depicting three major recombination pathways of charge carriers in a semiconductor.

Once the charges are thermalized to the band-edge, they recombine either radiatively or non-radiatively. In radiative process, the charges annihilate each other by emitting a photon with energy equal to the band gap. In a non-radiative process, the charges recombine at localized trap states in the band gap or they recombine and transfer their energy to a third charge, be it an electron or hole. The Shockley-Read-Hall (SRH)[1, 33-34] model best describes the former process and the latter process is known as Auger Recombination.[1] An illustrative energy band diagram showing these processes is given in figure 1.6.

SRH recombination *via* trap sites can occur *via* four transitions, as shown in figure 1.7. The trap site can be in a neutral, negatively charged or positively charged state. The four process are:

a. Capture of an electron: An empty neutral trap state captures an electron from the conduction band
b. Emission of an electron: A negatively charged trap state emits an electron to the conduction band through thermal energy of the host lattice
c. Capture of a hole: A filled trap state captures a hole from the valence band
d. Emission of a hole: A positively charged trap state emits a hole to the valence band.

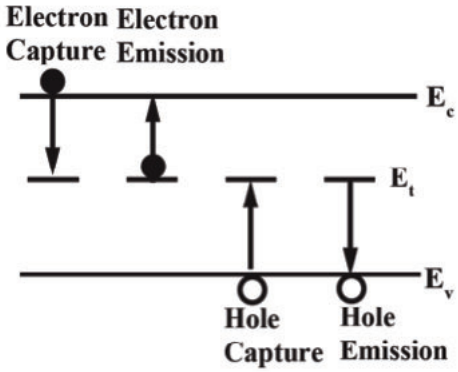

Figure 1.7 Illustrative diagram showing electron and hole capture and emission processes governing Shockley-Read-Hall recombination.

The underlying rate equation describing the SRH model is derived from the aforementioned processes using Fermi-Dirac statistics, as discussed in detail elsewhere.[1] The net SRH recombination rate is equal to

$$U = \frac{\left(np - n_i^2\right)}{\tau_{p0}\left(n + n_1\right) + \tau_{n0}\left(p + p_1\right)}, \tag{1.6}$$

where U is the net rate of electron or hole capture per unit volume. In equation (1.6), n and p are the total densities of electrons and holes, n_i is the density of intrinsic electrons and holes, n_1 and p_1 are defect parameters, τ_{n0} and τ_{p0} are the associated lifetimes of electrons and holes, which are defined as $\tau_{n0} = 1/c_{\mathrm{n}}N_{\mathrm{t}}$ and $\tau_{p0} = 1/c_{\mathrm{p}}N_{\mathrm{t}}$, where $c_{\mathrm{n}} = \sigma_{\mathrm{n}}\langle\nu_{\mathrm{th}}\rangle$ and $c_{\mathrm{p}} = \sigma_{\mathrm{p}}\langle\nu_{\mathrm{th}}\rangle$ are the electron- and hole-capture coefficients, respectively, N_{t} is the total trap density, σ_{n} and σ_{p} are the electron- and hole-capture cross-sections and $\langle\nu_{\mathrm{th}}\rangle = \left(3k_{\mathrm{B}}T/m^*\right)^{1/2}$ denotes the average thermal velocity of electrons and holes.

As mentioned above, radiative recombination is a process where an electron and hole recombine by emission of a photon, which is the inverse process of optical excitation. The rate of annihilation of electrons and holes *via* radiative recombination is directly proportional to the product of the densities of electrons and holes. Under thermal equilibrium conditions, the rate of radiative

recombination should be equal to the rate of thermal generation (G_0), which can be written as $G_0 = B_r n_i^2$, where B_r is the rate constant of radiative recombination.[1, 35] Similarly, after external excitation, the rate of radiative recombination is given by $r = B_r np$, where n and p are the densities due to external and thermal excitation, given by $n = n_i + \Delta n$ and $p = n_i + \Delta p$. Eventually, the net recombination rate can be obtained from r and G_0 as

$$U_r = r - G_0 = B_r\left(np - n_i^2\right) . \tag{1.7}$$

In an Auger recombination process the energy resulting from band-to-band recombination of electrons and holes is transferred to a third particle, which can be an electron in the conduction band or hole in the valence band. The excess energy obtained by the third particle is then lost in the form of heat. Auger recombination is an inverse process of impact-ionization, where a sufficiently energetic electron (or hole) excites an electron from the valence band to the conduction band.

The rate equation for the three-particle Auger recombination process can be written as $G_0 = \left(C_n + C_p\right)n_i^3$. Under non-equilibrium conditions, upon external excitation, the rate is $r_A = C_n n^2 p + C_p p^2 n$. Eventually, the net Auger recombination rate can be obtained from G_0 and r_A as

$$U_A = r_A - G_0 = C_n\left(n^2 p - n_i^3\right) + C_p\left(p^2 n - n_i^3\right), \tag{1.8}$$

where C_n and C_p are the capture probability coefficients when the third charged particle is either an electron or hole, respectively.
The total recombination rate results from the three abovementioned recombination processes, as described by equations (1.6), (1.7) and (1.8).

1.7 Thesis Outline

In this thesis, temperature dependent mobility and recombination pathways of free electrons and holes are studied on low-dimensional van der Waals materials. The excess free charge carriers were generated by irradiation of the sample with high-energy (3 MeV) electrons from a van de Graaff accelerator. The 3 MeV electrons

generate mobile free charge carriers in the sample, as briefly described in section 1.5 and the transient conductivity due to the latter is measured using a contactless method.

In chapter 1, we report studies of the temperature dependent mobility and charge carrier decay dynamics in black phosphorus (BP). We infer that BP is a highly efficient infrared emitter. In order to study the carrier dynamics, excess electrons and holes were generated using the pulse-radiolysis technique. The transient microwave conductivity due to the excess charges was measured as a function of time for different initial charge densities and temperatures in the range of 203 K to 373 K. A new global analysis scheme, including the treatment of intrinsic carriers is provided, which shows that the recombination dynamics in BP, a low dimensional semiconductor, is strongly influenced by the presence of intrinsic carriers. The temperature dependence of the charge mobility and charge carrier decay *via* second-order recombination is obtained from modelling of the experimental data. The combined electron and hole mobility was found to increase with temperature up to 250 K and decrease above that. Auger recombination was negligible for the studied densities of excess electron-hole pairs up to 2.5×10^{17} cm^{-3}. For this density the major fraction of the excess electrons and holes undergo radiative recombination. It is further inferred that for excess charge densities of the order 10^{18} cm^{-3} electrons and holes recombine with near unity radiative yield, which offers promising prospects for use of BP as efficient mid-infrared emitter in devices.

In chapter 2, we describe transient conductivity studies on tin disulfide (SnS_2), a two-dimensional semiconducting van der Waals material with indirect band gap. We measured the mobility, trapping and recombination dynamics of charge carriers as a function of temperature and charge density. Excess electrons and holes were generated by pulsed-irradiation with 3 MeV electrons. The charge carriers were probed by time-resolved microwave conductivity measurements. The mobility and decay pathways of the charge carriers were determined from the fits of a theoretical kinetic model including decay of charges by trapping and higher-order recombination. We found high mobilities for electrons and holes near 100 $cm^2V^{-1}s^{-1}$. The mobility decreases at higher temperature, which is typical for band-like transport. The second-order recombination rate constant is found to be thermally activated with an activation energy close to the energy difference of the direct and indirect band gap of SnS_2. This suggests that radiative recombination is a reaction-limited process occurring after promotion of electrons

from the $M-$point to the $\Gamma-$point in the conduction band.

In chapter 3, we discuss the transient conductivity studies on trigonal selenium (Se), which is a semiconducting van der Waals solid consisting of helical atomic chains of Se. We studied the mobility and decay dynamics of excess electrons and holes moving along the Se chains. Excess charge carriers were generated through pulse-radiolysis and their mobility and decay *via* trapping or recombination was studied by time-resolved microwave conductivity measurements as a function of temperature. The mobility of charge carriers along the Se chains is at least $0.5\ cm^2V^{-1}s^{-1}$ at room temperature. It was found that charges decay predominantly by trapping at defects. The appreciable mobility, together with the potential for large-scale production of Se wires by liquid exfoliation makes this material of great interest for use in nanoelectronics.

In the last chapter of this thesis, we discuss our results on trigonal tellurium (Te), which is a small band gap elemental van der Waals semiconductor. Te consists of one-dimensional helical chains of atoms, similar to Se. We study the temperature dependence of the charge carrier mobility and recombination pathways in bulk Te. Excess electrons and holes were generated through pulse-radiolysis and charge carrier dynamics were probed by time-resolved microwave conductivity measurements. A theoretical model was used to explain the experimental observations for different charge densities and temperatures. Our analysis reveals a high room temperature mobility of $190 \pm 20\ cm^2V^{-1}s^{-1}$. The mobility is thermally deactivated suggesting a band-like transport mechanism. According to our analysis, charges predominantly recombine *via* radiative recombination with a radiative yield close to 98 %, even at room temperature. The remaining charges recombine by either trap-assisted (Shockley-Read-Hall) recombination or undergo trapping to deep traps. The high mobility, near unity radiative yield and the possibility of large-scale production of atomic wires by liquid exfoliation makes Te of high potential for next-generation nanoelectronic and optoelectronic applications, including far-infrared detectors and lasers.

2. Radiatively Dominated Charge Carrier Recombination in Black Phosphorus

This chapter is based on the following work:
P. Bhaskar, A. W. Achtstein, M. J. W. Vermeulen, L. D. A. Siebbeles, *Journal of Physical Chemistry C* **2016**, *120*, 13836-13842.

2.1 Introduction

Two-dimensional nanomaterials receive much attention currently, as they have unique optical and electronic properties that offer promising prospects for their use in (opto) electronic devices.[36-38] The electronic structure,[39] carrier recombination dynamics and transport properties of these low-dimensional materials are currently in the focus of research as strong electronic confinement allows for an effective engineering and functionalization of material properties like e.g. for hydrogen generation by water splitting,[40] efficient carrier multiplication for solar cells of superior efficiency[41] or field effect transistor devices with high mobility,[42] bandwidth and on/off ratio.[43] In the last few years Black Phosphorous (BP) has entered the field of research on two-dimensional materials,[44-47] which is about hundred years after the first high pressure synthesis by Bridgman.[48] This current study investigates the recombination dynamics of charge carriers in BP by the means of electrode-less time-resolved microwave conductivity measurements.

BP has a sheet-like, puckered, orthorhombic structure due to sp^3 hybridization with an interlayer distance of 0.53 nm in bulk.[12, 49] Two-dimensional sheets of BP can be produced as thin as one atomic layer only, which is known as phosphorene.[46] The optical and electronic properties of BP can be adjusted by variation of the number of stacked layers.[43, 50] Bulk BP can be considered as a van der Waals solid consisting of stacked phosphorene sheets. BP has a direct band gap that can be tuned from 0.3 eV for bulk to 1.6 eV for a monolayer.[51-55] For bulk BP an experimental exciton binding energy of 8 meV has been reported.[49] For monolayer and few layers BP there are still relevant discrepancies of the effect of sheet thickness on the band gap and exciton binding energy from experiment and theory.[51-55] Recent studies showed high charge carrier mobilities in single and multilayer BP up to 10^4 $cm^2V^{-1}s^{-1}$, which is of great promise for application in next generation field-effect transistors.[12, 49, 52, 55-57] Apart from these findings a very high photoresponsivity[57] has been demonstrated, making BP also an interesting material for photodetectors and photovoltaics.

The dynamical response of thin BP flakes due to generation of excess charge carriers by pulsed photoexcitation has been studied recently.[58] As in single or few layers BP the electronic states are strongly dependent on the dielectric surrounding and the attachment of the sheets on each other. Hence, the electronic properties are not as well defined as in bulk BP where those effects do not occur. To understand the charge carrier dynamics in single or few layers BP, it is

necessary to understand this for bulk BP at first. Time-resolved studies of the mobility and dynamics of excess electrons and positive charges (holes) in bulk BP have not been reported yet.

The studies reported below aim to provide information on the mobility and the mechanisms of recombination of excess electrons and holes in bulk BP. Excess electrons and holes were produced by irradiation of bulk BP with high-energy (3 MeV) electron pulses[59] (see Methods Section). As in the used electron energy range of 3 MeV, the electronic stopping power is the predominant energy loss mechanism, atomic displacements and defects are not generated in contrast to ion irradiation of similar energy.[60] The mobility and decay of the excess charges were monitored by time-resolved microwave conductivity measurements (TRMC) at temperatures in the range 203 – 373 K. A global analysis in connection with a population rate equation model is used to analyze the experimental results and to obtain information about the relative importance of different electron-hole recombination mechanisms. For an excess density of the order of 10^{17} cm^{-3} electrons and holes decay predominantly radiatively *via* second-order recombination.

2.2 Experimental Methods

BP with a purity of 99.999 % was obtained from Smart Elements and used without further purification. Macroscopic grains of BP were compressed in a small sample notch in a polyether ether ketone (PEEK) sample holder in a glove box filled with nitrogen. In this way a 2 mm BP layer embedded in PEEK was formed. To avoid exposure to air the BP in the sample notch was covered with a thin film of poly(methyl methacrylate) (PMMA).

For time-resolved microwave conductivity (TRMC) measurements the sample was inserted in a K_a band (27-38 GHz) microwave waveguide so that the 20 mm long sample holder touches the endplate of the waveguide and the compressed BP layer is 4 mm apart from the endplate. Excess electron-hole pairs are produced by pulsed irradiation of the sample with 3 MeV electrons from a Van de Graaff accelerator, as described previously.[59] The incident 3 MeV electrons undergo scattering in the sample and transfer their energy by generating electron-hole pairs along their tracks. In this way, a close to uniform distribution of secondary, tertiary *etc*. electrons and holes is produced in the BP layer. The penetration depth of 3 MeV electrons is about 1.5 cm, which largely exceeds the thickness of the microwave cell (0.5 cm). Therefore, the incident 3 MeV electrons pass through

the cell without net charging of the sample. During the 3 MeV electron pulse, electron-hole pairs are generated in the BP layer with a number density per unit time, *G*, which is given by the ratio of the known energy transfer rate from the incident electrons to the sample (radiation dose) and the average energy needed for formation of an electron-hole pair.[61-63] The dose absorbed in BP (D_{BP}) was recalculated from a reference measurement for Benzene (Bz)[64] using the atomic mass (M), the density ($\rho_{\mathrm{BP}} = 2.69\ \mathrm{gcm}^{-3}$)[65] and the number of electrons per molecule or atom (N_e) in case of a monoatomic material.[66] Since in the occurring linear energy transfer regime, the absorbed dose is proportional to the total electron density in the material, the empirical relation $D_{\mathrm{BP}} = D_{\mathrm{Bz}}\left(N_{e,\mathrm{BP}}\,\rho_{\mathrm{BP}}\,M_{\mathrm{Bz}}/N_{e,\mathrm{Bz}}\,\rho_{\mathrm{Bz}}\,M_{\mathrm{BP}}\right)$ holds for the absorbed dose (D_{BP}) in BP.[66] The electron-hole pair formation energy, E_{p}, for BP was estimated using the empirical result for semiconductors of Alig *et al.*,[67] given by $E_{\mathrm{p}} = 2.73E_{\mathrm{g}} + b$ with $b = 0.5$ eV and $E_{\mathrm{g}} = 0.3\ \mathrm{eV}$[51] the band gap of bulk BP. The generated electron-hole pair density was obtained as $D_{\mathrm{BP}}/E_{\mathrm{p}}$.

The excess electrons and holes produced by irradiation of BP with an electron pulse give rise to a transient conductivity change $\Delta\sigma(t) = e[\mu_e + \mu_h]\Delta n(t)$, with e the elementary charge, μ_e(μ_h) the electron (hole) mobility and $\Delta n(t)$ the number density of excess electron-hole pairs at time t after the start of the pulse. The measured fractional change of microwave power reflected from the cell is related to the transient conductivity according to $\Delta P(t)/P = -A\Delta\sigma(t)$.[62-63] The low band gap of BP gives rise to an intrinsic conductivity, which makes it not possible to quantify the prefactor A, in contrast to non-conducting materials studied previously.[61, 63] According to what is mentioned above, the transient conductivity $\Delta\sigma(t)$ in arbitrary units is $-\Delta P(t)/P \equiv F\Delta n(t)$, with the prefactor $F = Ae[\mu_e + \mu_h]$ a relative measure of the sum of the electron and hole mobilities $[\mu_e + \mu_h]$. The temperature dependence of F reflects the dependence of $\mu_e + \mu_h$, since the dielectric constant of BP is virtually independent of temperature[68] and therefore A can be considered as an arbitrary constant.

2.3 Results and Discussion

2.3.1 Transient Microwave Conductivity due to Excess Electrons and Holes

Figure 2.1a shows the transient microwave conductivity due to excess electrons and holes generated by irradiation of the BP sample with 3 MeV electron pulses with durations as indicated and a generation rate equal to $G = (2.5 \pm 0.3) \times 10^{16}$ $cm^{-3}ns^{-1}$ (see Methods). The conductivity increases during the pulse due to charge generation and decays subsequently due to radiative and non-radiative recombination and decay. The conductivity saturates practically for the longest pulse duration of 50 ns in figure 2.1a, which is due to reaching an equilibrium between charge generation and higher-order recombination of electrons and holes. This saturation behaviour is even more clearly observed during 250 ns pulses, see figure 2.1b. The sublinear increase of the saturation level with the generation rate of electron-hole pairs is typical for decay by higher-order recombination.

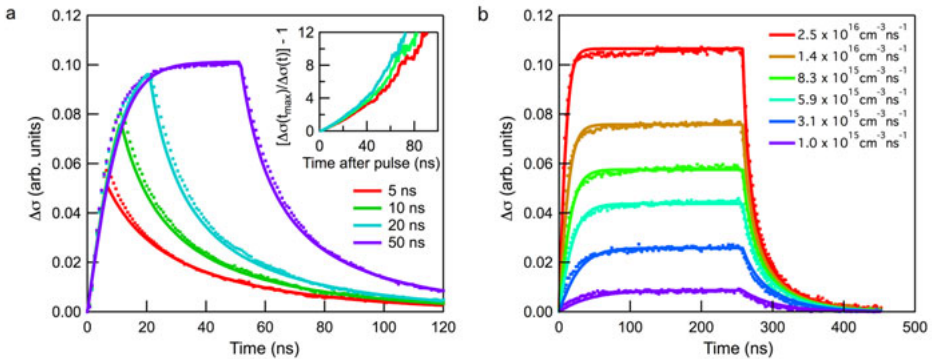

Figure 2.1 Transient microwave conductivity due to excess charge carriers in bulk BP at room temperature for different durations of the 3 MeV electron pulse as measured (dotted curves) and obtained from theoretical modelling (drawn curves). (a) Transient conductivity for a generation rate $G = 2.5 \times 10^{16}$ $cm^{-3}ns^{-1}$ for pulse durations as indicated. A saturation of the conductivity for the 50 ns pulse duration can be clearly identified. The Debye plot in the inset shows a linear behaviour on shorter time-scales, which is typical for second-order radiative recombination of electrons and holes. (b) The transient conductivity during a 250 ns pulse increases sublinearly with the generation rate in agreement with occurrence of second-order recombination.

For second-order decay with rate constant k_2 the excess density of electrons and holes at time t after the end of the 3 MeV electron pulse is given by $\Delta n(t) = \Delta n(t=0)/\left(1+\Delta n(t=0)k_2 t\right)$. The transient conductivity is proportional to the excess charge carrier density according to $\Delta\sigma(t) = e\left[\mu_e + \mu_h\right]\Delta n(t)$, with e the elementary charge and μ_e (μ_h) the electron (hole) mobility. Hence, a plot of $\left[\Delta\sigma(t_{\max})/\Delta\sigma(t)\right]-1$ versus time (Debye plot) is linear in the case of charge decay by second-order recombination. Note that $\Delta\sigma(t_{\max})$ is the end of the pulse conductivity obtained at t_{pulse}. The inset in figure 2.1a shows that such a Debye plot is linear for times up to ~40 ns after the pulse. The second-order decay is indicative for bimolecular radiative recombination of electrons and holes. The deviation from linearity in the Debye plot on longer times is due to an increasing fraction of trap-assisted recombination of excess charges, as further addressed below on the basis of theoretical modelling.

Figure 2.2 shows the transient microwave conductivity for different temperatures. The magnitude of the conductivity during the 3 MeV electron pulse first increases somewhat from low temperature to T = 253 K and then decreases at higher temperatures. This is a first indication that the charge mobility varies with temperature. The decay kinetics after the pulse varies significantly with temperature, which indicates that the temperature dependence of the electron-hole recombination processes is significant.

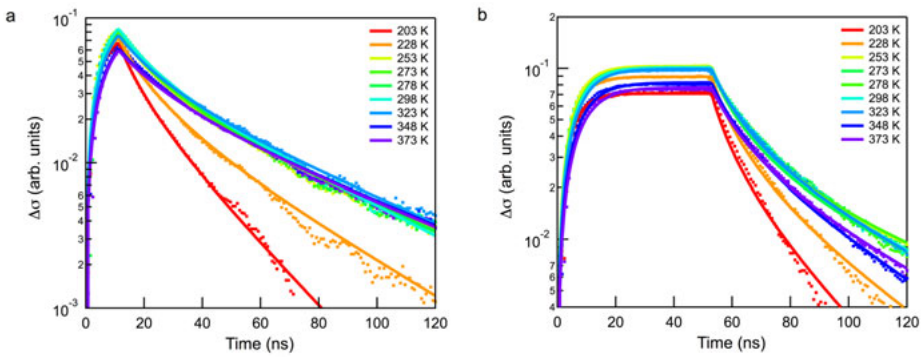

Figure 2.2 Effect of temperature on the measured transient microwave conductivity (dotted curves) and theoretical modelling (drawn curves) for pulse duration of 10 ns (a) and 50 ns (b). The electron-hole pair generation rate during the pulse is $G = 2.5\times10^{16}\ cm^{-3}ns^{-1}$.

2.3.2 Theoretical Model of Charge Carrier Dynamics

The transient microwave conductivity in figures 2.1 and 2.2 was described theoretically by taking into account generation of excess electrons and holes at equal density, $\Delta n(t)$, during the 3 MeV electron pulse with duration t_{pulse}. During and after the pulse the excess electrons and holes decay by recombination with each other or with the intrinsic electrons and holes that are assumed to be present with equal densities n_i. The intrinsic charge density is significant due to the low band gap of ~0.3 eV of BP.[49, 51-54] The time variation of the excess charge carrier density was described analogous to the work of Piprek *et al.*,[69] extended for the treatment of the intrinsic carrier densities[70] yielding

$$\frac{\mathrm{d}\Delta n(t)}{\mathrm{d}t} = G\left[\Theta(t) - \Theta\left(t - t_{\text{pulse}}\right)\right] - k_1\left[\frac{n^2(t) - n_i^2}{n(t)}\right] - k_2\left[n^2(t) - n_i^2\right] - 2k_3 n(t)\left[n^2(t) - n_i^2\right] \qquad (2.1)$$

with the total electron (hole) density $n(t) = n_i + \Delta n(t)$, assuming $n = p$. The first term on the right-hand side of equation (2.1) describes the generation of excess electrons during the 3 MeV electron pulse. The presence of the Heaviside step function, $\Theta(t)$, causes this term to be non-zero during the pulse only. Subsequent terms containing the factor n_i^2 take into account generation of electron-hole pairs by deviation from the thermodynamic equilibrium carrier density n_i through absorption of blackbody radiation, thermal excitation or impact ionization by sufficiently energetic intrinsic thermally excited charge carriers.[71]

The negative part of the second term takes into account first order charge trapping and subsequent non-radiative electron-hole recombination according to the Shockley-Read-Hall (SRH) model,[71] with an equal lifetime for electron and hole trapping, $\tau_{\text{SRH}} = 1/2k_1$, and neglecting defect parameters n_1 and p_1 (the electron and hole densities that one would have in case the Fermi energy coincides with the trap level[69]). The third term accounts for the radiative decay of an electron-hole pair with rate coefficient $k_2 = pE_{\text{g}}^2 / (k_{\text{B}}T)^{3/2}$ with p a constant independent of temperature[70, 72], k_{B} the Boltzmann constant and the band gap E_{g}

taken to be 0.3 eV.[43] The decrease of k_2 with temperature, T, can be understood as follows.[72-73] Recombining free carriers must have equal and opposite momenta, a condition that decreases in likelihood as the average thermal energy and hence the Fermi vector increases with temperature.[72]

The last term in equation (2.1) involves Auger recombination of an electron with a hole in which the band gap energy is transferred to a third charge carrier.[69, 71] Equation (2.1) was obtained by assuming that the Auger rate is equal for the third charge being an electron or a hole. The temperature dependence of the Auger rate is treated as $k_3 = r\left(k_{\mathrm{B}}T/E_{\mathrm{t}}\right)^{3/2}\exp\left[-E_t/k_{\mathrm{B}}T\right]$ with r a constant independent of temperature and a threshold energy $E_t = 1.5\,E_{\mathrm{g}}$.[70]

As BP is a bulk material consisting of two-dimensional sheets, the intrinsic charge density should be between that for two-dimensional $n_i^{2\mathrm{D}} = \left(2k_{\mathrm{B}}T/\pi\hbar^2\right)\sqrt{m_e^* m_h^*}\exp\left[-E_{\mathrm{g}}/2k_{\mathrm{B}}T\right]$ and three-dimensional $n_i^{3\mathrm{D}} = \sqrt{\left(m_e^* m_h^* k_{\mathrm{B}}^2 T^2/\pi^2\hbar^4\right)^{3/2}}\exp\left[-E_{\mathrm{g}}/2k_{\mathrm{B}}T\right]$ semiconductors.[74] The two-dimensional density was converted to a three-dimensional density to be used in equation (2.1) by dividing $n_i^{2\mathrm{D}}$ by the interlayer distance of 0.53 nm between BP sheets. The effective mass of electrons (holes), m_e (m_h), was taken from reference[49].

With these considerations the excess charge density $\Delta n(t)$ was modelled by numerically solving the differential equation (2.1) *via* a Runge-Kutta method and globally fitting to the experimental transient conductivity $\Delta\sigma(t) = e\left[\mu_e + \mu_h\right]\Delta n(t)$ in figures 2.1 and 2.2, by minimizing the chi-square deviation. The saturation level for higher pulse length (as shown in figure 2.1b) is very sensitive to the actual radiative and non-radiative rates and hence fitting also the beam current dependencies complements our global fit approach. The adjustable parameters in the fitting procedure are the temperature dependent sum of the electron and hole mobility $\mu_e + \mu_h$ in arbitrary units, the rate constants k_1 and the parameters p and r in k_2 and k_3, respectively.

2.3.3 Temperature Dependence of Charge Mobility and Decay Rate Coefficients

As can be seen in figures 2.1 and 2.2 the theoretical model of charge generation and decay reproduces the measured transient conductivity for all 3 MeV electron pulse durations, charge generation rates and temperatures considered. The fitted results for $\mu_e + \mu_h$ (in arbitrary units) and the rate coefficients k_1 and k_2 are shown in figures 2.3a-c as a function of temperature. The numerical fits were found to only agree with the experimental results for the calculated three-dimensional expression for the intrinsic charge carriers density, n_i^{3D}, which is shown in figure 2.3d.

The need to invoke the three-dimensional intrinsic charge density implies that there is relevant electronic coupling perpendicular to the phosphorene sheets in bulk BP. This observation is in line with resistance anisotropy measurements on bulk like BP, showing considerable transversal inter-sheet conductivity of BP.[49] The calculated intrinsic density of electrons and holes shown in figure 2.3d increases with temperature to a few times 10^{16} cm^{-3} for the highest temperature. The intrinsic density is small compared to the initial excess charge density, which is at least an order of magnitude higher at the end of the (*e.g.* 10 ns) 3 MeV electron pulses used to obtain the data in figures 2.1 and 2.2. Hence, recombination of excess charges with intrinsic charges is mainly relevant on longer time-scales ($>\sim 50$ ns) after the end of the 3 MeV electron pulse, when the transient conductivity and hence the excess carrier concentration has decreased an order of magnitude or more compared to its maximum value. The increasing fraction of excess electrons and holes recombining with intrinsic charges and *via* non-radiative SRH recombination on longer time-scales after the pulse agrees with the deviation of the Debye plot in figure 2.1a from a linear behaviour on longer time-scales.

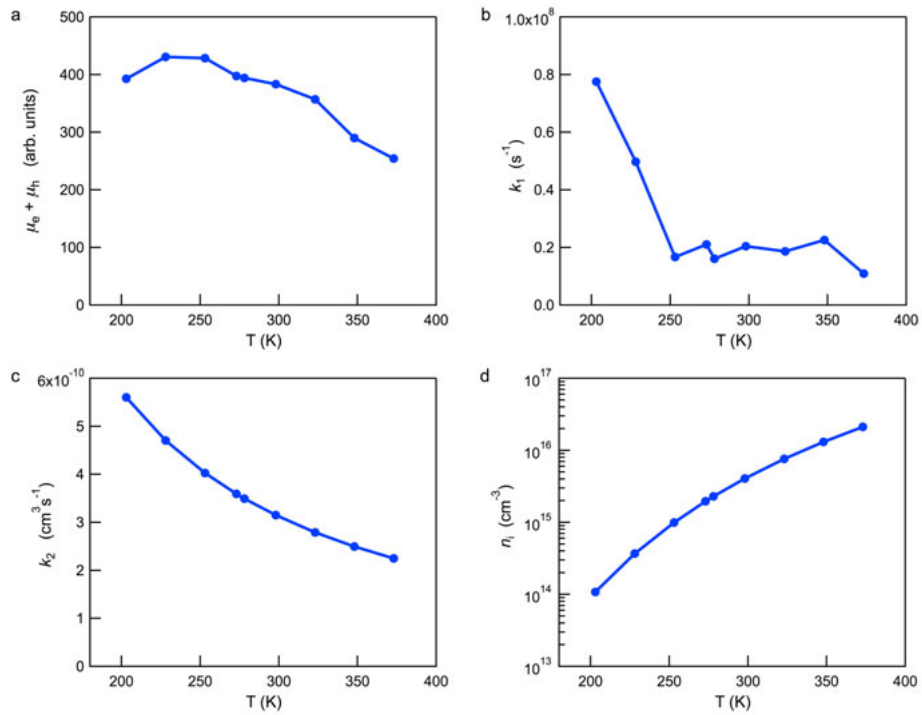

Figure 2.3 Temperature dependence of parameters in the theoretical model: (a) sum of electron and hole mobilities, (b) decay rate k_1 for trap-assisted SRH recombination, (c) radiative recombination rate k_2, and (d) intrinsic charge carrier density n_i.

Figure 2.3a shows that $\mu_e + \mu_h$ first increases with temperature up to $T \sim 250$ K and decreases for higher temperatures up to 373 K. The slight increase of the charge mobility with temperature at the lowest measured temperatures may be related to scattering on structural defects that can be surpassed by thermal activation or due to scattering on charged impurities.[70] The decrease of the mobility at higher temperatures is likely due to deformation potential scattering with acoustic phonons, yielding a temperature dependence according to $\mu_{\text{acoustic}} \propto T^{-3/2}$.[70] Polar optical phonon scattering is not possible in BP, as there are no different atoms in the BP lattice. The combined effect of different scattering processes on the mobility can be obtained from Matthiessen's rule[70] as $\mu^{-1} = \sum_m \mu_m^{-1}$ with m accounting for the different types of scattering. Hence, the scattering processes considered above result in the occurrence of a maximum mobility at intermediate temperature, in agreement with the data in figure 2.3a. The decrease of the mobility at elevated temperature found here for bulk BP is in

line with reports on few layer BP, which show a decrease of the carrier mobility in phosphorene field effect transistors and Hall measurements at elevated temperatures.[12, 56]

Figure 2.3b shows that the non-radiative decay rate, k_1, decreases with temperature. As with temperature the intrinsic charge carrier density rises strongly (see figure 2.3d), trap states become filled to a larger extent and consequently trap-assisted SRH recombination becomes less important at higher temperature.

As expected from the theoretical considerations above, the second-order radiative recombination coefficient k_2 decreases with temperature, see figure 2.3c. Fits of the theoretical model to the experimental data in figures 2.1 and 2.2 gives for the parameter $p = (3.6 \pm 0.4) \times 10^{-2}$ cm^{3}s^{-1}J$^{-1/2}$. This translates into a k_2 value at room temperature of $(2.3 \pm 0.3) \times 10^{-10}$ cm^{3}s^{-1}, which is in good agreement with results for low bandgap semiconductors like InSb, InAs and InGaSb showing k_2 values of the order of 10^{-10} cm^{3}s^{-1}.[71, 75] From an analysis of the k_2 values it can be inferred that the second-order recombination is reaction-limited and cannot be diffusion-limited. For a diffusion-limited recombination process k_2 depends on the mobility according to $k_2 = e[\mu_e + \mu_h]/\varepsilon_0 \varepsilon_r$, where ε_0 and ε_r, are the free space and relative permittivity, respectively.[66] Taking the room temperature mobilities $\mu_e = 220$ cm^{2}V^{-1}s^{-1} and $\mu_h = 350$ cm^{2}V^{-1}s^{-1} from reference[76] and $\varepsilon_r = 12.3$ from reference[49], gives a diffusion-limited recombination coefficient $k_2 = 8 \times 10^{-5}$ cm^{3}s^{-1}, which is more than five orders of magnitude higher than the value obtained from the fitting. Hence, diffusion-limited recombination can be ruled out and it is concluded that second-order electron-hole recombination in bulk BP is a reaction-limited radiative process.

To reproduce the experimental data in figures 2.1 and 2.2, the Auger recombination coefficient k_3 must be less than 10^{-32} cm^{6}s^{-1}. This value is much smaller than for other low bandgap semiconductors (*e.g.* InSb, InAs, InGaSb) having k_3 values in the range 10^{-24} to 10^{-28} cm^{6}s^{-1}. The much smaller value for bulk BP is likely due to restrictions imposed by the requirement of simultaneous conservation of momentum and energy of the three charges involved in Auger recombination. Theoretical calculations of the electronic band structure and

Auger recombination coefficients are needed to explain the factors determining the relatively low k_3 value for bulk BP. For the experimental charge densities considered above (figures 2.1 and 2.2) the fraction of charges undergoing Auger recombination is less than 10^{-3} and can be ignored. By contrast, Ge *et al.* [58] observed third-order Auger recombination in few layers BP flakes, since their density of electron-hole pairs near 5×10^{21} cm^{-3} (recalculated from the given two-dimensional density) is about four orders of magnitude higher than those in the present work.

2.3.4 Radiative Yield of Charge Recombination

The radiative yield, RY, is defined as the net number of photons emitted from the sample normalized to the net number of electron-hole annihilation events (radiative and non-radiative). RY is thus the ratio of the second-order radiative rate in equation (2.1) and the sum of all recombination rates; *i.e.*

$$RY = \frac{k_2\left[n^2(t)-n_i^2\right]}{k_1\left[\frac{n^2(t)-n_i^2}{n(t)}\right]+k_2\left[n^2(t)-n_i^2\right]+2k_3n(t)\left[n^2(t)-n_i^2\right]} \tag{2.2}$$

The second-order radiative decay rate (numerator in equation (2.2)) can be written as $k_2\left[\Delta n(t)+2n_i\right]\Delta n(t)$, which corresponds with a pseudo first-order radiative recombination rate equal to $k_1^{\text{pseudo}}(t)=k_2\left[\Delta n(t)+2n_i\right]$. For the experimental conditions used to obtain the data in figure 2.1, the 50 ns pulse yields an (end of pulse) excess density of electrons and holes of $\Delta n(t=50)=(2.5\pm0.09)\times10^{17}$ cm^{-3}, so that $k_1^{\text{pseudo}}(t=50)=k_2\left[\Delta n(t=50)+2n_i\right]=75\pm8.6$ μs^{-1}, while for long time-scales $k_1^{\text{pseudo}}(t\to\infty)=2k_2n_i=3\pm0.35$ μs^{-1}. For the 50 ns electron pulse the excess density of electron-hole pairs at the end of the 3 MeV electron pulse largely exceeds the room-temperature intrinsic charge density $n_i\approx10^{15}$ cm^{-3}, see figure 2.3d. In that case, the pseudo first-order non-radiative rate for SRH recombination is to a good approximation equal to k_1, which is about 20 μs^{-1} at room temperature (see figure 2.3b). As discussed above, for the charge densities in the current experiments Auger recombination can be neglected and therefore the radiative recombination yield can be obtained as

$RY = k_2[\Delta n + 2n_i]/(k_1 + k_2[\Delta n + 2n_i])$, which gives $0.78\ (78 \pm 5\ \%)$ at the end of the 50 ns pulse and decreases to $0.13(13 \pm 0.03\ \%)$ for a single carrier pair added to the background of the intrinsic carrier density. Hence, the early recombination dynamics is radiatively limited. The total fraction of charges decaying *via* second-order radiative recombination after the 3 MeV electron pulse can be obtained by integration of the numerator and the denominator in equation (2.2) over time, which yields a radiative yield of 0.66 (66 %). Hence, for excess densities of electron-hole pairs of the order of $10^{17}\ \mathrm{cm}^{-3}$ radiative recombination is significant. The radiative yield will increase for higher density of excess charges and eventually decrease for very high densities due to the then dominant Auger recombination (see also figure 2.4). For higher density of excess charges n_i can be ignored and in that case the maximum radiative yield obtained from equation (2.2) is $RY_{\max} = \left(1 + 2\sqrt{2k_1k_3}/k_2\right)^{-1}$ (under continuous steady state excitation). Taking the recombination rate coefficients k_1 and k_2 at room temperature from figure 2.3 and the upper limit of k_3 yields $RY_{\max} = 0.995$ at an excess charge density of $3 \times 10^{19}\ \mathrm{cm}^{-3}$ which is not accessible in the current experiment (due to the limitation of the beam current to 4 A), but may be reached *e.g.* by photoexcitation.

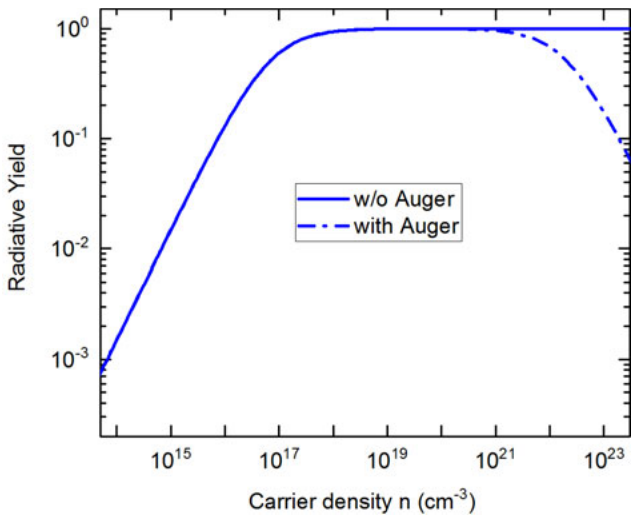

Figure 2.4 Total charge carrier density ($n = n_i + \Delta n$) dependence of the radiative yield in BP under steady state conditions obtained from equation (2.2)

with the obtained rate coefficients k_1, k_2 and k_3. The straight curve corresponds to a vanishing non-radiative Auger recombination coefficient k_3, while the dash-dotted curve shows the case of the upper boundary for k_3.

Figure 2.4 shows an illustration of the total carrier density ($n = n_i + \Delta n$) dependence of the radiative yield of BP under steady state conditions using the obtained room temperature values for k_1, k_2 and upper bound for k_3 reflecting Auger decay. On increasing the charge density the value of RY first goes up, since second-order radiative decay becomes more significant as compared to non-radiative SRH recombination. For densities above 10^{18} cm^{-3} the value of RY converges to unity. If there is additional Auger decay, RY decreases considerably for densities above 10^{21} cm^{-3}.

The high radiative recombination yield for charge densities above 10^{17} cm^{-3} makes BP a promising material for application in efficient infrared emission devices around 4 μm, as this is the necessary density range for efficient operation of infrared LEDs or laser diodes.[77]

2.4 Conclusions

A global analysis scheme is used to reveal the impact of radiative second-order decay and the presence of intrinsic carriers on the decay dynamics of charge carriers in BP. The combined electron and hole mobilities in BP increases at low temperatures with temperature due to ionized impurity scattering and after reaching a maximum near 250 K it drops to about half the maximum value due to deformation potential scattering. The rate coefficients for second-order radiative recombination and for non-radiative SRH recombination are found to decrease with temperature. Non-radiative third-order Auger recombination is negligible for the studied densities of excess electron-hole pairs. For densities of 2.5×10^{17} cm^{-3} a major fraction (78 %) of the excess electrons and holes undergo radiative recombination. For higher excess charge densities of the order of 10^{18} cm^{-3} electron-hole recombination is expected to occur with near unity radiative yield. This makes BP an interesting material for efficient infrared emitter devices like LEDs or lasers around 4 μm.

3. Thermally Activated Indirect to Direct Radiative Recombination of Electrons and Holes in Tin Disulfide Two-Dimensional van der Waals Material

This chapter is based on the following work:
P. Bhaskar, A. W. Achtstein, M. J. W. Vermeulen, L. D. A. Siebbeles, *Journal of Physical Chemistry C* **2019**, Article ASAP, DOI:10.1021/acs.jpcc.9b01842

3.1 Introduction

Two-dimensional layered materials are of interest due to their intriguing optical and electronic properties and promising prospects for application in optoelectronic devices.[47, 78-83] Beyond graphene, black phosphorus and transition metal dichalcogenides have been studied extensively.[43, 76, 84-87] Among other emerging metal dichalcogenides materials tin disulfide (SnS_2) currently attracts attention for water splitting,[88] photoconductivity,[89-90] electronic and optical,[91-93] (thermo)electrical,[94-95] photovoltaic[96] and photocatalytical applications.[97]

Bulk SnS_2 is a semiconductor with an indirect band gap of 2.29 eV and a direct gap of 2.44 eV.[27, 93] It consists of layers of hexagonally attached tin and sulfur atoms that are stacked together by weak van der Waals forces. Monolayers and few-layers of SnS_2 exhibit an indirect band gap, unlike monolayers of transition metal dichalcogenides.[94, 98] However, upon application of biaxial tensile strain[99] an indirect to direct band gap transition can be induced in SnS_2.

The mobility and decay pathways of charge carriers play an important role in (opto)electronic devices. According to a theoretical first principles study the electron and hole mobility in a monolayer of SnS_2 are as high as 756 $cm^2V^{-1}s^{-1}$, and 187 $cm^2V^{-1}s^{-1}$, respectively.[94] For monolayer SnS_2 electron mobilities of 50 $cm^2V^{-1}s^{-1}$ and 230 $cm^2V^{-1}s^{-1}$ have been reported, while values of 1.5 $cm^2V^{-1}s^{-1}$ and 20 $cm^2V^{-1}s^{-1}$ were found for samples of 10 nm and 120 nm thickness, respectively.[98, 100] For bulk SnS_2 electron mobilities in the range $15-50$ $cm^2V^{-1}s^{-1}$ have been found,[89, 101] and a combined electron and hole mobility of 150 $cm^2V^{-1}s^{-1}$ has been published.[92]

Figure 3.1 illustrates of the band structure of bulk SnS_2, as obtained from density functional theory (DFT) calculations described in the Methods section below. Quantitative results from detailed DFT calculations can be found elsewhere.[94, 99, 102] The maximum of the valence band is at the $\Gamma-$point, while the minimum in the conduction band is at the $M-$point. This causes SnS_2 to be an indirect band gap semiconductor.[91, 98, 102] Recombination of electrons and holes via the indirect band gap (orange arrow in figure 3.1) occurs via a phonon assisted process to conserve momentum. It is also possible that the electron is thermally excited from the $M-$point to the $\Gamma-$point in the conduction band (purple arrow in figure 3.1), followed by radiative recombination (green arrow in figure 3.1). The latter

process is expected to occur with an activation energy equal to the energetic difference (0.15 eV) between the $M-$point to the $\Gamma-$point in the conduction band.

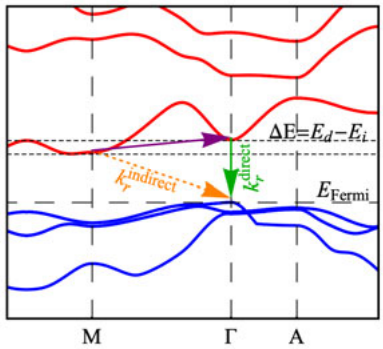

Figure 3.1 Illustration of the band structure of SnS_2 obtained from DFT. The purple arrow indicates thermal excitation of an electron from the indirect band to the direct band, orange and green arrows indicate electron-hole recombination via the indirect and direct band gap.

The aim of the current work involves characterization of the mobility and recombination pathways of charge carriers in bulk SnS_2. Electrons and holes were generated by irradiation of the sample with 3 MeV electron pulses and their dynamics was probed by contactless microwave conductivity measurements at various temperatures. According to theoretical analysis of the magnitude and decay kinetics of the conductivity, electrons and holes have a mobility near $100\ cm^2V^{-1}s^{-1}$ and predominantly decay via recombination after thermal electron excitation from the $M-$point to the $\Gamma-$point in the conduction band.

3.2 Methods

3.2.1 Transient Conductivity

Thin flakes of SnS_2 (2H phase) were procured from HQ Graphene (Groningen, the Netherlands) with 99.995 % purity and used without any further treatment. The yellowish translucent flakes of SnS_2 were filled into a polyetheretherketone (PEEK) sample holder with a groove of 1 mm along the direction of high-energy electron irradiation, analogous to our previous study on Te.[103] The flakes were tightly pressed to fill the groove entirely. The sample holder was inserted into a copper waveguide cell suitable to perform microwave conductivity studies in the K_a-band (28-37 GHz), similar to previous studies.[21, 103-104] Electrons and holes

were generated in the sample via irradiation with 3 MeV electron pulses from a van de Graaff electron accelerator. The 3 MeV electrons lose part of their energy by impact-ionization in the sample, leading to a uniform spatial distribution of electron-hole pairs. The stopping range of the 3 MeV electrons exceeds the 1 mm sample length and therefore they pass through the sample so that charge neutrality is maintained. Successive irradiation did not affect the measured microwave conductivity, which implies the absence of effects of radiation damage.

The radiation dose D_{SnS_2} deposited in SnS_2 by the 3 MeV electrons was obtained from $D_{SnS_2} = D_{Bz}\left(N_{e,SnS_2}\rho_{SnS_2}M_{Bz}/N_{e,Bz}\rho_{Bz}M_{SnS_2}\right)$, where $D_{Bz} = 530$ $Jm^{-3}nC^{-1}$, is the reference dose absorbed by benzene (Bz), N, ρ and M are the number of electrons per molecule, mass density, and molecular mass of SnS_2 or benzene. The density of electron-hole pairs generated in SnS_2 per unit time during the 3 meV electron pulse is $G_{pulse} = D_{SnS_2}/\left(E_p t_{pulse}\right)$, where E_p is the pair-formation energy and t_{pulse} is the pulse duration. For semiconductors, the pair formation energy for high-energy electron irradiation can be estimated according to an empirical formula provided by Alig *et al.*,[105] which is given by $E_p = 2.73E_g + b$, where $b = 0.5$ eV and $E_g = 2.29$ eV the band gap of SnS_2 in the 2H phase.[93, 106]

The generated charge carriers absorb a part, $\Delta P(t)$, of the incident microwave power P, which is related to the conductivity $\Delta\sigma(t)$ by $\Delta P(t)/P = -AB\Delta\sigma(t)$, where A and B are sensitivity factors, see refs.[30-31] The factor A accounts for the effect of microwave cell dimensions and the dielectric constant of the sample. The factor B accounts for the effects due to heterogeneity of the sample resulting from the layers of SnS_2 and the PEEK sample holder. This leads to an effective dielectric constant that can be described by[32, 63, 107]

$$\varepsilon_* = \varepsilon_*^{'} - j\varepsilon_*^{''} = d\left[\sum_i \frac{d_i}{\varepsilon_i^{'} - j\varepsilon_i^{''}}\right]^{-1} \tag{3.1}$$

In the above equation, ε_* is the effective dielectric constant due to the stacked layers with real and imaginary dielectric constants $\varepsilon_i^{'}$ and $\varepsilon_i^{''}$ with layer thickness d_i, and total thickness d, while $j^2 = -1$.

3.2.2 DFT Calculations

For illustrative purpose the band structure of SnS_2 was calculated using the Amsterdam Density Functional theory program (ADF-BAND).[108-110] The calculation was done using a DZP (double zeta and one polarization) basis set and the Perdew-Burke-Ernzerhof generalized gradient approximation density functional. Relativistic spin-orbit coupling was taken into account.

3.3 Results and Discussion

3.3.1 Time Dependent Microwave Conductivity due to Excess Charges

The transient conductivity of electrons and holes generated by 3 MeV electrons is shown in figure 3.2 for different pulse durations t_{pulse} and temperatures T. The inset in figure 3.2a shows the end-of-pulse conductivities $\Delta\sigma_{\text{eop}}$ for t_{pulse} ranging from 1 ns to 20 ns. The sub-linear increase of $\Delta\sigma_{\text{eop}}$ with t_{pulse} for long pulse duration is an indication of higher-order recombination at higher charge carrier densities. Figures 3.2b, 3.2c and 3.2d show the transient conductivities for t_{pulse} equal to 5 ns, 10 ns and 20 ns in the temperature range of 198 K to 373 K. It is observed that the decay of the conductivity becomes faster as the temperature increases.

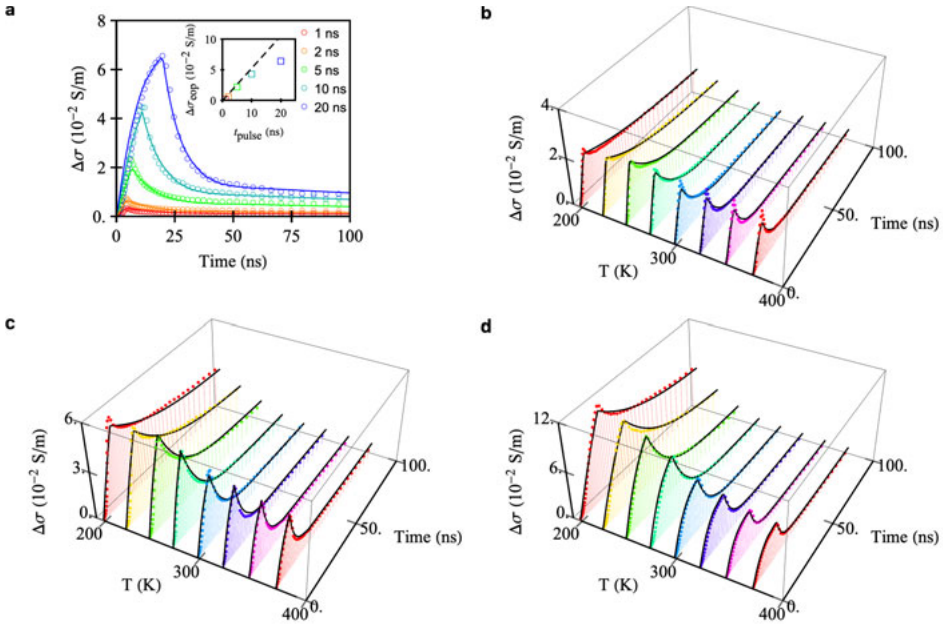

Figure 3.2 *Transient microwave conductivity of charge carriers in SnS_2 at room temperature obtained for various pulse durations at T = 298 K (a) and for various temperatures from 198 K to 373 K for 5 ns (b) 10 ns (c) and 20 ns (d) pulse durations. The dotted curves are the experimental conductivity traces and the drawn curves were obtained from theoretical modelling. The inset in (a) shows the end-of-pulse conductivity, $\Delta\sigma_{\mathrm{eop}}$, as a function of pulse duration t_{pulse}.*

3.3.2 Theoretical Modelling

The formation and decay dynamics of electrons and holes can be described by the following differential equations.

$$\frac{\mathrm{d}n_1(t)}{\mathrm{d}t} = G_{\mathrm{pulse}}\phi_1 - k_1 n_1(t) - k_r n_1(t) n_2(t) \tag{3.2}$$

$$\frac{\mathrm{d}n_2(t)}{\mathrm{d}t} = G_{\mathrm{pulse}}\phi_2 - k_2 n_2(t) - k_r n_1(t) n_2(t) \tag{3.3}$$

In equations (3.2) and (3.3), $n_1(t)$ and $n_2(t)$ are interchangeable electron and hole densities, as the experiment cannot distinguish which corresponds to electrons and which to holes. The densities generated during the 3 MeV electron pulse with generation rate G_{pulse} is determined to be $(2.2 \pm 0.3) \times 10^{15}$ $\mathrm{cm}^{-3}\mathrm{nC}^{-1}$, as described in the Methods section. The term $G_{\mathrm{pulse}} = G\left[\Theta(t) - \Theta\left(t - t_{\mathrm{pulse}}\right)\right]$ with

Θ the Heaviside function is non-zero during the electron pulse only. The factors ϕ_1 and ϕ_2 are the initial yields of charges of type 1 and 2, accounting for the survival fraction of charges from trapping and geminate recombination on times shorter than t_{pulse}. The rate constants k_1 and k_2 account for the first-order decay of charges to traps. The rate-constant k_r takes second-order (radiative) recombination of electrons and holes into account. The relation between the transient microwave conductivity $\Delta\sigma(t)$, the transient densities of charges $n_1(t)$ and $n_2(t)$ and the charge mobilities μ_1 and μ_2 is given by

$$\Delta\sigma(t) = e\left[\mu_1 n_1(t) + \mu_2 n_2(t)\right]. \tag{3.4}$$

Equations (3.2) - (3.4) were globally fitted to the experimental data for various values of t_{pulse} and T with $\mu_1, \mu_2, k_1, k_2, k_r, \phi_1$ and ϕ_2 as adjustable parameters. Figure 3.2 shows that the theoretical fits reproduce the experimental results very well.

3.3.3 Mobility and Initial Yield of Charges

Figure 3.3 shows the temperature dependent mobility of charges of type 1 and 2 observed from the fit. For the charges of type 1, the mobility μ_1 decreases with temperature, which is typical for band-like transport with increased electron-phonon scattering reducing the mobility at higher temperature.

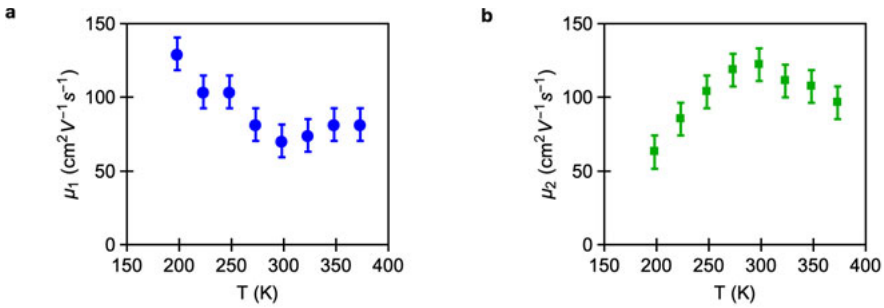

Figure 3.3 Temperature dependent mobility for charges of type 1 (a) and type 2 (b), respectively.

The mobility μ_2 of charges of type 2 first increases with temperature to 300 K and then decreases at higher temperature. The initial increase could be due to defects in the SnS_2 crystal that can be surmounted more easily at higher

temperature. With further increase of temperature the reduction of the mobility could be due to dominance of electron-phonon scattering.

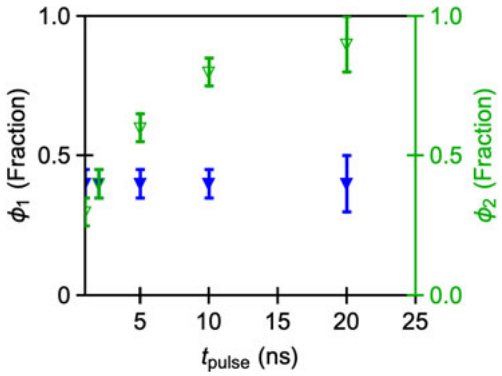

Figure 3.4 Initial yield of charges of type 1 and 2 as a function of pulse duration.

Figure 3.4 shows that the initial yield of type 1 charges, ϕ_1 , remains constant with t_{pulse}. This could be due to the presence of shallow traps, which would lead to the equilibrium between trapping and de-trapping of charges. For shallow traps these rates may be sufficiently high so that equilibrium is reached on a timescale much shorter than t_{pulse} and ϕ_1 reaches the equilibrium value. In that case, the rate equation for the density of trapped charges at equilibrium at a particular temperature can be written as

$$\frac{\mathrm{d}n_1^{\text{free}}}{\mathrm{d}t} = -k_1^{\text{trap}} n_1^{\text{free}} + k_1^{\text{detrap}} n_1^{\text{trapped}} = 0, \tag{3.5}$$

where n_1^{free}, n_1^{trapped}, k_1^{trap} and k_1^{detrap} are the free charge density, trapped charge density, trapping rate and de-trapping rate for charges of type 1, at short times during the pulse t_{pulse}. According to equation 3.5, at equilibrium, the ratio of free charge density and trapped charge density is equal to the ratio $k_1^{\text{detrap}} / k_1^{\text{trap}}$. It was found that ϕ_1 and ϕ_2 are merely temperature independent (data not shown), implying a constant ratio $k_1^{\text{detrap}} / k_1^{\text{trap}}$. From this we infer that the energetic depth of the shallow traps is less than 15 meV, which is the thermal energy corresponding to the lowest temperature of 198 K used in the experiments. It is observed that the initial yield of charges of type 2, ϕ_2, increases with t_{pulse}. This

can be due to enhanced filling and eventual saturation of traps as the pulse duration (and thus the charge density) increases.

3.3.4 Charge Carrier Recombination and Decay

The second-order (radiative) recombination constant k_r found from the fits of the theoretical model described above increases strongly with temperature, see figure 3.5a. The thermal activation can be understood as follows: As can be seen in figure 3.1, recombination via the indirect band gap of SnS_2 corresponds to a transition of an electron from the $M-\text{point}$ in the conduction band to the $\Gamma-\text{point}$ in the valence band. This transition involves a change of momentum of the electron. To conserve total momentum the transition must be assisted by phonons. An increase of temperature will enhance the mediation by phonons and thus lead to an increase of the indirect recombination rate constant. The alternative recombination process occurs by thermal excitation of an electron from the $M-\text{point}$ to the $\Gamma-\text{point}$ in the conduction band and subsequent radiative recombination with the hole.[98] The recombination rate constant associated with this pathway is thermally activated, since it requires excitation of an electron from the $M-\text{point}$ to the $\Gamma-\text{point}$. In that case the activation energy, ΔE, is the difference between the direct and indirect band gap SnS_2, which is $0.15\ \text{eV}$.[27, 93]

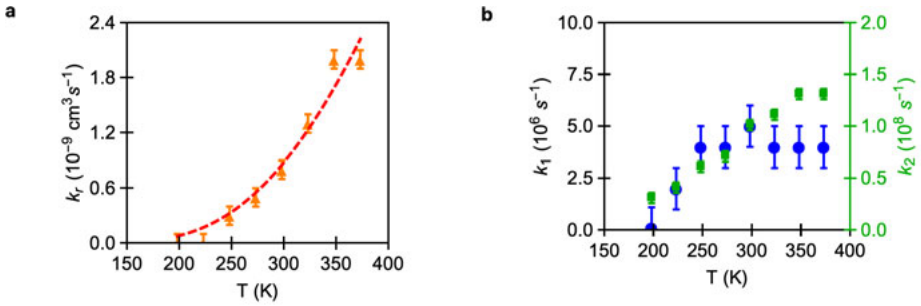

Figure 3.5 (a)Temperature dependent second-order recombination rate constant k_r obtained from fitting the theoretical model (see equations 3.2-3.4) to the experimental conductivity data (triangular markers). The dashed line is a fit of equation 3.6 to the data. (b) Temperature dependence of trapping rate constants k_1 (blue) and k_2 (green) for charges of type 1 and 2.

The total recombination rate is the sum of the rates for the transition via the indirect band gap, k_r^{indirect}, and the direct band gap, k_r^{direct}, which according to the work of Hall is given by[111]

$$k_r^{\text{tot}} = k_r^{\text{indirect}} + k_r^{\text{direct}} \exp\left(\frac{-\Delta E}{k_B T}\right) \tag{3.6}$$

In equation (3.6), $k_r^{\text{indirect}} = A\coth(\theta/2T)$, where the prefactor A is temperature independent,[73, 75, 111] θ is the Debye temperature (calculated to be 137 K for SnS_2[94]) and k_B is the Boltzmann constant. We fitted equation (3.6) to the data points in figure 3.5a yielding the dashed curve with $k_r^{\text{indirect}} < 10^{-12}$ cm^{3}s^{-1} and $k_r^{\text{direct}} = (2.3 \pm 0.2)\times 10^{-7}$ cm^{3}s^{-1}. With these values the recombination rate *via* the direct band gap is found to be at least two orders of magnitude higher than via the indirect band gap. Hence, electron-hole recombination occurs mainly via thermal excitation of an electron to the $\Gamma-$point and subsequent radiative decay.

So far we have considered reaction-limited recombination only. In general, second-order recombination can also be a diffusion-limited process with Langevin recombination rate constant $k_r^{\text{diff}} = e(\mu_1 + \mu_2)/\varepsilon_0\varepsilon_r$,[112] where ε_0 and ε_r are the permittivity of vacuum and the dielectric constant of a material. Taking the room temperature value of $(\mu_1 + \mu_2) = 193$ cm^{2}V^{-1}s^{-1} and $\varepsilon_r = 7.5$,[113] the value of k_r^{diff} is calculated to be 5×10^{-7} cm^{3}s^{-1}, which is more than one order of magnitude larger than the measured value of $(0.8 \pm 0.1)\times 10^{-9}$ cm^{3}s^{-1}. Hence we conclude that recombination is not diffusion-limited, but occurs *via* the reaction-limited process with radiative decay at the $\Gamma-$point, as discussed above.

Next we discuss the first-order trapping rates in figure 3.5b. In case trapping is diffusion controlled, the rate is proportional to the diffusion coefficent of the charge carrier, which is related to the mobility as $D = \mu k_B T/e$. The temperature dependence of the mobilities in figure 3 then yield a much smaller thermal activation of *D* than the trapping rates in figure 3.5b. Hence, trapping is not a diffusion-limited process. Apparently trapping occurs via a thermally activated reaction-limited pathway. The thermal activation can be due to the fact that the

nuclear lattice undergoes a structural reorganization when a charge enters a trapping site. This is similar to polaron formation or Marcus charge transfer.[114]

3.4 Conclusions

The mobility of charge carriers of type 1 is 70 ± 12 $cm^2V^{-1}s^{-1}$ and of the opposite charges it is 123 ± 12 $cm^2V^{-1}s^{-1}$. The decrease of the mobility at higher temperature is typical for a band-like transport mechanism. Theoretical analysis of the charge carrier decay kinetics reveals that electron-hole recombination occurs by thermal promotion of electrons from the indirect to the direct band gap, followed by radiative recombination. Phonon assisted recombination via the indirect band gap is found to be negligible.

4. Mobility and Decay Dynamics of Charges in One-Dimensional Selenium van der Waals Solid

This chapter is based on the following work:

P. Bhaskar, A. W. Achtstein, S. L. Diedenhofen, L. D. A. Siebbeles, *Journal of Physical Chemistry C* **2017**, *121*, 18917-18921

4.1 Introduction

Van der Waals solids attract a great deal of interest due to possibilities to prepare single layers or stacks of two-dimensional (2D) semiconductor sheets.[79, 82, 85] Electronic quantum confinement perpendicular to the plane of a sheet allows one to tune the optoelectronic properties by varying the number of stacked sheets. Recent developments of large-scale production of 2D sheets *via* liquid exfoliation offer promising prospects for optoelectronic applications, in contrast to small-scale mechanical exfoliation[81, 87, 115] or controlled solution-phase chemical synthesis.[23]

In nanoelectronics one-dimensional (1D) wires are also of interest. Solution processable nanowires have been studied in the form of conjugated organic molecular chains (polymers),[61, 116-120] or as colloidal semiconductor nanorods/nanowires.[121] Interestingly 1D van der Waals solids also exist, such as trigonal selenium (Se) and tellurium (Te).[122] Until now, only a few studies on the optoelectronic properties of these 1D van der Waals solids have been reported, including calculations of electronic band-structure[25, 123-124] and measurements of photoconductivity[125-126], magnetoconductivity[127], magnetoabsorption[25] and electroreflectance.[128] Charge carrier mobilities from $0.1\,cm^2V^{-1}s^{-1}$ up to $40\,cm^2V^{-1}s^{-1}$ were found for (photo-)doped trigonal Se.[24, 125-127] In these measurements the high doping densities could have led to trap filling, which increases the mobility compared to that at low charge carrier density.

The aim of the present study is to provide insight into the mobility and charge decay dynamics *via* trapping or recombination in trigonal Se at varying charge carrier density, similar to our previous work on 2D black phosphorus.[104] Possible negative effects of backscattering of charges at the ends of Se chains on the mobility are discussed, using the theoretical model of Prins *et al*.[129]

4.2 Experimental Methods

Pellets of trigonal Se from Sigma Aldrich with purity ≥ 99.999% were powdered using a pestle and mortar. The trigonal crystal structure was confirmed from Raman spectroscopy using a Renishaw inVia system in backscattering configuration with an excitation wavelength of 514 nm.

To study the dynamics of excess charge carriers the Se powder was introduced into a microwave conductivity measurement cell with dimensions suitable for

frequencies in the K_a band (27-38 GHz), similar to our previous studies.[104] High-energy (3 MeV) electron pulses from a van de Graaff accelerator were used to generate excess electrons and holes in the sample. The high-energy electrons pass through the sample and lose energy by generating a close to uniform distribution of electron-hole pairs along their tracks without inducing net charging in the sample. During the 3 MeV electron pulse electron-hole pairs are generated with number density per unit time, G, given by the ratio of the known energy transfer rate (radiation dose per unit time) from the electron pulse to the sample and the energy required for the formation of an electron-hole pair. The radiation dose in the Se sample, D_{Se}, was obtained from a reference measurement on benzene (Bz) according to $D_{\mathrm{Se}} = D_{\mathrm{Bz}}\left(N_{\mathrm{e,Se}}\,\rho_{\mathrm{Se}}\,M_{\mathrm{Bz}}/N_{\mathrm{e,Bz}}\,\rho_{\mathrm{Bz}}\,M_{\mathrm{Se}}\right)$, with N_e, ρ and M the number of electrons per atom/molecule, the mass density and the atomic/molecular mass for Se or Bz.[66, 104] The electron-hole pair formation energy, E_{p}, was estimated from the empirical formula provided by Alig *et al.*[105], which is given by $E_p = 2.73E_g + b$ with $b = 0.5$ eV and $E_g = 1.9$ eV[25] the band gap of trigonal Se. The density of generated electron-hole pairs is given by the ratio of D_{Se}/E_p.

The transient conductivity, $\Delta\sigma(t)$, due to excess charge carriers is obtained from the measured change of microwave power reflected from the cell, according to $\Delta P(t)/P = -A\Delta\sigma(t)$, with A being a sensitivity factor depending on the cell dimensions and dielectric constant of the sample.[30] The transient conductivity is equal to $\Delta\sigma(t) = e\left[\mu_n n(t) + \mu_p p(t)\right]$, with e the elementary charge, μ_n and μ_p the mobility of electrons and holes, $n(t)$ and $p(t)$ the transient densities of excess electrons and holes, respectively.

4.3 Results and Discussion

4.3.1 Structural Characterization

The crystal structure of the powdered Se sample was characterized using Raman spectroscopy (see Experimental Methods). The measured Raman spectrum in figure 4.1a shows a peak at 237 cm^{-1}, which is characteristic for the trigonal phase consisting of helical chains of Se atoms.[122, 130-131] Other phases of Se (α-monoclinic or vitreous) are known to exhibit Raman shifts in the range 250-256 cm^{-1}, [122] which are not observed in figure 4.1a. From this we infer that our sample

predominantly consists of helical Se chains in the trigonal phase, as shown in the inset of figure 4.1a.

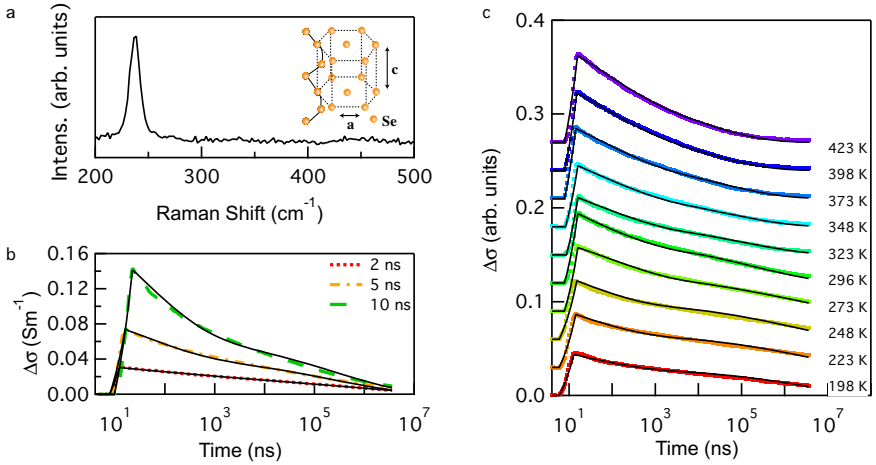

Figure 4.1 (a) The Raman spectrum exhibits a peak at 237 cm^{-1}, which is characteristic for helical Se chains in the trigonal phase with a crystal structure as shown on the inset. (b) Transient microwave conductivity due to excess charge carriers in Se at room temperature measured using different durations of the 3 MeV electron pulse (colored curves) and obtained from theoretical modelling (drawn black curves). (c) Transient conductivity obtained with a 5 ns electron pulse for different temperatures with vertical offsets for clarity.

4.3.2 Transient Microwave Conductivity Measurements

The powdered trigonal Se sample was contained in a rectangular microwave cell suitable for conductivity detection near 30 GHz, see Experimental Methods. The sample was irradiated with pulses of 3 MeV electrons that lose energy along their path through the sample *via* impact-ionization. This leads to production of secondary, tertiary *etcetera*, excess electrons and holes with a close to uniform spatial distribution. The incident 3 MeV electrons only lose part of their energy and leave the sample, so that net charging of the sample does not occur.

Figure 4.1b shows the transient microwave conductivity obtained with pulse durations as indicated. The conductivity increases during the pulse due to generation of mobile electrons and holes in the sample. The conductivity at the end of the electron pulse increases with its duration, which reflects that the density of the produced electrons and holes is higher for a longer pulse. The decay of charge carriers occurs by trapping at defects or by electron-hole recombination. It can be seen that the conductivity becomes shorter lived for longer pulse duration,

which is caused by faster higher-order recombination of electrons and holes at higher density.

Figure 4.1c shows the temperature dependence of the conductivity in the range of 198 K to 423 K. The conductivity transients are plotted with vertical offset for clarity. The conductivity at the end of the 3 MeV electron pulse increases with temperature and the decay kinetics becomes faster.

4.3.3 Theoretical Modelling

The transient microwave conductivity is given by $\Delta\sigma(t) = e\left[\mu_n n(t) + \mu_p p(t)\right]$ with μ_n (μ_p) the electron (hole) mobility, $n(t)$ ($p(t)$) the electron (hole) density and *e* the elementary charge. Charge mobilities and decay kinetics were obtained from fitting a theoretical model to the measured conductivity. The electron and hole densities were described by the differential equations

$$\frac{\mathrm{d}n(t)}{\mathrm{d}t} = G_{\text{pulse}}\phi_n - \frac{\beta_n\left(k_{1n}t\right)^{\beta_n}}{t}n(t) - k_2 n(t)p(t) \tag{4.1}$$

$$\frac{\mathrm{d}p(t)}{\mathrm{d}t} = G_{\text{pulse}}\phi_p - \frac{\beta_p\left(k_{1p}t\right)^{\beta_p}}{t}p(t) - k_2 p(t)n(t) \tag{4.2}$$

In equations (4.1) and (4.2) the first term contains the generation of electrons and holes with rate $G_{\text{pulse}} = G\left[\Theta(t) - \Theta\left(t - t_{\text{pulse}}\right)\right]$, where Θ is the Heaviside function making it non-zero only during the 3 MeV electron pulse. Further, ϕ_n and ϕ_p denote the fraction of charges surviving from direct trapping or geminate electron-hole recombination during the 3 MeV electron pulse. The second terms in equations (4.1) and (4.2) represent first-order electron (hole) trapping with characteristic rate k_{1n} (k_{1p}), which by themselves yield a stretched-exponential decay given by $n(t) = n(t=0)\exp\left[\left(-k_1 t\right)^{\beta}\right]$.[132] Such stretched-exponential decay can occur from charges that need to diffuse to the traps with a specific characteristic time $1/k_1$ followed by irreversible trapping. In that case of diffusion-limited trapping, the parameter $\beta = d/(d+2)$ with d the dimensionality of the medium.[132-133] The third terms in equations (4.1) and (4.2)

bring into account second-order radiative recombination of electrons and holes with rate constant k_2.

The coupled differential equations (4.1) and (4.2) were solved using a fourth-order Runge-Kutta method. The measured conductivity was modelled by fitting a constrained set of shared parameters $\phi_{n,p}$, $\beta_{n,p}$ and k_2 for all the experimental data, while the charge mobilities μ_n (μ_p) and first-order decay rates k_{1n} (k_{1p}) were allowed to vary with temperature. The model fits our experimental data as shown in figures 4.1b and 4.1c. In first instance, we included the recombination of free charges with trapped charges. It turned out that the recombination rate constant of free charges and trapped charges is much smaller than rate constant (k_2) for the mutual recombination of the free charges. Consequently, these processes can, hence, be ignored in the equations (4.1) and (4.2) to sufficiently describe the experimental data. The averaged conductivity transients were found to be independent of the number of 3 MeV electron pulses used. Hence, all charges recombine between successive electron pulses (with repetition rate of ~ 1 s^{-1}) and charge accumulation does not affect our results.

4.3.4 Initial Yield and Mobility of Charge Carriers

We found from our fits that one type of charge carrier becomes trapped much faster than the other. Following a previous report on efficient electron trappings in Se, we attribute the charge carriers that are trapped fastest to electrons.[126] We found electron survival fractions equal to $\phi_n = (0.11 \pm 0.01)$, (0.36 ± 0.03) and (0.57 ± 0.06) for 2 ns, 5 ns and 10 ns pulse duration, respectively. The increase with pulse duration, or equivalently with initial electron density, can be attributed to a larger fraction of traps being filled at higher initial electron density. The fits yielded $\phi_p = 1$, which implies that all holes survive from trapping during the 3 MeV electron pulse.

The fits yielded $\beta_n = \beta_p = (0.30 \pm 0.05)$, corresponding to 1D charge transport $(d = 1)$. In agreement with this, the helical chains in trigonal Se are held together by weak van der Waals forces causing transport along the chains to be much more efficient than from one chain to another, which leads to (almost) 1D charge transport.

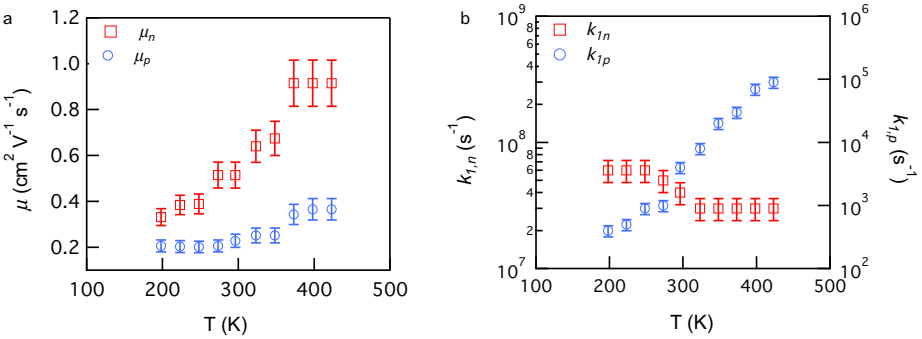

Figure 4.2 (a) Temperature dependence of (a) the measured microwave mobilities of electrons and holes and (b) their trapping rates.

The 1D mobilities of electrons and holes moving along the Se chains were found to be $\mu_n = (0.52 \pm 0.06)$ cm^{2}V^{-1}s^{-1} and $\mu_p = (0.23 \pm 0.03)$ cm^{2}V^{-1}s^{-1} at room temperature. The mobilities increase with temperature as shown in figure 4.2a. The increase of the mobility with temperature may be due to scattering on static structural defects or charged impurities that can be surpassed by thermal activation.[1] At elevated temperature, the mobilities of electrons and holes tend to saturate. This can be attributed to a more prominent role of scattering on phonons, which has a reducing effect on the mobility.

The microwave mobilities in figure 4.2a obtained from the measured conductivity data in figure 4.1 can be limited by scattering of charges at the ends of Se chains. In that case, the intra-chain mobility of charge carriers, μ_{intra}, (that would be obtained in absence of such scattering) can be related to the measured ac mobility of charges, μ_{ac}, moving on a chain with length L in an AC electric field oscillating with radian frequency ω, according to

$$\mu_{ac} = 8\mu_{\text{intra}} \sum_{j=0}^{\infty} \frac{c_j^{-2}}{\left(\frac{\mu_{\text{intra}} k_B T}{eL^2\omega}\right)^2 c_j^4 + 1}, \qquad (4.3)$$

with $c_j = 2\pi(j + 1/2)$.[129] Figure 4.3 shows the ac mobility at the experimental frequency of 30 GHz, calculated according to equation (4.3), as a function of μ_{intra} for chain lengths in the range 300 nm to 100 μm. The dashed horizontal line denotes a mobility value of 0.5 cm^{2}V^{-1}s^{-1}, which is close to experimental results

for electrons and holes at room temperature. It can be seen from figure 4.3 that the Se chains should at least have a length of ~1 μm to reproduce the experimental mobility. For longer chains the mobility can be close to the measured value or much higher. Experiments on Se chains with well-defined length are needed to further establish precise value of the intra-chain mobility.

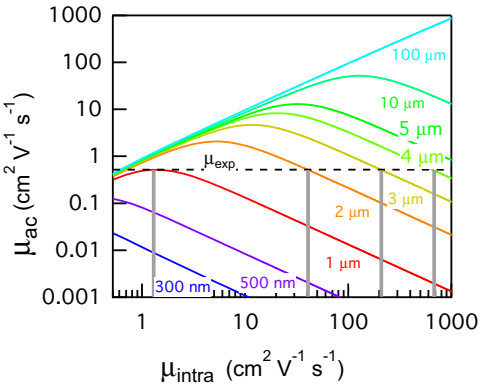

Figure 4.3 Microwave mobility as a function of intra-chain mobility for Se chains with lengths as indicated. The dashed horizontal line indicates a mobility of 0.5 $cm^2V^{-1}s^{-1}$*, which is close to the experimental values for electrons and holes at room temperature.*

4.3.5 Charge Decay by Trapping and Recombination

Figure 4.2b depicts the trapping rates for electrons and holes at different temperatures. The electron-trapping rate slightly decreases with temperature, while it increases strongly for holes. The reduction of the electron-trapping rate with temperature can be due to faster thermally activated release of electrons from shallow traps. The presence of shallow electron traps agrees with the thermally activated electron mobility in figure 4.2a. The strong thermally activated trapping rate for holes suggests that they need to overcome a potential barrier to get trapped. The second-order electron-hole recombination rate is 10^{-13} cm^3s^{-1} and was found to be independent of temperature. This rate is likely due to relatively slow diffusion of charge carriers between different Se chains and therefore does not reflect the temperature dependence of the intra-chain charge mobility.

4.4 Conclusions

In conclusion, the 1D mobility of charge carriers along helical chains of Se in the trigonal phase is at least *ca.* 0.5 $cm^2V^{-1}s^{-1}$ at room temperature, which is promising for applications in nanoelectronics. In addition, the fact that Se is a van

der Waals solid offers prospects for large-scale production of isolated chains or bunches *via* liquid exfoliation.

5. Charge Mobility and Recombination Mechanisms in Tellurium van der Waals Solid

This chapter is based on the following work:

P. Bhaskar, A. W. Achtstein, M. J. W. Vermeulen, L. D. A. Siebbeles, *Journal of Physical Chemistry C* **2019**, *123*, 841-847.

5.1 Introduction

Extensive studies on fundamental properties of two-dimensional (2D) van der Waals materials have revealed new possibilities for the development of next generation optoelectronic devices.[20, 78-80, 82, 84, 134-135] 2D materials, where layers of strongly bound atoms are weakly held together by van der Waals forces, exhibit the possibility of separating the layers *via* exfoliation techniques, allowing one to engineer their electronic and optical properties. Similar to 2D materials, in one-dimensional (1D) materials, covalently bound chains of atoms are held together by weak van der Waals forces in the two perpendicular directions. Such 1D materials also have interesting promising applications in nanoelectronics. Two of such impeccable 1D systems are trigonal Selenium (Se) and Tellurium (Te), which have crystal structures that consist of helical chains of atoms. These materials exhibit potential for various applications due to their stability in air. As proposed for Se,[21] exfoliation of bulk Te to obtain 1D atomic chains of Te has been demonstrated recently.[26] However, Te is different from Se due to strong inter-chain electronic coupling in the bulk, thus being a quasi-1D system.[29] In addition, the 0.33 eV band gap of Te[22, 25] is much lower than the 1.9 eV band gap of Se.[13]

As a 1D van der Waals material, Te has been widely studied for its electronic structure,[25, 124, 136-137] optical properties,[22, 25, 138] Hall conductivity and extrinsic mobility in p-type Te.[139-142] Very recently, it gained attention due to its high thermoelectric figure of merit.[28, 143] The aforementioned studies on conductivity and mobility have mostly been performed at low temperatures (~77 K),[141] with externally doped samples and using contact measurements.[141, 144] Therefore, it is of great interest to study its intrinsic optoelectronic properties without external doping and at temperatures close to ambience.

In the present investigation, we provide insights into temperature dependent intrinsic charge carrier mobility and decay mechanisms in trigonal Te with varying charge carrier density, building up on our earlier results on other van der Waals materials.[21, 104] Quantitative analysis of our experimental observations reveals the characteristics of charge carrier mobility and recombination in the quasi-1D atomic chains of Te in bulk, laying the basis for further investigations of exfoliated Te. The high mobility and near unity quantum yield make Te of interest for nanoelectronics and optoelectronics. These properties and the low band gap make Te a promising material for use in far-infrared detectors. The

appreciably high mobility and quantum yield result in low device resistance and $1/f$ noise, which are essential to realize a high *S/N* ratio.[145]

5.2 Experimental Methods

Te pellets with purity 99.999% were procured from Sigma Aldrich (now MERCK) and used as received without any further treatment. Te pellets were finely powdered using a mortar and pestle for studying contactless microwave conductivity at various temperatures and at various densities of excess electrons and holes. The microwave conductivity studies were performed at frequencies in the range of the K_a band (27-38 GHz), similar to our previous studies.[21, 104] Uniform densities of excess electrons and holes were generated by irradiation with 3 MeV electron pulses from a van de Graaff accelerator, along with Bremsstrahlung irradiation. Bremsstrahlung was produced by retarding the electron pulses by a 2 mm lead (Pb) sheet. The high-energy Bremsstrahlung photons generate electron-hole pairs along their paths through the sample. Successive irradiation of the sample had no effect on the transient conductivity, implying the absence of radiation induced damage.

The powdered Te sample was filled into a polyetheretherketone (PEEK) sample holder with a groove of 1 mm along the direction of high-energy irradiation. In this sample holder, the sample height along the direction of electron irradiation is 1 mm, whereas the sample holder size is close to 3.5 mm. Such a sample holder was designed to avoid non-uniform generation of charges, as would have occurred due to stopping of high-energy electrons within the sample, discussed next. As Tellurium is a heavy material, with atomic number $Z = 52$, density $\rho_{Te} = 6.2\ \text{gcm}^{-3}$, $M_{Te} = 127.60\ \text{gmol}^{-1}$, it exhibits a comparatively higher stopping power ($S(E) = -dE/dx$) for the 3 MeV electrons, as compared to materials we studied previously.[21, 104] A higher stopping power leads to lower average penetration depth (Δx) for the 3 MeV electrons in the sample, which leads to a non-uniform distribution of charges inside the sample. In order to avoid a non-uniform charge density, the sample height was reduced so that the high-energy electrons could pass through the sample generating a close to uniform distribution. The stopping power and average penetration depth values were calculated using the equations (5.1) and (5.2) respectively, which were obtained by simplifying Bethe's expression for the collisional mass stopping power (also known as linear energy transfer) for high energy electrons.[146-149]

$$(S)_{\mathrm{Te}} = \left(\frac{S}{\rho}\right)_{\mathrm{H_2O}} \frac{18}{10} \rho_{\mathrm{Te}} \frac{Z_{\mathrm{Te}}}{M_{\mathrm{Te}}} \tag{5.1}$$

$$\Delta x = \int_0^{E_0} \frac{1}{S(E)} dE \tag{5.2}$$

In equations (5.1) and (5.2), ρ is the mass density,[60] Z the atomic number, M the elemental or molecular weight and E_0 is the 3 MeV energy of incident electrons. Equations (5.1) and (5.2) yield an average penetration depth of 3.5 mm. Since this significantly exceeds the sample width of 1 mm, a uniform density of electrons and holes is produced upon irradiation.

The stacked dual-layered structure consisting of Te and PEEK sample holder results in a heterogeneity of the sample along the direction of irradiation. In such a case for studying microwave absorption, the effective dielectric constant of a heterogeneous sample can be estimated by considering the Maxwell-Wagner effect, which is described by[32, 107, 150]

$$\varepsilon_* = \varepsilon_*^{'} - j\varepsilon_*^{''} = d\left[\sum_i \frac{d_i}{\varepsilon_i^{'} - j\varepsilon_i^{''}}\right]^{-1}. \tag{5.3}$$

In the above equation, d is the total height of the layered sample, d_i is the height of the i^{th} layer, $\varepsilon_i^{'}$ ($\varepsilon_i^{''}$) is the real (imaginary) part of the permittivity of the i^{th} layer ε_* corresponds to the effective dielectric constant and $j^2 = -1$. This effect introduces a sensitivity factor B, which is used to obtain the conductivity in absolute values (discussed below).

Due to very high conductivity signals of Te, nearly saturating the electronic regime of the experimental setup, even for a short electron pulse duration of 500 ps, the radiation dose was reduced by using a 2 mm Pb plate placed at the top of the experimental cell containing the sample. The introduction of the Pb plate resulted into a reduction of the irradiation dose by 70 times due to partial stopping of 3 MeV electrons in the plate and production of Bremsstrahlung. The reduction factor was deduced from a test experiment of Te using 300 ps electron pulse with and without using a Pb plate, for which the conductivity signal was well within the saturation range. The final dose on the sample is a result of slowed-down electrons as well as Bremsstrahlung. The incident high-energy electrons together

with the Bremsstrahlung resulted in the formation of uniformly distributed electrons and holes in the sample with number density G per unit time. G is given by the ratio of the known energy-transfer rate (radiation dose per unit time) from the irradiation and the energy required for the formation of an electron-hole pair.

The radiation dose in Te, D_{Te}, was obtained from a reference measurement on benzene (Bz), which was found to be $530\ \mathrm{Jm^{-3}nC^{-1}}$,[119] according to $D_{\mathrm{Te}} = D_{\mathrm{Bz}}\left(N_{e,\mathrm{Te}}\,\rho_{\mathrm{Te}}\,M_{\mathrm{Bz}} / N_{e,\mathrm{Bz}}\,\rho_{\mathrm{Bz}}\,M_{\mathrm{Te}}\right)$, followed by a reduction of 70 times due to the Pb sheet, where N, ρ, and M are the number of the electrons per atom/molecule, mass density, and atomic/molecular mass for Te or Bz, respectively. The electron-hole pair formation energy, E_{p}, was estimated from the empirical relation provided by Alig *et al.*,[105] which is given by $E_{\mathrm{p}} = 2.73E_{\mathrm{g}} + b$, where $b = 0.5$ eV and $E_{\mathrm{g}} = 0.33$ eV,[25] the band gap of Te. The density of generated electron-hole pairs is given by the ratio $D_{\mathrm{Te}}/E_{\mathrm{p}}$, and the generation rate of electron-hole pairs during the 3 MeV electron pulse with a rectangular shape during time and duration t_{pulse} is equal to $G = D_{\mathrm{Te}}/\left(E_{\mathrm{p}}\,t_{\mathrm{pulse}}\right)$.

The transient conductivity, $\Delta\sigma(t)$, due to excess charge carriers is obtained from the measured change of microwave power reflected from the cell, according to $\Delta P(t)/P = -AB\Delta\sigma(t)$, where A and B are sensitivity factors. While A depends on the cell dimensions and dielectric constant of the sample, B takes into account the heterogeneity of the sample by introducing a factor corresponding to an effective dielectric constant of the sample, as described previously.[150-151]

5.3 Results and Discussion

5.3.1 Transient Microwave Conductivity due to Excess Electrons and Holes

Figure 5.1 shows the transient microwave conductivity traces, obtained for various pulse durations and temperatures as indicated. The traces with markers are the experimental results, while the solid traces overlaid on top of them are obtained upon theoretical modelling as discussed below.

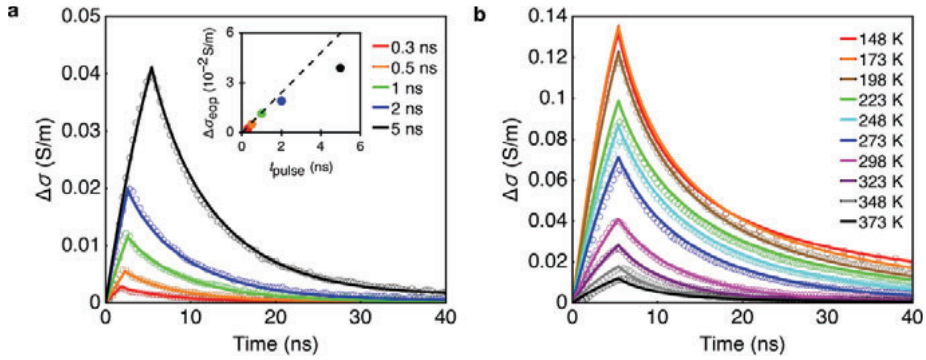

Figure 5.1. Transient microwave conductivity due to excess charge carriers in Tellurium at room temperature (298 K) for various durations of the 3 MeV electron pulse (curves with markers) and as obtained from theoretical modelling (solid curves) (a) and for various temperatures, as labeled (b). The inset shows the conductivity at the end of the electron pulse $\Delta\sigma_{\mathrm{eop}}$*, as a function of pulse duration* t_{pulse}.

The transient conductivity increases during the 3 MeV electron pulse, due to generation of excess mobile electrons and holes in the sample. Also, the end-of-the-pulse conductivities $\left(\Delta\sigma_{\mathrm{eop}}\right)$ increase as the pulse duration becomes longer from 0.3 ns through 5 ns (see in figure 5.1a), due to a higher charge carrier density for a longer pulse. The inset in figure 5.1a shows $\Delta\sigma_{\mathrm{eop}}$ as a function of pulse duration (t_{eop}). The sub-linear increase of $\Delta\sigma_{\mathrm{eop}}$ with t_{pulse} is due to higher-order recombination of charges in addition to the first-order trapping. Subsequently, the electrons and holes decay by recombination or trapping.

5.3.2 Theoretical Model of Charge Carrier Generation and Decay Dynamics

The transient microwave conductivity is given by $\Delta\sigma(t)=e\left[\mu_{n_1}\Delta n_1(t)+\mu_{n_2}\Delta n_2(t)\right]$, where μ_{n_1} and μ_{n_2} are mobilities for charge particles of type n_1 and n_2. Since we cannot distinguish electrons from holes, charges of type n_1 and n_2 correspond to electrons and holes, respectively, or vice versa. The excess charge densities are equal to $\Delta n_1(t)$ and $\Delta n_2(t)$, and e is the elementary charge. We describe the conductivity signals theoretically by taking into account the generation of excess electrons and holes with a generation

rate $G=(3.1\pm0.4)\times10^{14}$ $\mathrm{cm^{-3}ns^{-1}}$during the 3 MeV electron pulse, followed by recombination with each other, or with the intrinsic electrons and holes that are already present with equal densities $n_i(T)$, at temperature T, or by trapping at defects. The thermal generation and recombination at a given temperature results in significant equilibrium densities of electrons and holes, due to the low Te band gap of $E_g=0.33$ eV.[25]

Charge mobilities and decay kinetics were obtained from fitting a theoretical model to the measured conductivity traces, where excess electron and hole transient densities are described according to the coupled differential equations given by

$$\frac{d\Delta n_1(t)}{dt}=G_{\mathrm{pulse}}\phi_{n_1}-\frac{k_{n_1}^{\mathrm{SRH}}k_{n_2}^{\mathrm{SRH}}\left[n_1(t)n_2(t)-n_i^2\right]}{\left(k_{n_1}^{\mathrm{SRH}}n_1(t)+k_{n_2}^{\mathrm{SRH}}n_2(t)\right)}-\frac{\beta_{n_1}\left(k_{n_1}t\right)^{\beta_{n_1}}}{t}n_1(t)-k_r\left[n_1(t)n_2(t)-n_i^2\right] \tag{5.4}$$

$$\frac{d\Delta n_2(t)}{dt}=G_{\mathrm{pulse}}\phi_{n_2}-\frac{k_{n_1}^{\mathrm{SRH}}k_{n_2}^{\mathrm{SRH}}\left[n_1(t)n_2(t)-n_i^2\right]}{\left(k_{n_1}^{\mathrm{SRH}}n_1(t)+k_{n_2}^{\mathrm{SRH}}n_2(t)\right)}-\frac{\beta_{n_2}\left(k_{n_2}t\right)^{\beta_{n_2}}}{t}n_2(t)-k_r\left[n_1(t)n_2(t)-n_i^2\right] \tag{5.5}$$

The total electron or hole density is $n_1(t)=n_i+\Delta n_1(t)$ (and $n_2(t)=n_i+\Delta n_2(t)$), where $\Delta n_1(t)$ (and $\Delta n_2(t)$) is the density of excess electrons or holes produced by the incident high-energy irradiation. Note, that the initial excess densities are equal; i.e. $\Delta n_1(t=0)=\Delta n_2(t=0)$. Further, the first term describes the generation of electrons and holes with a rate $G_{\mathrm{pulse}}=G\left[\Theta(t)-\Theta\left(t-t_{\mathrm{pulse}}\right)\right]$, where Θ is the Heaviside function making the expression non-zero only during the high-energy irradiating pulse with duration t_{pulse}. Furthermore, ϕ_{n_1} and ϕ_{n_2} denote the fraction of initially generated charges surviving from direct trapping or geminate electron-hole recombination during the 3 MeV electron pulse. Terms containing the factor n_i^2 take into account generation of electron-hole pairs by deviation from the thermodynamic equilibrium carrier density n_i through

absorption of blackbody radiation, thermal excitation, or impact ionization by sufficiently energetic intrinsic thermally excited charge carriers.[71] The intrinsic density of charge carriers is given by $n_i = \sqrt{\left(m_e^* m_h^* k_B^2 T^2 / \pi^2 \hbar^4\right)^{3/2}} \exp\left[-E_g / 2k_B T\right]$ for a three dimensional semiconductor,[152] with m_e^*, m_h^* the effective masses of electrons and holes taken from previous reports.[22, 137] Furthermore, k_B denotes the Boltzmann constant, T the temperature and $\hbar$ is the reduced Planck constant. Note, that Liu *et al.*[29] reported that the inter-chain electronic coupling of Te atomic wires is comparable to the intrachain electronic coupling. This causes Te to behave almost like an isotropic 3D system, rather than a 1D system such as Se, so that the use of the 3D intrinsic carrier density above is substantiated.

The second terms in equations (5.4) and (5.5) take into account trapping and subsequent non-radiative electron-hole recombination according to the Shockley-Read-Hall (SRH) model,[71] neglecting defect parameters (the densities of electrons and holes in case the Fermi energy coincides with the trap level[69]). The parameters $k_{n_1}^{\mathrm{SRH}}$ and $k_{n_2}^{\mathrm{SRH}}$ denote the trapping rate constants for SRH recombination. In an ideal case they are proportional to the trap density and electron- and hole-capture coefficients, which depend upon the thermal velocity of charges.[70] However, the temperature dependence of trapping rate constants may, nevertheless, deviate from the ideal case; e.g. when trapping processes are thermally activated. The third terms in equations (5.4) and (5.5) represent charge trapping with the characteristic rate k_{n_1} (and k_{n_2}), which by themselves yield a stretched-exponential (quasi-exponential or Kohlrausch)[153] decay given by $n(t) = n(t=0)\exp\left[(-kt)^{\beta}\right]$,[154-155] where β is a parameter that characterizes dispersive charge diffusion in an exponential energy landscape. For an exponential distribution of trap site energies of width $k_B T_0$, the β parameter is given by $\beta = T/T_0$.[154, 156-158] The fourth terms in equations (5.4) and (5.5) account for radiative recombination of an electron-hole pair with rate coefficient $k_r = pE_g^2 / (k_B T)^{3/2}$ with p a constant independent of temperature.[70, 104, 159] The decrease of k_r with temperature is understood in terms of the decreasing likelihood of matching equal but opposite momenta of free carriers, imposed by momentum conservation during recombination, as the average thermal energy and hence Fermi vector increases with temperature.[159]

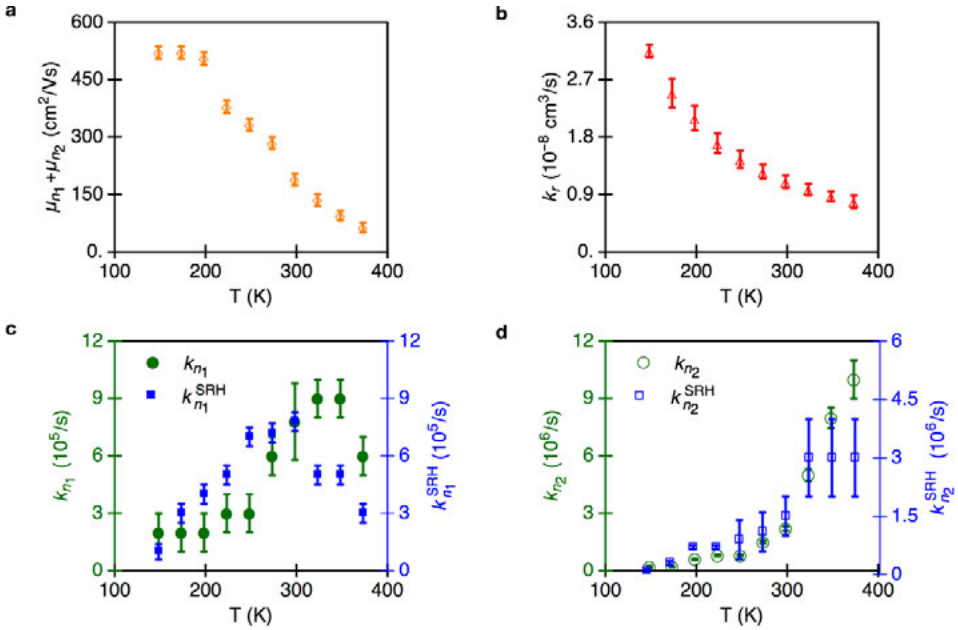

Figure 5.2. Temperature dependence of fitting parameters obtained from the theoretical model: (a) the combined mobility of electrons and holes, (b) radiative recombination rate constant k_r, (c) and (d) SRH recombination rate constant and decay rate for stretched-exponential trapping for electrons or holes (n_1) and their respective counter charges (n_2).

5.3.3 Temperature Dependent Electron and Hole Mobility and Decay Rate Coefficients

Figure 5.1 shows that the theoretical model, given by equations (5.4) and (5.5), reproduces the measured transient conductivities. The fitted parameters, combined electron and hole mobility ($\mu_{n_1}+\mu_{n_2}$), band-to-band radiative recombination (k_r), Shockley-Read-Hall rate constants ($k_{n_1}^{\mathrm{SRH}}$ and $k_{n_2}^{\mathrm{SRH}}$) and characteristic rate constants for stretched exponential decay of charges (k_{n_1} and k_{n_2}) are shown in figure 5.2 as a function of temperature. The trapping rates for electrons and holes cannot be distinguished, as they are interchangeable. In our previous work on Se, electrons and holes could be distinguished because it was known from literature that electrons are trapped faster than holes.[21, 126] Such information is not available for Te and consequently we cannot distinguish electrons and holes. Hence, the charge carrier densities and related rates and mobilities are denoted as n_1 for one type of charge and n_2 for the counter charge.

As mentioned earlier, the numerical fits were found to reproduce the experimental results only for the calculated intrinsic density valid for a three-dimensional system and not for a one-dimensional system, in agreement with the finding of Liu *et al*.[29] Additionally, the numerical fits could only reproduce the experimental data by taking the values for the initial yield of charges (ϕ in equation (5.3)) equal to unity. This implies that the initially generated charges do not undergo geminate recombination to form excitons, as could be expected since the exciton binding energy in Te is only 1.2 meV.[25] Furthermore, the charges are generated far apart in the sample, larger than the critical escape radius determined by the thermal energy.

The mobility obtained at room temperature is 190 ± 20 $\mathrm{cm^2V^{-1}s^{-1}}$. This value is somewhat lower than the values near 700 $\mathrm{cm^2V^{-1}s^{-1}}$ reported for thin layers of 1D and 2D Te nanostructures in field effect transistors.[144, 160] The latter values can be higher than ours due to enhancement of the mobility for thinner samples[160] and/or due to the high charge density in field effect transistor (FET) measurements resulting in filling of trap states. The high mobility in Te may be in part due to the absence of polar optical phonon scattering, which significantly limits the mobility in compound 2D semiconductors.[161] Figure 5.2a depicts that the combined electron and hole mobility decreases with temperature, which is typical for band-like transport. This can be due to the combined effect of various types of electron-phonon scattering processes. Classically, ionized impurity scattering of charges generally occurs due to elastic scattering of charges with ionized shallow-donor impurities in a semiconductor. Due to this scattering, the mobility is expected to increase with $T^{3/2}$ at low temperature.[70] Ionized impurity scattering leads to increase in mobility with temperature, which can be a reason for the initial flatness in the mobility trend up to 200 K together with another process decreasing the mobility with temperature. Above 200 K the mobility decreases due to electron-phonon scattering. The observed decrease in the mobility with temperature in Te is in line with the trends in previous reports.[28, 141]

Figure 5.2b shows the temperature dependence of the second-order band-to-band radiative recombination rate constant (k_r), which decreases with temperature, as expected form theory (see theoretical model section). The numerical fits to the experimental data in figure 5.1 yield a room temperature value of k_r equal to $(1.1 \pm 0.1) \times 10^{-8}$ $\mathrm{cm^3s^{-1}}$. In case of diffusion-limited radiative recombination the

rate constant would be related to the combined mobility of charges according to $k_r = e\left(\mu_{n_1} + \mu_{n_2}\right)\big/\varepsilon_0\varepsilon_r$. Taking $\mu_{n_1} + \mu_{n_2} = 190\ \mathrm{cm^2V^{-1}s^{-1}}$, $\varepsilon_r = 28$,[162] the recombination rate for the diffusion-limited k_r is then estimated to be $1.2\times10^{-5}\ \mathrm{cm^3s^{-1}}$, which is almost 3 orders of magnitude higher than the value obtained from the fitting. Therefore, the radiative recombination in Te is concluded to be a reaction-limited process, rather than a diffusion-limited process.

Figures 5.2c and 5.2d show the temperature dependence of trap-assisted SRH rates, as well as rates to trapping of charges into an energetically exponential distribution of trap sites. Incorporation of two pathways for charge decay *via* trapping is the result of the inability to reproduce our experimental data with either type of processes individually. SRH mostly deals with trap-assisted recombination, implying capture of an electron (or a hole) from the conduction band (or valance band) followed by successive recombination with a hole (or an electron) in the valance band (or conduction band). The associated rate constant $k_{n_1}^{\mathrm{SRH}}$ (or $k_{n_2}^{\mathrm{SRH}}$) depends upon the total trap density N_{t}, and capture coefficients c_n (or c_p) according to the relation $k_{n_{1/2}}^{\mathrm{SRH}} = c_{n_{1/2}} N_{\mathrm{t}}$, where $c_{n_{1/2}} = \sigma_{n_{1/2}} \left\langle \nu_{\mathrm{th}} \right\rangle$. $\sigma_{n_{1/2}}$ is the electron or hole capture cross-section and $\left\langle \nu_{\mathrm{th}} \right\rangle$ the thermal velocity of charges, given by $\left\langle \nu_{\mathrm{th}} \right\rangle = \sqrt{\left(3k_{\mathrm{B}}T/m_{e/h}^{*}\right)}$.[70] Therefore, the SRH recombination rate increases with temperature, in contrast to our results in figure 5.2c where a decrease with temperature is observed above 300 K. The decrease could be due to filling of trap sites at higher temperatures by thermally generated intrinsic charges. These competing processes could give rise to a trend as can be clearly seen for one of the charges in figure 5.2c in blue color. For the case of the other type of charges, as shown in figure 5.2d, the thermally generated intrinsic charges may not simply fill the traps, thus, the rate constant does not decrease at higher temperatures. The stretched exponential parameter T_0 is found to be $500\pm100\ \mathrm{K}$, corresponding to an energetic width of $43\pm9\ \mathrm{meV}$. It is also observed that the stretched exponential parts in the equations (5.4) and (5.5) only determine the longer time scale of the conductivity signals in the range of roughly 25 ns to 40 ns. The temperature dependence of characteristic trapping rate constant of the charges $k_{n_{1/2}}$, as shown in green color in figure 5.2c, is not very pronounced for one type of charges, while it is strongly thermally activated for the other type of charges in figure 5.2d. This is similar to the trends observed for trapping of charges in Selenium.[21]

5.3.4 Radiative Yield of Charges

The radiative yield (RY), by definition, is the ratio of the number of photons emitted from the sample and the net number of electrons and holes annihilated radiatively or non-radiatively equaling the generated charge carrier number. The ratio for the instantaneous radiative yield ($\mathrm{RY}(t)$) is given by

$$\mathrm{RY}(t) = 2k_r\left[n_1(t)n_2(t) - n_i^2\right] \Bigg/ \left(2\frac{k_{n_1}^{\mathrm{SRH}} k_{n_2}^{\mathrm{SRH}}\left[n_1(t)n_2(t) - n_i^2\right]}{k_{n_1}^{\mathrm{SRH}} n_1(t) + k_{n_2}^{\mathrm{SRH}} n_2(t)} + \frac{\beta_{n_1}\left(k_{n_1}t\right)^{\beta_{n_1}}}{t} + \frac{\beta_{n_2}\left(k_{n_2}t\right)^{\beta_{n_2}}}{t} + 2k_r\left[n_1(t)n_2(t) - n_i^2\right] \right), \tag{5.6}$$

with $n(t) = \left(n_i + \Delta n(t)\right)$. Integrating the numerator and denominator over time yields an estimate for the total (time-integrated) radiative yield (RY), as discussed later. From the theoretical analysis, the 5 ns pulse (peak value in figure 5.1a) yields excess densities of electrons and holes equal to density of $\left(3.7 \pm 0.5\right) \times 10^{15}$ cm^{-3}. In order to compare the significance of decay, namely radiative recombination, SRH recombination and stretched-exponential decay, the instantaneous radiative yield expression can be further rewritten, taking the densities of electrons and holes equal, as they fall in the aforementioned uncertainty. This simplification enables direct comparison of the processes in the same units. In such a case, the second-order radiative decay rate can be simplified into $k_r\left[\Delta n(t) + 2n_i\right]\Delta n(t)$ corresponding to a pseudo first order decay with rate $k_r\left[\Delta n(t) + 2n_i\right]$. At room temperature, the obtained value for k_r is $\left(1.1 \pm 0.1\right) \times 10^{-8}$ $\mathrm{cm}^3\mathrm{s}^{-1}$, which yields a value for $k_1^{\mathrm{pseudo}}\left(t = 5\ \mathrm{ns}\right) = k_r\left[\Delta n\left(t = 5\ \mathrm{ns}\right) + 2n_i\right] = \left(5.8 \pm 0.2\right) \times 10^7\ \mathrm{s}^{-1}$, while for long-time scale the value is $k_1^{\mathrm{pseudo}}\left(t \to \infty\right) = 2k_r n_i = \left(1.78 \pm 0.04\right) \times 10^7\ \mathrm{s}^{-1}$. Additionally, the room temperature SRH recombination rate and the characteristic decay rate by stretched-exponential decay are $\left(7.8 \pm 0.47\right) \times 10^5\ \mathrm{s}^{-1}$ and $\left(1.0 \pm 0.5\right) \times 10^5\ \mathrm{s}^{-1}$, respectively, and hence considerably lower than the number above. Using the values for the decay rate constants, $\Delta n\left(t = 5\ \mathrm{ns}\right)$ and equation (5.6), the obtained value for the instantaneous $\mathrm{RY}\left(t = 5\ \mathrm{ns}\right)$ is ca. 0.98 (or 98 %),

which decreases to ca. 0.92 (or 92 %) for long-time scale (~40 ns), where most of the pulse generated charges have decayed.

The total RY is obtained by integrating the numerator and denominator, as shown in the following equation

$$\mathrm{RY}=\left(\int_{t_{\mathrm{pulse}}}^{\infty} 2k_r\left[2n_i+\Delta n(t)\right]\mathrm{d}t\right)\Bigg/\left(\int_{t_{\mathrm{pulse}}}^{\infty}\left[2\frac{\left[2n_i+\Delta n(t)\right]}{\left(\tau_{n_1}^{\mathrm{SRH}}+\tau_{n_2}^{\mathrm{SRH}}\right)\left[n_i+\Delta n(t)\right]}+2k_r\left[2n_i+\Delta n(t)\right]+\frac{\beta_{n_1}\left(k_{n_1}t\right)^{\beta_{n_1}}}{t}+\frac{\beta_{n_2}\left(k_{n_2}t\right)^{\beta_{n_2}}}{t}\right]\mathrm{d}t\right) \quad (5.7)$$

In the above equation, $\tau_{n_1}^{\mathrm{SRH}}$ and $\tau_{n_2}^{\mathrm{SRH}}$ are inverse of the corresponding rates $k_{n_1}^{\mathrm{SRH}}$ and $k_{n_2}^{\mathrm{SRH}}$. Equation (5.7) yields a total RY of 0.98 (or 98 %). This result indicates predominant strong radiative recombination in van der Waals bound chains of Te.

For excess densities of electrons and holes on the order of 10^{15} cm^{-3} the RY yield is much higher than for a similar band gap material such as black phosphorus[104], where a comparable RY can be achieved only at an excess density of 10^{19} cm^{-3}. The high RY at a density of 10^{15} cm^{-3} together with an appreciably high carrier mobility makes Te a material of high potential in efficient infrared LEDs or laser diodes.[77] Note, that a high current is needed in laser diodes to achieve population inversion. On the other hand it is suitable for very efficient infrared photodetectors with high bandwidth and low Johnson noise at high frequency due to appreciably high carrier mobility, as e.g. in a photo resistor the noise (voltage) amplitude is proportional to the square root of the inverse mobility *via* $u_{\mathrm{Noise}}\approx\sqrt{4k_{\mathrm{B}}TR}=2L\sqrt{k_{\mathrm{B}}T/e\left(n_1\mu_{n_1}+n_2\mu_{n_2}\right)}$ with the detector resistance R of a photodetector of length L.[145] At low (modulation) frequencies and/or low temperatures $1/f$ noise limits the detector performance resulting in a noise current $I_{\mathrm{Noise}}=\sqrt{QYP_S/2h\nu\Delta f}$,[145] with P_S the infrared signal power, Δf the bandwidth and $h\nu$ the photon energy. From the last equation it is apparent, that a high quantum yield (QY), as measured in Te, is desirable to obtain a high S/N ratio, since the signal is proportional to the QY and hence $S/N\propto\sqrt{QY}$. Hence,

Te is an interesting material for applications due to high quantum yield and appreciably high mobility.

5.4 Conclusions

The mobility of charges in Te is thermally deactivated with a room temperature value of 190 ± 20 $cm^2V^{-1}s^{-1}$. Charges decay with near unity quantum yield *via* radiative recombination. Te, being a quasi one-dimensional van der Waals material, has a potential for in-depth studies of interesting optoelectronic properties with isolated atomic chains. Such chains can in principle be obtained by liquid exfoliation, which offers possibilities for large-scale production. Furthermore, the appreciably high mobility, and near unity radiative yield opens the potential for applications in nanoelectronics like as efficient far infrared detectors with high bandwidth or lasers with high efficiency. Further, far infrared imaging applications replacing micro bolometers may be of interest.

Appendix

A1. Stopping power of electrons

As discussed in section 1.5, in pulse-radiolysis microwave conductivity studies it is important to generate uniformly distributed charges in the sample. However, in case the stopping power of the sample is high, the primary electrons (3 MeV from van de Graaf accelerator) lose a larger fraction of their energy near the side where they enter the sample and a significant of the incident electrons may even stop inside the sample. This leads to a non-uniform distribution of secondary (tertiary etc.) charges. In addition stopping of primary electrons in the sample defies charge-neutrality. Figure A1.1 shows a schematic diagram of a non-uniform distribution of charges along the vertical direction.

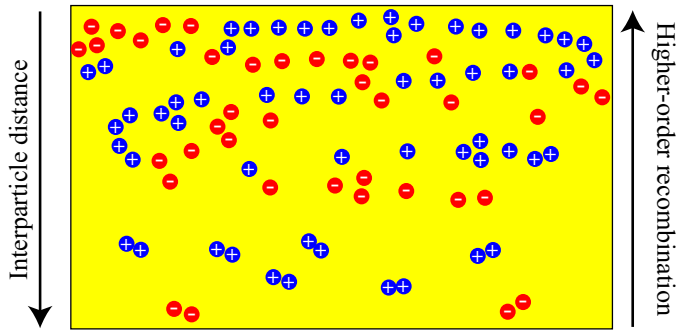

Figure A1.1 Schematic diagram depicting a non-uniform distribution of charges along the vertical direction.

The non-uniformity of secondary etc. charges along the direction of irradiation (vertical in figure A1.1) results in different inter-particle distances. In the high density region the interparticle distances between electrons and holes are shorter than in a region of low density. Second-order recombination of charges is more pronounced in a region with higher charge density. This causes the recombination kinetics of charges to vary along the direction of irradiation, which complicates quantitative analysis of the decay of the microwave conductivity with time.

The stopping power of 3 MeV electrons can be calculated as discussed in section 5.2. The stopping power of a material is the average amount of energy dissipated by the incident charged particles (with energy E) per unit length x; i.e.

$S(E) = -\mathrm{d}E/\mathrm{d}x$. The energy dissipation occurs mainly due to collision of incident electrons with the electrons in the sample and due to emission of radiation. We calculated the penetration depth of primary electrons in our samples, using equations (5.1) and (5.2 Using relativistic quantum mechanics Bethe[60] derived the following expression for the stopping power of a medium for heavy charged particles.

$$S(E) = -\frac{\mathrm{d}E}{\mathrm{d}x} = \frac{4\pi k_0^2 z^2 e^4 n}{mc^2\beta^2}\left[\ln\frac{2mc^2\beta^2}{I\left(1-\beta^2\right)} - \beta^2\right], \qquad \text{(A1.1)}$$

where

$k_0 = 1/4\pi\varepsilon_0 = 8.99\times10^9\ \mathrm{Nm^2C^{-2}}$,

$z =$ atomic number of the heavy charged particles,

$e = 1.60\times10^{-19}\,C =$ elementary charge,

$n =$ number of electrons per unit volume in the medium,

$m = 9.11\times10^{-31}\,\mathrm{kg} =$ rest mass of electron,

$c = 3.00\times10^8\ \mathrm{ms^{-1}} =$ speed of light in vacuum,

$\beta = V/c =$ speed of the particle relative to c,

$I =$ mean excitation energy of the medium.

The collisional stopping power for electrons is different from that for heavy charged particles. Heavy charged particles continuously lose small fractions of their energy *via* electronic collisions inducing ionizations and/or electronic excitations in a medium, with negligible deflection. However, electrons lose a large fraction of their energies in a single collision with electrons in the sample, which results into large deflections. Due to this, electrons deflect at large angles. In addition, electrons get scattered by nuclei resulting into generation of bremsstrahlung. Moreover, upon collision of an incident electron with an electron in the sample, the identity of the former and the latter cannot be distinguished. Taking this indistinguishability into account gives stopping power for electrons given by equation (A1.2).[60, 149]

$$S(E)_{\mathrm{col}} = -\left(\frac{\mathrm{d}E}{\mathrm{d}x}\right)_{\mathrm{col}} = \frac{4\pi k_0^2 e^4 n}{mc^2\beta^2}\left[\ln\left(\frac{mc^2\tau\sqrt{\tau+2}}{\sqrt{2}I}\right) + F(\beta)\right],$$

where ,

$$F(\beta) = \frac{1-\beta^2}{2}\left[1+\frac{\tau^2}{8}-(2\tau+1)\ln 2\right] \text{ and } \tau = \frac{T}{mc^2} \qquad \text{(A1.2)}$$

In A1.2, T is the kinetic energy of the incident electrons. The equation in (A1.2) can further be simplified to the following, by putting the values of various constants mentioned above.

$$S(E)_{\text{col}} = -\left(\frac{\mathrm{d}E}{\mathrm{d}x}\right)_{\text{col}} = \frac{5\times10^{-31}n}{\beta^2}\left[\ln\left(3.61\times10^{5}\tau\sqrt{\tau+2}\right) - \ln I_{\text{eV}} + F^{-}(\beta)\right] \text{ MeV cm}^{-1} \qquad \text{(A1.3)}$$

The total stopping power for electrons in materials is due to collisional as well as radiative processes, so that

$$\left(-\frac{\mathrm{d}E}{\mathrm{d}x}\right)_{\text{total}} = \left(-\frac{\mathrm{d}E}{\mathrm{d}x}\right)_{\text{col}} + \left(-\frac{\mathrm{d}E}{\mathrm{d}x}\right)_{\text{rad}}. \qquad \text{(A1.4)}$$

In contrast to collisional stopping power, an analytical expression to estimate the radiative stopping power $\left(-\mathrm{d}E/\mathrm{d}x\right)_{\text{rad}}$ does not exist. Numerical analysis of experiments on electron stopping in water has established that the radiative energy-loss rate in a material is proportional to n and hence Z. Additionally, the radiative energy-loss rate increases nearly linearly with incident electron energy. For in-depth knowledge about stopping power, linear energy transfer and radiation chemistry, it is recommended to consult books on radiation chemistry such as those by A. Hummel,[66] J. Turner[60] and A. Mozumder.[149]

From equation A1.3, the values of the stopping power (in MeVcm^{-1}) of 3 MeV electrons in various media are calculated and compared with NIST (ESTAR) values as shown below.

Material	Stopping power (A1.4)	Stopping power (ESTAR)*
Water	1.86	1.88
Tellurium	8.61	8.67

**Note: The ESTAR program can be used to calculate the stopping power, density effect parameters, range, and radiation yield for electrons in various materials. A web-only version of the program is available at the website of National Institute of Standards and Technology (NIST) with the following link: (http://physics.nist.gov/PhysRefData/Star/Text/ESTAR.html)*

The obtained dependence of the stopping power on the kinetic energy of electrons is shown in figure A1.2.

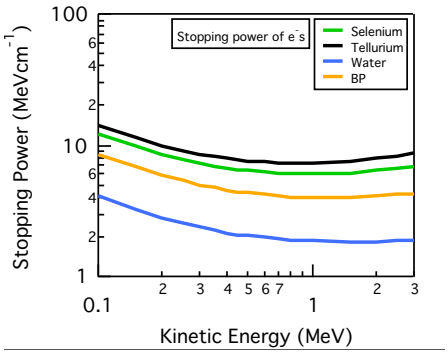

Figure A1.2 The stopping power of electrons in various materials as a function of the kinetic energy of electrons in the range of 0.1 MeV to 3 MeV.

It can be seen in figure A1.2 that the stopping power first decreases with the energy of incident electrons and then increases with energy. Further, it depends on the type of materials primarily due to variation of the electron density n. Calculation of the stopping power from equations (5.1) and (5.2) yields similar values as those from equations (A1.3).

To complement the above described calculations, a Monte Carlo Simulation package (CASINO**) was used to simulate the trajectories of 3 MeV electrons in a system composed of a 0.4 mm layer of copper, 3.5 mm layer of sample and 1 mm of copper, mimicking the sample configuration used in microwave conductivity experiments. Figure A1.3 shows a comparison of trajectories of primary electrons in water and tellurium.

**Note: CASINO (monte CArlo Simulation of electroN trajectory in sOlids) is a Monte Carlo package to simulate trajectories of electrons in solid materials. This simulation was performed as an alternative to the calculations done in the earlier section to check the obtained values of the stopping power and the penetration depth of electrons.

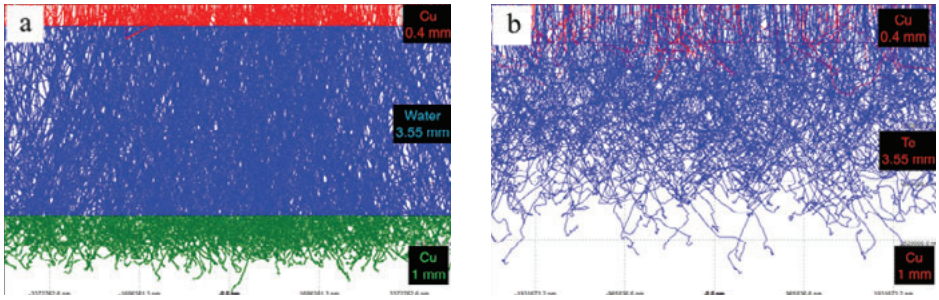

Figure A1.3 Electron trajectories in (a) water and (b) tellurium.

Figure A1.3 shows that 3 MeV electrons can easily pass through a water sample of thickness 3.5 mm. In tellurium, due to higher stopping power, the 3 MeV electrons are stopped within the sample of thickness 3.5 mm (generic sample holder as shown in figure A1.4(a)). In such a case, the distribution of secondary charges generated by the primary electrons would no longer be uniform, therefore the sample groove was reduced from 3.5 mm to 1 mm to avoid non-uniform generation of secondary charges, as shown in figure A1.4(b).

(a) Configuration C1 (b) Configuration C2

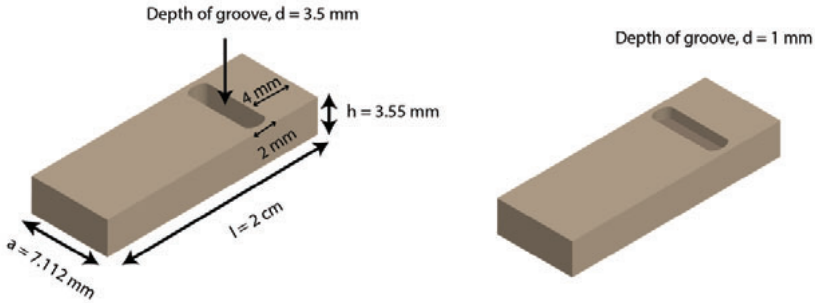

Figure A1.4 (a) Generic sample holder, (b) modified sample holder.

A similar Monte Carlo simulation of electron trajectories was performed for the modified sample holder filled with tellurium. Figure A1.5 shows the obtained trajectories of 3 MeV electrons passing through 0.4 mm copper, 1 mm tellurium, 2.5 mm PMMA and 1 mm copper, respectively.

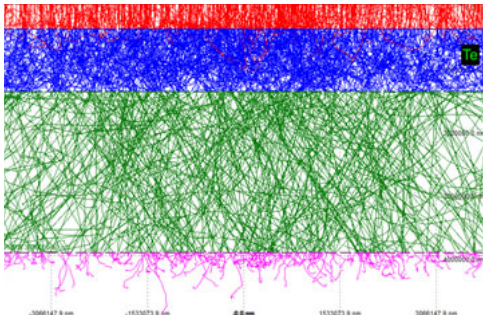

Figure A1.5 Trajectories of 3 MeV electrons in tellurium filled in the C2 configuration of sample holder.

The modification of the sample holder enabled us to perform pulse-radiolysis experiments on more dense materials such as tellurium, while avoiding the complication of non-uniform charge generation.

A2. Schematic diagram of the PR-TRMC setup

Figure A1.6 shows a schematic diagram of the pulse-radiolysis transient microwave conductivity setup, consisting of a van de Graaff electron accelerator and a K_a-band microwave system.

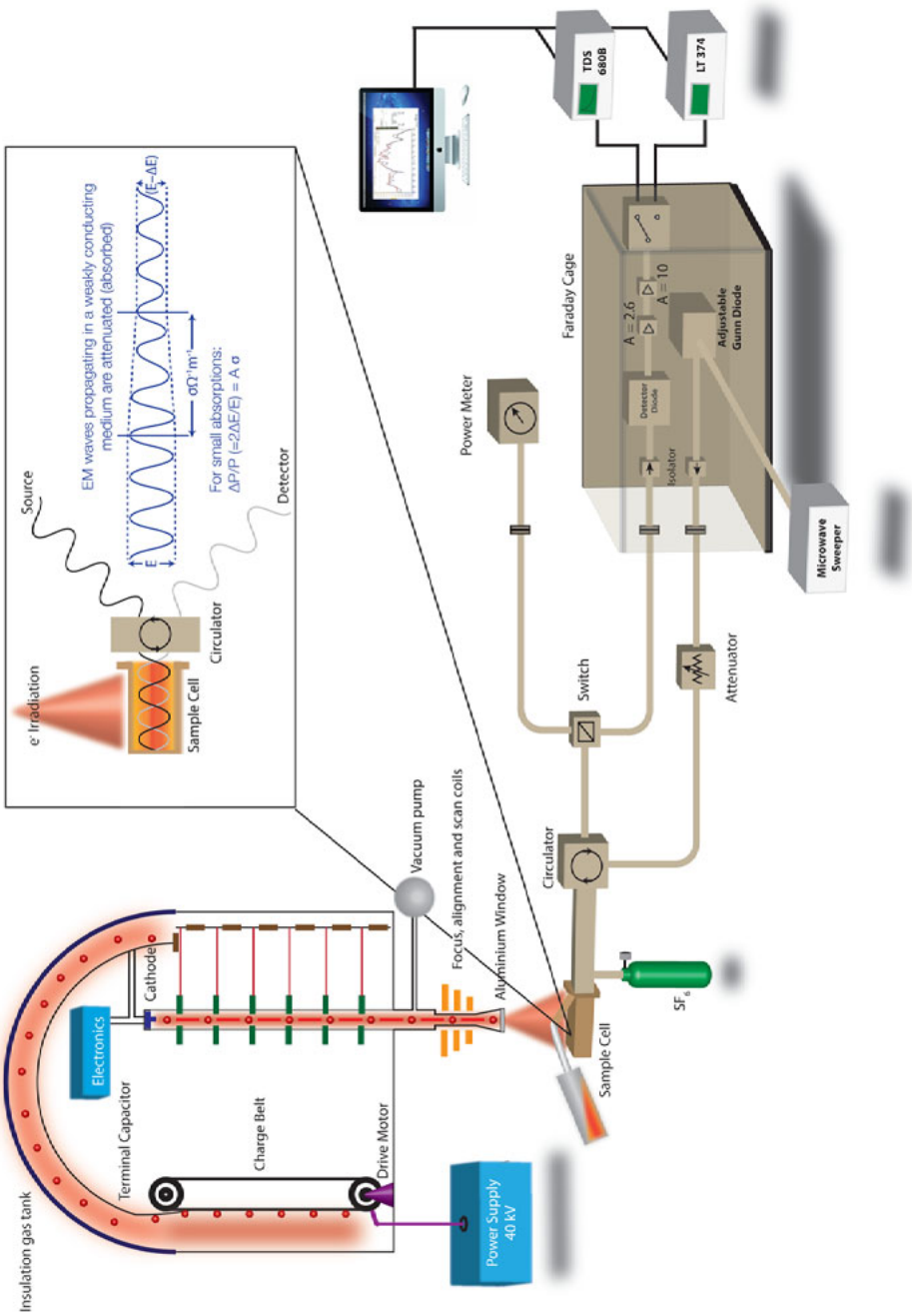

A1.6 A schematic diagram of van de Graaff electron accelerator with microwave conductivity setup.

References

1. Li, S. S., *Semiconductor Physical Electronics*. Springer New York: 2006.
2. Schultz, O.; Mette, A.; Preu, R.; Glunz, S. W., Silicon Solar Cells With Screen-Printed Front Side Metallization Exceeding 19% Efficiency. In *22nd European Photovoltaic Solar Energy Conference and Exhibition*, Milano, 2007.
3. Shockley, W.; Queisser, H. J., Detailed Balance Limit of Efficiency of p-n Junction Solar Cells. *Journal of Applied Physics* **1961,** *32* (3), 510-519.
4. Kulkarni, A.; Evers, W. H.; Tomić, S.; Beard, M. C.; Vanmaekelbergh, D.; Siebbeles, L. D. A., Efficient Steplike Carrier Multiplication in Percolative Networks of Epitaxially Connected PbSe Nanocrystals. *ACS Nano* **2018,** *12* (1), 378-384.
5. Barati, F.; Grossnickle, M.; Su, S.; Lake, R. K.; Aji, V.; Gabor, N. M., Hot carrier-enhanced interlayer electron–hole pair multiplication in 2D semiconductor heterostructure photocells. *Nature Nanotechnology* **2017,** *12*, 1134.
6. Hanna, M. C.; Nozik, A. J., Solar conversion efficiency of photovoltaic and photoelectrolysis cells with carrier multiplication absorbers. *Journal of Applied Physics* **2006,** *100* (7), 074510.
7. Schaller, R. D.; Klimov, V. I., High Efficiency Carrier Multiplication in PbSe Nanocrystals: Implications for Solar Energy Conversion. *Physical Review Letters* **2004,** *92* (18), 186601.
8. Ellingson, R. J.; Beard, M. C.; Johnson, J. C.; Yu, P.; Micic, O. I.; Nozik, A. J.; Shabaev, A.; Efros, A. L., Highly Efficient Multiple Exciton Generation in Colloidal PbSe and PbS Quantum Dots. *Nano Letters* **2005,** *5* (5), 865-871.
9. Murphy, J. E.; Beard, M. C.; Norman, A. G.; Ahrenkiel, S. P.; Johnson, J. C.; Yu, P.; Mićić, O. I.; Ellingson, R. J.; Nozik, A. J., PbTe Colloidal Nanocrystals: Synthesis, Characterization, and Multiple Exciton Generation. *Journal of the American Chemical Society* **2006,** *128* (10), 3241-3247.

10. Schaller, R. D.; Sykora, M.; Pietryga, J. M.; Klimov, V. I., Seven Excitons at a Cost of One: Redefining the Limits for Conversion Efficiency of Photons into Charge Carriers. *Nano Letters* **2006,** *6* (3), 424-429.

11. Schaller, R. D.; Petruska, M. A.; Klimov, V. I., Effect of electronic structure on carrier multiplication efficiency: Comparative study of PbSe and CdSe nanocrystals. *Applied Physics Letters* **2005,** *87* (25), 253102.

12. Qiao, J.; Kong, X.; Hu, Z.-X.; Yang, F.; Ji, W., High-mobility transport anisotropy and linear dichroism in few-layer black phosphorus. *Nat Commun* **2014,** *5*.

13. *Silicon (Si), electron mobility: Datasheet from Landolt-Börnstein - Group III Condensed Matter · Volume 41A1β: "Group IV Elements, IV-IV and III-V Compounds. Part b - Electronic, Transport, Optical and Other Properties" in SpringerMaterials (https://dx.doi.org/10.1007/10832182_456)*, Springer-Verlag Berlin Heidelberg.

14. *Amorphous silicon (a-Si) drift mobility: Datasheet from Landolt-Börnstein - Group III Condensed Matter · Volume 41E: "Ternary Compounds, Organic Semiconductors" in SpringerMaterials (https://dx.doi.org/10.1007/10717201_942)*, Springer-Verlag Berlin Heidelberg.

15. Britnell, L.; Ribeiro, R. M.; Eckmann, A.; Jalil, R.; Belle, B. D.; Mishchenko, A.; Kim, Y. J.; Gorbachev, R. V.; Georgiou, T.; Morozov, S. V.; Grigorenko, A. N.; Geim, A. K.; Casiraghi, C.; Neto, A. H. C.; Novoselov, K. S., Strong Light-Matter Interactions in Heterostructures of Atomically Thin Films. *Science* **2013,** *340* (6138), 1311.

16. Bernardi, M.; Palummo, M.; Grossman, J. C., Extraordinary Sunlight Absorption and One Nanometer Thick Photovoltaics Using Two-Dimensional Monolayer Materials. *Nano Letters* **2013,** *13* (8), 3664-3670.

17. Novoselov, K. S.; Geim, A. K.; Morozov, S. V.; Jiang, D.; Zhang, Y.; Dubonos, S. V.; Grigorieva, I. V.; Firsov, A. A., Electric Field Effect in Atomically Thin Carbon Films. *Science* **2004,** *306* (5696), 666-669.

18. Schwierz, F., Graphene transistors. *Nature Nanotechnology* **2010,** *5*, 487.

19. Geim, A. K.; MacDonald, A. H., Graphene: Exploring carbon flatland. *Physics Today* **2007,** *60* (8), 35-41.
20. Ajayan, P.; Kim, P.; Banerjee, K., Two-dimensional van der Waals materials. *Physics Today* **2016,** *69* (9), 38-44.
21. Bhaskar, P.; Achtstein, A. W.; Diedenhofen, S. L.; Siebbeles, L. D. A., Mobility and decay dynamics of charge carriers in one-dimensional selenium van der Waals solid. *Journal of Physical Chemistry C* **2017,** *121* (34), 18917-18921.
22. Caldwell, R. S.; Fan, H. Y., Optical Properties of Tellurium and Selenium. *Physical Review* **1959,** *114* (3), 664-675.
23. Gates, B.; Mayers, B.; Cattle, B.; Xia, Y., Synthesis and Characterization of Uniform Nanowires of Trigonal Selenium. *Advanced Functional Materials* **2002,** *12* (3), 219-227.
24. Luo, L.-B.; Yang, X.-B.; Liang, F.-X.; Jie, J.-S.; Li, Q.; Zhu, Z.-F.; Wu, C.-Y.; Yu, Y.-Q.; Wang, L., Transparent and flexible selenium nanobelt-based visible light photodetector. *CrystEngComm* **2012,** *14* (6), 1942-1947.
25. Stuke, J., Recent Progress in the Physics of Selenium and Tellurium. In *The Physics of Selenium and Tellurium*, Pergamon: 1969; pp 3-20.
26. Churchill, H. O. H.; Salamo, G. J.; Yu, S.-Q.; Hironaka, T.; Hu, X.; Stacy, J.; Shih, I., Toward Single Atom Chains with Exfoliated Tellurium. *Nanoscale Research Letters* **2017,** *12* (1), 488.
27. Du, Y.; Qiu, G.; Wang, Y.; Si, M.; Xu, X.; Wu, W.; Ye, P. D., One-Dimensional van der Waals Material Tellurium: Raman Spectroscopy under Strain and Magneto-Transport. *Nano Letters* **2017,** *17* (6), 3965-3973.
28. Lin, S.; Li, W.; Chen, Z.; Shen, J.; Ge, B.; Pei, Y., Tellurium as a high-performance elemental thermoelectric. *Nature Communications* **2016,** *7*, 10287.
29. Liu, Y.; Wu, W.; Goddard, W. A., Tellurium: Fast Electrical and Atomic Transport along the Weak Interaction Direction. *Journal of the American Chemical Society* **2018,** *140* (2), 550-553.
30. Infelta, P. P.; de Haas, M. P.; Warman, J. M., The study of the transient conductivity of pulse irradiated dielectric liquids on a nanosecond

timescale using microwaves. *Radiation Physics and Chemistry (1977)* **1977,** *10* (5), 353-365.
31. Hoofman, R. J. O. M.; Siebbeles, L. D. A.; Haas, M. P. d.; Hummel, A.; Bloor, D., Anisotropy of the charge-carrier mobility in polydiacetylene crystals. *The Journal of Chemical Physics* **1998,** *109* (5), 1885-1893.
32. Warman, J. M.; de Haas, M. P.; Wentinck, H. M., The study of radiation induced conductivity changes in microheterogeneous materials using microwaves. *International Journal of Radiation Applications and Instrumentation. Part C. Radiation Physics and Chemistry* **1989,** *34* (4), 581-586.
33. Shockley, W.; Read, W. T., Statistics of the Recombinations of Holes and Electrons. *Physical Review* **1952,** *87* (5), 835-842.
34. Hall, R. N., Electron-Hole Recombination in Germanium. *Physical Review* **1952,** *87* (2), 387-387.
35. Landsberg, P. T., *Recombination in Semiconductors*. Cambridge University Press: Cambridge, 1992.
36. Butler, S. Z.; Hollen, S. M.; Cao, L. Y.; Cui, Y.; Gupta, J. A.; Gutierrez, H. R.; Heinz, T. F.; Hong, S. S.; Huang, J. X.; Ismach, A. F.; Johnston-Halperin, E.; Kuno, M.; Plashnitsa, V. V.; Robinson, R. D.; Ruoff, R. S.; Salahuddin, S.; Shan, J.; Shi, L.; Spencer, M. G.; Terrones, M.; Windl, W.; Goldberger, J. E., Progress, Challenges, and Opportunities in Two-Dimensional Materials Beyond Graphene. *ACS Nano* **2013,** *7* (4), 2898-2926.
37. Zhang, H., Ultrathin Two-Dimensional Nanomaterials. *ACS Nano* **2015,** *9* (10), 9451-9469.
38. Bhimanapati, G. R.; Lin, Z.; Meunier, V.; Jung, Y.; Cha, J.; Das, S.; Xiao, D.; Son, Y.; Strano, M. S.; Cooper, V. R.; al, e., Recent Advances in Two-Dimensional Materials beyond Graphene. *ACS Nano* **2015,** *9* (12), 11509-11539.
39. Shu, H.; Li, Y.; Niu, X.; Wang, J., The stacking dependent electronic structure and optical properties of bilayer black phosphorus. *Physical Chemistry Chemical Physics* **2016,** *18* (8), 6085-6091.
40. Carroll, E. C.; Compton, O. C.; Madsen, D.; Osterloh, F. E.; Larsen, D. S., Ultrafast Carrier Dynamics in Exfoliated and Functionalized

Calcium Niobate Nanosheets in Water and Methanol. *The Journal of Physical Chemistry C* **2008,** *112* (7), 2394-2403.

41. ten Cate, S.; Liu, Y.; Suchand Sandeep, C. S.; Kinge, S.; Houtepen, A. J.; Savenije, T. J.; Schins, J. M.; Law, M.; Siebbeles, L. D. A., Activating Carrier Multiplication in PbSe Quantum Dot Solids by Infilling with Atomic Layer Deposition. *The Journal of Physical Chemistry Letters* **2013,** *4* (11), 1766-1770.

42. Xiao, J.; Long, M.; Zhang, X.; Zhang, D.; Xu, H.; Chan, K. S., First-Principles Prediction of the Charge Mobility in Black Phosphorus Semiconductor Nanoribbons. *The Journal of Physical Chemistry Letters* **2015,** *6* (20), 4141-4147.

43. Ling, X.; Wang, H.; Huang, S.; Xia, F.; Dresselhaus, M. S., The renaissance of black phosphorus. *Proceedings of the National Academy of Sciences* **2015,** *112* (15), 4523-4530.

44. Churchill, H. H.; Jarillo-Herrero, P., Two-Dimensional Crystals Phosphorus joins the familly. *Nature Nanotechnology* **2014,** *9* (5), 330-331.

45. Woomer, A. H.; Farnsworth, T. W.; Hu, J.; Wells, R. A.; Donley, C. L.; Warren, S. C., Phosphorene: Synthesis, Scale-Up, and Quantitative Optical Spectroscopy. *ACS Nano* **2015,** *9* (9), 8869-8884.

46. Liu, H.; Du, Y.; Deng, Y.; Ye, P. D., Semiconducting black phosphorus: synthesis, transport properties and electronic applications. *Chemical Society Reviews* **2015,** *44* (9), 2732-2743.

47. Castellanos-Gomez, A., Why all the fuss about 2D semiconductors? *Nature Photon*. **2016,** *10*, 202-204.

48. Bridgman, P. W., Two New Modifications of Phosphorus. *Journal of the American Chemical Society* **1914,** *36* (7), 1344-1363.

49. Morita, A., Semiconducting black phosphorus. *Appl. Phys. A* **1986,** *39* (4), 227-242.

50. Wang, V.; Liu, Y. C.; Kawazoe, Y.; Geng, W. T., Role of Interlayer Coupling on the Evolution of Band Edges in Few-Layer Phosphorene. *The Journal of Physical Chemistry Letters* **2015,** *6* (24), 4876-4883.

51. Cai, Y.; Zhang, G.; Zhang, Y.-W., Layer-dependent Band Alignment and Work Function of Few-Layer Phosphorene. *Scientific Reports* **2014,** *4*, 6677.

52. Liu, H.; Neal, A. T.; Zhu, Z.; Luo, Z.; Xu, X.; Tománek, D.; Ye, P. D., Phosphorene: An Unexplored 2D Semiconductor with a High Hole Mobility. *ACS Nano* **2014,** *8* (4), 4033-4041.
53. Yang, J.; Xu, R.; Pei, J.; Myint, Y. W.; Wang, F.; Wang, Z.; Zhang, S.; Yu, Z.; Lu, Y., Optical tuning of exciton and trion emissions in monolayer phosphorene. *Light Sci Appl* **2015,** *4*, e312.
54. Tran, V.; Soklaski, R.; Liang, Y.; Yang, L., Layer-controlled band gap and anisotropic excitons in few-layer black phosphorus. *Physical Review B* **2014,** *89* (23), 235319.
55. Castellanos-Gomez, A.; Vicarelli, L.; Prada, E.; Island, J. O.; Narasimha-Acharya, K. L.; Blanter, S. I.; Groenendijk, D. J.; Buscema, M.; Steele, G. A.; Alvarez, J. V.; Zandbergen, H. W.; Palacios, J. J.; van der Zant, H. S. J., Isolation and characterization of few-layer black phosphorus. *2D Materials* **2014,** *1* (2).
56. Das, S.; Zhang, W.; Demarteau, M.; Hoffmann, A.; Dubey, M.; Roelofs, A., Tunable Transport Gap in Phosphorene. *Nano Letters* **2014,** *14* (10), 5733-5739.
57. Wu, J.; Koon, G. K. W.; Xiang, D.; Han, C.; Toh, C. T.; Kulkarni, E. S.; Verzhbitskiy, I.; Carvalho, A.; Rodin, A. S.; Koenig, S. P.; al, e., Colossal Ultraviolet Photoresponsivity of Few-Layer Black Phosphorus. *ACS Nano* **2015,** *9* (8), 8070-8077.
58. Ge, S.; Li, C.; Zhang, Z.; Zhang, C.; Zhang, Y.; Qiu, J.; Wang, Q.; Liu, J.; Jia, S.; Feng, J.; al, e., Dynamical Evolution of Anisotropic Response in Black Phosphorus under Ultrafast Photoexcitation. *Nano Letters* **2015,** *15* (7), 4650-4656.
59. Warman, J. M.; de Haas, M. P.; Dicker, G.; Grozema, F. C.; Piris, J.; Debije, M. G., Charge Mobilities in Organic Semiconducting Materials Determined by Pulse-Radiolysis Time-Resolved Microwave Conductivity: π-Bond-Conjugated Polymers versus π–π-Stacked Discotics. *Chemistry of Materials* **2004,** *16* (23), 4600-4609.
60. Turner, J. E., In *Atoms, Radiation, and Radiation Protection*, Wiley-VCH Verlag GmbH & Co. KGaA: 2007.
61. Warman, J. M.; de Haas, M. P.; Dicker, G.; Grozema, F. C.; Piris, J.; Debije, M. G., Charge Mobilities in Organic Semiconducting Materials Determined by Pulse-Radiolysis Time-Resolved Microwave

Conductivity: π-Bond-Conjugated Polymers versus π–π-Stacked Discotics. *Chemistry of Materials* **2004,** *16* (23), 4600-4609.

62. Infelta, P. P.; de Haas, M. P.; Warman, J. M., Study of Transient Conductivity of Pulse Irradiated Dielectric Liquids on a Nanosecond Timescale Using Microwaves. *Radiation Physics and Chemistry* **1977,** *10* (5-6), 353-365.

63. Hoofman, R.; Siebbeles, L. D. A.; de Haas, M. P.; Hummel, A.; Bloor, D., Anisotropy of the charge-carrier mobility in polydiacetylene crystals. *J. Chem. Phys.* **1998,** *109* (5), 1885-1893.

64. Grozema, F. C.; Hoofman, R. J. O. M.; Candeias, L. P.; de Haas, M. P.; Warman, J. M.; Siebbeles, L. D. A., The Formation and Recombination Kinetics of Positively Charged Poly(phenylene vinylene) Chains in Pulse-Irradiated Dilute Solutions. *The Journal of Physical Chemistry A* **2003,** *107* (31), 5976-5986.

65. Berger, L. I., *Semiconductor Materials*. CRC Press: Boca Raton, 1997; Vol. 1.

66. Hummel, A., *Radiation Chemistry : The Chemical Effects of Ionizing Radiation and Their Effects*. IRLTUD: Delft, 1995.

67. Alig, R. C.; Bloom, S.; Struck, C. W., Scattering by ionization and phonon emission in semiconductors. *Physical Review B* **1980,** *22* (12), 5565-5582.

68. Polavarapu, P. L., *Principles and Applications of Polarization-Division Interferometry*. Wiley: Chichester, UK, 1998.

69. Piprek, J.; Römer, F.; Witzigmann, B., On the uncertainty of the Auger recombination coefficient extracted from InGaN/GaN light-emitting diode efficiency droop measurements. *Applied Physics Letters* **2015,** *106* (10), 101101.

70. Li, S. S., *Semiconductor Physical Electronics*. Springer: New York, 2006; Vol. 2nd edd.

71. Piprek, J., Chapter 3 - Carrier Transport. In *Semiconductor Optoelectronic Devices*, Academic Press: Boston, 2003; pp 49-82.

72. Gfroerer, T. H.; Priestley, L. P.; Fairley, M. F.; Wanlass, M. W., Temperature dependence of nonradiative recombination in low-band gap InxGa1-xAs/InAsyP1-y double heterostructures grown on InP substrates. *J. Appl. Phys.* **2003,** *94* (3), 1738-1743.

73. Landsberg, P., *Recombination in Semiconductors*. Cambridge University Press: 1991.
74. Davies, J. H., *The Physics of Low-dimensional Semiconductors*. Cambridge University Press: 1997.
75. Varshni, Y. P., Band-to-Band Radiative Recombination in Groups IV, VI, and III-V Semiconductors (I). *physica status solidi (b)* **1967,** *19* (2), 459-514.
76. Keyes, R. W., The Electrical Properties of Black Phosphorus. *Physical Review* **1953,** *92* (3), 580-584.
77. Sorokina, I. T.; Vodopyanov, K. L., *Solid-state mid-infrared laser sources*. Springer Science & Business Media: 2003; Vol. 89.
78. Zhou, X.; Zhang, Q.; Gan, L.; Li, H.; Xiong, J.; Zhai, T., Booming Development of Group IV–VI Semiconductors: Fresh Blood of 2D Family. *Advanced Science* **2016,** *3* (12), 1600177.
79. Zhong, L.; Amber, M.; Natalie, B.; Shruti, S.; Kehao, Z.; Yifan, S.; Xufan, L.; Nicholas, J. B.; Hongtao, Y.; Susan, K. F.-S.; Alexey, C.; Hui, Z.; Stephen, M.; Aaron, M. L.; Kai, X.; Brian, J. L.; Marija, D.; James, C. M. H.; Jiwoong, P.; Manish, C.; Raymond, E. S.; Ali, J.; Mark, C. H.; Joshua, R.; Mauricio, T., 2D materials advances: from large scale synthesis and controlled heterostructures to improved characterization techniques, defects and applications. *2D Materials* **2016,** *3* (4), 042001.
80. Mak, K. F.; Shan, J., Photonics and optoelectronics of 2D semiconductor transition metal dichalcogenides. *Nature Photonics* **2016,** *10*, 216.
81. Niu, L.; Coleman, J. N.; Zhang, H.; Shin, H.; Chhowalla, M.; Zheng, Z., Production of Two-Dimensional Nanomaterials via Liquid-Based Direct Exfoliation. *Small* **2016,** *12* (3), 272-293.
82. Wenjing, Z.; Qixing, W.; Yu, C.; Zhuo, W.; Andrew, T. S. W., Van der Waals stacked 2D layered materials for optoelectronics. *2D Materials* **2016,** *3* (2), 022001.
83. Zhesheng, C.; Johan, B.; Abhay, S., Optimal light harvesting in 2D semiconductor heterostructures. *2D Materials* **2017,** *4* (2), 025115.
84. Choi, W.; Choudhary, N.; Han, G. H.; Park, J.; Akinwande, D.; Lee, Y. H., Recent development of two-dimensional transition metal

dichalcogenides and their applications. *Materials Today* **2017,** *20* (3), 116-130.

85. Ryder, C. R.; Wood, J. D.; Wells, S. A.; Hersam, M. C., Chemically Tailoring Semiconducting Two-Dimensional Transition Metal Dichalcogenides and Black Phosphorus. *ACS Nano* **2016,** *10* (4), 3900-3917.

86. Zeng, Z.; Yin, Z.; Huang, X.; Li, H.; He, Q.; Lu, G.; Boey, F.; Zhang, H., Single-Layer Semiconducting Nanosheets: High-Yield Preparation and Device Fabrication. *Angewandte Chemie International Edition* **2011,** *50* (47), 11093-11097.

87. Coleman, J. N.; Lotya, M.; O'Neill, A.; Bergin, S. D.; King, P. J.; Khan, U.; Young, K.; Gaucher, A.; De, S.; Smith, R. J.; Shvets, I. V.; Arora, S. K.; Stanton, G.; Kim, H.-Y.; Lee, K.; Kim, G. T.; Duesberg, G. S.; Hallam, T.; Boland, J. J.; Wang, J. J.; Donegan, J. F.; Grunlan, J. C.; Moriarty, G.; Shmeliov, A.; Nicholls, R. J.; Perkins, J. M.; Grieveson, E. M.; Theuwissen, K.; McComb, D. W.; Nellist, P. D.; Nicolosi, V., Two-Dimensional Nanosheets Produced by Liquid Exfoliation of Layered Materials. *Science* **2011,** *331* (6017), 568-571.

88. Sun, Y.; Cheng, H.; Gao, S.; Sun, Z.; Liu, Q.; Liu, Q.; Lei, F.; Yao, T.; He, J.; Wei, S.; Xie, Y., Freestanding Tin Disulfide Single-Layers Realizing Efficient Visible-Light Water Splitting. *Angewandte Chemie International Edition* **2012,** *51* (35), 8727-8731.

89. Shibata, T.; Muranushi, Y.; Miura, T.; Kishi, T., Photoconductive properties of single-crystal 2H-SnS2. *Journal of Physics and Chemistry of Solids* **1990,** *51* (11), 1297-1300.

90. Patil, S. G.; Tredgold, R. H., Electrical and photoconductive properties of SnS2 crystals. *Journal of Physics D: Applied Physics* **1971,** *4* (5), 718-722.

91. Burton, L. A.; Whittles, T. J.; Hesp, D.; Linhart, W. M.; Skelton, J. M.; Hou, B.; Webster, R. F.; O'Dowd, G.; Reece, C.; Cherns, D.; Fermin, D. J.; Veal, T. D.; Dhanak, V. R.; Walsh, A., Electronic and optical properties of single crystal SnS_2: an earth-abundant disulfide photocatalyst. *Journal of Materials Chemistry A* **2016,** *4* (4), 1312-1318.

92. Burton, L. A.; Colombara, D.; Abellon, R. D.; Grozema, F. C.; Peter, L. M.; Savenije, T. J.; Dennler, G.; Walsh, A., Synthesis,

Characterization, and Electronic Structure of Single-Crystal SnS, Sn_2S_3, and SnS_2. *Chemistry of Materials* **2013,** *25* (24), 4908-4916.

93. Powell, M. J.; Grant, A. J., The effect of pressure on the optical-absorption edge in SnS2 and SnSe2. *Il Nuovo Cimento B (1971-1996)* **1977,** *38* (2), 486-495.

94. Shafique, A.; Samad, A.; Shin, Y.-H., Ultra low lattice thermal conductivity and high carrier mobility of monolayer SnS_2 and $SnSe_2$: a first principles study. *Physical Chemistry Chemical Physics* **2017,** *19* (31), 20677-20683.

95. Szczech, J. R.; Higgins, J. M.; Jin, S., Enhancement of the thermoelectric properties in nanoscale and nanostructured materials. *Journal of Materials Chemistry* **2011,** *21* (12), 4037-4055.

96. Tan, F.; Qu, S.; Zeng, X.; Zhang, C.; Shi, M.; Wang, Z.; Jin, L.; Bi, Y.; Cao, J.; Wang, Z.; Hou, Y.; Teng, F.; Feng, Z., Photovoltaic effect of tin disulfide with nanocrystalline/amorphous blended phases. *Solid State Communications* **2010,** *150* (1), 58-61.

97. Zhuang, H. L.; Hennig, R. G., Theoretical perspective of photocatalytic properties of single-layer SnS2. *Physical Review B* **2013,** *88* (11), 115314.

98. Huang, Y.; Sutter, E.; Sadowski, J. T.; Cotlet, M.; Monti, O. L. A.; Racke, D. A.; Neupane, M. R.; Wickramaratne, D.; Lake, R. K.; Parkinson, B. A.; Sutter, P., Tin Disulfide—An Emerging Layered Metal Dichalcogenide Semiconductor: Materials Properties and Device Characteristics. *ACS Nano* **2014,** *8* (10), 10743-10755.

99. Ram, B.; Singh, A. K., Strain-induced indirect-to-direct band-gap transition in bulk SnS_2. *Physical Review B* **2017,** *95* (7), 075134.

100. Song, H. S.; Li, S. L.; Gao, L.; Xu, Y.; Ueno, K.; Tang, J.; Cheng, Y. B.; Tsukagoshi, K., High-performance top-gated monolayer SnS2 field-effect transistors and their integrated logic circuits. *Nanoscale* **2013,** *5* (20), 9666-9670.

101. Gowers, J. P.; Lee, P. A., Mobility of electrons in SnS2 single crystals. *Solid State Communications* **1970,** *8* (18), 1447-1449.

102. Gonzalez, J. M.; Oleynik, I. I., Layer-dependent properties of SnS_2 and $SnSe_2$ two-dimensional materials. *Physical Review B* **2016,** *94* (12), 125443.

103. Bhaskar, P.; Achtstein, A. W.; Vermeulen, M. J. W.; Siebbeles, L. D. A., Charge Mobility and Recombination Mechanisms in Tellurium van der Waals Solid. *The Journal of Physical Chemistry C* **2018**.
104. Bhaskar, P.; Achtstein, A. W.; Vermeulen, M. J. W.; Siebbeles, L. D. A., Radiatively Dominated Charge Carrier Recombination in Black Phosphorus. *Journal of Physical Chemistry C* **2016,** *120* (25), 13836-13842.
105. Alig, R. C.; Bloom, S.; Struck, C. W., Scattering by ionization and phonon emission in semiconductors. *Physical Review B: Condensed Matter* **1980,** *22* (12), 5565-5582.
106. *Tin disulfide (SnS_2) band structure, energy gaps: Datasheet from Landolt-Börnstein - Group III Condensed Matter · Volume 41C: "Non-Tetrahedrally Bonded Elements and Binary Compounds I" in SpringerMaterials (https://dx.doi.org/10.1007/10681727_785)*, Springer-Verlag Berlin Heidelberg.
107. Coelho, R., *Physics of dielectrics for the engineer / Roland Coelho*. Elsevier Scientific Pub. Co., ; distributors for the U.S. and Canada, Elsevier/North-Holland: Amsterdam ; New York : New York, 1979.
108. Baerends, E. J.; Ziegler, T.; Atkins, A. J.; Autschbach, J.; Bashford, D.; Baseggio, O.; Bérces, A.; Bickelhaupt, F. M.; Bo, C.; Boerritger, P. M.; Cavallo, L.; Daul, C.; Chong, D. P.; Chulhai, D. V.; Deng, L.; Dickson, R. M.; Dieterich, J. M.; Ellis, D. E.; van Faassen, M.; Ghysels, A.; Giammona, A.; van Gisbergen, S. J. A.; Goez, A.; Götz, A. W.; Gusarov, S.; Harris, F. E.; van den Hoek, P.; Hu, Z.; Jacob, C. R.; Jacobsen, H.; Jensen, L.; Joubert, L.; Kaminski, J. W.; van Kessel, G.; König, C.; Kootstra, F.; Kovalenko, A.; Krykunov, M.; van Lenthe, E.; McCormack, D. A.; Michalak, A.; Mitoraj, M.; Morton, S. M.; Neugebauer, J.; Nicu, V. P.; Noodleman, L.; Osinga, V. P.; Patchkovskii, S.; Pavanello, M.; Peeples, C. A.; Philipsen, P. H. T.; Post, D.; Pye, C. C.; Ramanantoanina, H.; Ramos, P.; Ravenek, W.; Rodríguez, J. I.; Ros, P.; Rüger, R.; Schipper, P. R. T.; Schlüns, D.; van Schoot, H.; Schreckenbach, G.; Seldenthuis, J. S.; Seth, M.; Snijders, J. G.; Solà, M.; Stener, M.; Swart, M.; Swerhone, D.; te Velde, G.; Tognetti, V.; Vernooijs, P.; Versluis, L.; Visscher, L.; Visser, O.; Wang, F.; Wesolowski, T. A.; van Wezenbeek, E. M.; Wiesenekker, G.; Wolff, S. K.; Woo, T. K.; Yakovlev, A. L., ADF2017, SCM,

Theoretical Chemistry, Vrije Universiteit, Amsterdam, The Netherlands, https://www.scm.com.
109. te Velde, G.; Bickelhaupt, F. M.; Baerends, E. J.; Fonseca Guerra, C.; van Gisbergen, S. J. A.; Snijders, J. G.; Ziegler, T., Chemistry with ADF. *Journal of Computational Chemistry* **2001,** *22* (9), 931-967.
110. Fonseca Guerra, C.; Snijders, J. G.; te Velde, G.; Baerends, E. J., Towards an order-N DFT method. *Theoretical Chemistry Accounts* **1998,** *99* (6), 391-403.
111. Hall, R. N., Recombination Processes in Semiconductors. *Proceedings of the IEE - Part B: Electronic and Communication Engineering* **1959,** *106* (17), 923-931.
112. Lakhwani, G.; Rao, A.; Friend, R. H., Bimolecular Recombination in Organic Photovoltaics. *Annual Review of Physical Chemistry* **2014,** *65* (1), 557-581.
113. Tin disulfide (SnS_2) optical properties, dielectric constants. In *Non-Tetrahedrally Bonded Elements and Binary Compounds I*, Madelung, O.; Rössler, U.; Schulz, M., Eds. Springer Berlin Heidelberg: Berlin, Heidelberg, 1998; pp 1-11.
114. Schatz, G. C.; Ratner, M. A., Quantum mechanics in chemistry. **2002**.
115. Nicolosi, V.; Chhowalla, M.; Kanatzidis, M. G.; Strano, M. S.; Coleman, J. N., Liquid Exfoliation of Layered Materials. *Science* **2013,** *340* (6139).
116. Xiao, C.; Zhao, G.; Zhang, A.; Jiang, W.; Janssen, R. A. J.; Li, W.; Hu, W.; Wang, Z., High Performance Polymer Nanowire Field-Effect Transistors with Distinct Molecular Orientations. *Advanced Materials* **2015,** *27* (34), 4963-4968.
117. Briseno, A. L.; Mannsfeld, S. C. B.; Jenekhe, S. A.; Bao, Z.; Xia, Y., Introducing organic nanowire transistors. *Materials Today* **2008,** *11* (4), 38-47.
118. Zhou, Y.; Lei, T.; Wang, L.; Pei, J.; Cao, Y.; Wang, J., High-Performance Organic Field-Effect Transistors from Organic Single-Crystal Microribbons Formed by a Solution Process. *Advanced Materials* **2010,** *22* (13), 1484-1487.

119. Grozema, F. C.; Hoofman, R. J. O. M.; Candeias, L. P.; de Haas, M. P.; Warman, J. M.; Siebbeles, L. D. A., The Formation and Recombination Kinetics of Positively Charged Poly(phenylene vinylene) Chains in Pulse-Irradiated Dilute Solutions. *J. Phys. Chem. A* **2003,** *107* (31), 5976-5986.
120. Grozema, F. C.; Siebbeles, L. D. A., Charge Mobilities in Conjugated Polymers Measured by Pulse Radiolysis Time-Resolved Microwave Conductivity: From Single Chains to Solids. *Journal of Physical Chemistry Letters* **2011,** *2* (23), 2951-2958.
121. Krahne, R.; Morello, G.; Figuerola, A.; George, C.; Deka, S.; Manna, L., Physical properties of elongated inorganic nanoparticles. *Phys. Rep.* **2011,** *501* (3–5), 75-221.
122. V. S. Minaev, V. S.; Timoshenkova, S. P.; Kalugina, V. V., Structural and Phase Transformations in Condensed Selenium. *Journal of Optoelectronics and Advanced Materials* **2005,** *7* (4), 1717-1741.
123. Tutihasi, S.; Chen, I., Optical Properties and Band Structure of Trigonal Selenium. *Physical Review* **1967,** *158* (3), 623-630.
124. Treusch, J.; Sandrock, R., Energy Band Structures of Selenium and Tellurium (Kohn-Rostoker Method). *physica status solidi (b)* **1966,** *16* (2), 487-497.
125. Mort, J., Acoustoelectric Current Saturation in Trigonal Selenium. *Physical Review Letters* **1967,** *18* (14), 540-543.
126. Mort, J., Transient Photoconductivity in Trigonal Selenium Single Crystals. *Journal of Applied Physics* **1968,** *39* (8), 3543-3549.
127. Mell, H.; Stuke, J., Magnetoconductivity of hexagonal selenium single crystals. *Physics Letters* **1966,** *20* (3), 222-224.
128. Weiser, G.; Stuke, J., Electroreflectance on Trigonal Selenium. *physica status solidi (b)* **1971,** *45* (2), 691-703.
129. Prins, P.; Grozema, F. C.; Schins, J. M.; Patil, S.; Scherf, U.; Siebbeles, L. D. A., High Intrachain Hole Mobility on Molecular Wires of Ladder-Type Poly(p-Phenylenes). *Physical Review Letters* **2006,** *96* (14), 146601.
130. Poborchii, V. V.; Kolobov, A. V.; Caro, J.; Zhuravlev, V. V.; Tanaka, K., Dynamics of Single Selenium Chains Confined in One-Dimensional Nanochannels of AlPO4-5: Temperature Dependencies of the

First- and Second-Order Raman Spectra. *Physical Review Letters* **1999,** *82* (9), 1955-1958.
131. Poborchii, V. V.; Kolobov, A. V.; Caro, J.; Zhuravlev, V. V.; Tanaka, K., Polarized Raman spectra of selenium species confined in nanochannels of AlPO4-5 single crystals. *Chemical Physics Letters* **1997,** *280* (1), 17-23.
132. Movaghar, B.; Sauer, G. W.; Würtz, D.; Huber, D. L., Time decay of excitations in the one dimensional trapping problem. *Solid State Communications* **1981,** *39* (11), 1179-1182.
133. Movaghar, B.; Grünewald, M.; Pohlmann, B.; Würtz, D.; Schirmacher, W., Theory of hopping and multiple-trapping transport in disordered systems. *Journal of Statistical Physics* **1983,** *30* (2), 315-334.
134. Chenxi, Z.; Cheng, G.; Yifan, N.; Kyung-Ah, M.; Chaoping, L.; Young Jun, O.; Hengji, Z.; Weihua, W.; Suklyun, H.; Luigi, C.; Robert, M. W.; Kyeongjae, C., Systematic study of electronic structure and band alignment of monolayer transition metal dichalcogenides in Van der Waals heterostructures. *2D Materials* **2017,** *4* (1), 015026.
135. Yu, X.; Sivula, K., Layered 2D semiconducting transition metal dichalcogenides for solar energy conversion. *Current Opinion in Electrochemistry* **2017,** *2* (1), 97-103.
136. Hulin, M., Electron band structure of tellurium. *Journal of Physics and Chemistry of Solids* **1966,** *27* (2), 441-449.
137. Lutz, M.; Stolze, H.; Grosse, P., The Masses of Free Holes and Electrons in Tellurium. *physica status solidi (b)* **1974,** *62* (2), 665-675.
138. Tutihasi, S.; G. Roberts, G.; C. Keezer, R.; E. Drews, R., *Optical Properties of Tellurium in the Fundamental Absorption Region*. 1969; Vol. 177, p 1143-1150.
139. Bondar, V. M.; Radchenko, V. S.; Solonchuk, L. S., Conductivity of Warm Holes in Tellurium. *physica status solidi (b)* **1978,** *87* (2), K97-K100.
140. Bohmeyer, W.; Hoerstel, W., Hall effect in p-tellurium at high electric fields. *physica status solidi (a)* **1977,** *41* (1), K27-K30.

141. Hoerstel, W.; Kusnick, D.; Spitzer, M., High-field transport and low-field mobility in tellurium single crystals. *physica status solidi (b)* **1973,** *60* (1), 213-221.
142. Nimtz, G.; Seeger, K., Current Controlled Negative Differential Resistivity of P-type Tellurium. *Applied Physics Letters* **1969,** *14* (1), 19-21.
143. Peng, H.; Kioussis, N.; Snyder, G. J., Elemental tellurium as a chiral p-type thermoelectric material. *Physical Review B* **2014,** *89* (19), 195206.
144. Zhou, G.; Addou, R.; Wang, Q.; Honari, S.; Cormier, C. R.; Cheng, L.; Yue, R.; Smyth, C. M.; Laturia, A.; Kim, J.; Vandenberghe, W. G.; Kim, M. J.; Wallace, R. M.; Hinkle, C. L., High-Mobility Helical Tellurium Field-Effect Transistors Enabled by Transfer-Free, Low-Temperature Direct Growth. *Advanced Materials* **2018,** *30* (36), 1803109.
145. Boyd, R. W., *Radiometry and the detection of optical radiation*. Wiley: 1983.
146. Bethe, H.; Heitler, W., On the stopping of fast particles and on the creation of positive electrons. *Proceedings of the Royal Society of London. Series A* **1934,** *146* (856), 83-112.
147. Bethe, H.; Hund, F.; Mott, N. F.; Pauli, W.; Rubinowicz, A.; Wentzel, G.; Smekal, A., *Quantentheorie*. Springer-Verlag Berlin Heidelberg: 1933.
148. Report 16. *Journal of the International Commission on Radiation Units and Measurements* **1970,** *os9* (1), 1-51.
149. Mozumder, A., Chapter 2 - Interaction of Radiation with Matter: Energy Transfer from Fast Charged Particles. In *Fundamentals of Radiation Chemistry*, Mozumder, A., Ed. Academic Press: San Diego, 1999; pp 5-39.
150. Hoofman, R. J. O. M.; Siebbeles, L. D. A.; de Haas, M. P.; Hummel, A.; Bloor, D., Anisotropy of the charge-carrier mobility in polydiacetylene crystals. *J. Chem. Phys.* **1998,** *109* (5), 1885-1893.
151. Infelta, P. P.; de Haas, M. P.; Warman, J. M., The study of the transient conductivity of pulse irradiated dielectric liquids on a nanosecond

timescale using microwaves. *Radiation Physics and Chemistry* **1977,** *10* (5), 353-365.
152. Piprek, J., Chapter 1 - Introduction to Semiconductors. In *Semiconductor Optoelectronic Devices*, Academic Press: Boston, 2003; pp 3-11.
153. Berberan-Santos, M. N.; Bodunov, E. N.; Valeur, B., Mathematical functions for the analysis of luminescence decays with underlying distributions 1. Kohlrausch decay function (stretched exponential). *Chemical Physics* **2005,** *315* (1–2), 171-182.
154. Dicker, G.; de Haas, M. P.; de Leeuw, D. M.; Siebbeles, L. D. A., Origin of the stretched-exponential hole relaxation in regioregular poly(3-hexylthiophene). *Chemical Physics Letters* **2005,** *402* (4), 370-374.
155. Dicker, G.; de Haas, M. P.; Warman, J. M.; de Leeuw, D. M.; Siebbeles, L. D. A., The Disperse Charge-Carrier Kinetics in Regioregular Poly(3-hexylthiophene). *Journal of Physical Chemistry B* **2004,** *108* (46), 17818-17824.
156. Pfister, G.; Scher, H., Dispersive (non-Gaussian) transient transport in disordered solids. *Advances in Physics* **1978,** *27* (5), 747-798.
157. Silver, M.; Schoenherr, G.; Baessler, H., Dispersive Hopping Transport from an Exponential Energy Distribution of Sites. *Physical Review Letters* **1982,** *48* (5), 352-355.
158. Schnörer, H.; Haarer, D.; Blumen, A., Crossover from dispersive to nondispersive transport in a trap-controlled hopping model. *Physical Review B* **1988,** *38* (12), 8097-8101.
159. Gfroerer, T. H.; Priestley, L. P.; Fairley, M. F.; Wanlass, M. W., Temperature dependence of nonradiative recombination in low-band gap InxGa1-xAs/InAsyP1-y double heterostructures grown on InP substrates. *J. Appl. Phys.* **2003,** *94* (3), 1738-1743.
160. Wang, Y.; Qiu, G.; Wang, R.; Huang, S.; Wang, Q.; Liu, Y.; Du, Y.; Goddard, W. A.; Kim, M. J.; Xu, X.; Ye, P. D.; Wu, W., Field-effect transistors made from solution-grown two-dimensional tellurene. *Nature Electronics* **2018,** *1* (4), 228-236.
161. Cheng, L.; Liu, Y., What Limits the Intrinsic Mobility of Electrons and Holes in Two Dimensional Metal Dichalcogenides? *Journal of the American Chemical Society* **2018**.

162. Young, K. F.; Frederiske, H. P. R., Compilation of the Static Dielectric Constant of Inorganic Solids. *Journal of Physical and Chemical Reference Data* **1973,** *2* (2), 313-409.

Summary

This doctoral thesis reports studies on effects of temperature and density on the mobility and recombination dynamics of charge carriers in low-dimensional van der Waals materials.

Chapter 2. In this chapter we studied mobility and decay dynamics of charge carriers in two-dimensional black phosphorus (BP) using contactless microwave conductivity technique. A global analysis scheme is used to reveal the impact of radiative second-order decay and the presence of intrinsic carriers in BP. The combined electron and hole mobilities in BP increases at low temperatures with temperature due to ionized impurity scattering, and after reaching a maximum near 250 K it drops to about half the maximum value due to deformation potential scattering. The rate coefficients for second-order radiative recombination and for non-radiative Shockey-Read-Hall (SRH) recombination are found to decrease with temperature. Non-radiative third-order Auger recombination is negligible for the studied densities of excess electron-hole pairs. For densities of 2.5×10^{17} cm^{-3} a major fraction (78 %) of the excess electrons and holes undergo radiative recombination. For higher excess charge densities on the order of 10^{18} cm^{-3} electron-hole recombination is expected to occur with near unity radiative yield. This makes BP an interesting material for efficient infrared emitter devices like LEDs or lasers around 4 μm.

Chapter 3. In this chapter, we studied charge carrier mobility and their decay dynamics in another two-dimensional material, tin disulfide (SnS_2), which is an indirect semiconductor. We found that the mobility of charge carriers of type 1 is 70 ± 12 $\mathrm{cm}^2\mathrm{V}^{-1}\mathrm{s}^{-1}$ and of the opposite charges it is 123 ± 12 $\mathrm{cm}^2\mathrm{V}^{-1}\mathrm{s}^{-1}$. The decrease of the mobility at higher temperature is typical for a band-like transport mechanism. Theoretical analysis of the charge carrier decay kinetics reveals that electron-hole recombination occurs by thermal promotion of electrons from the indirect to the direct band gap, followed by radiative recombination. Phonon assisted recombination via the indirect band gap is found to be negligible.

Chapter 4. In this chapter, we studied the mobility and decay dynamics of charge carriers in trigonal selenium (Se), which is a one-dimensional van der Waals material. The one-dimensional mobility of charge carriers along helical chains of Se in the trigonal phase is at least ca. 0.5 $\mathrm{cm}^2\mathrm{V}^{-1}\mathrm{s}^{-1}$ at room temperature, which

is promising for application in nanoelectronics. In addition, the fact that Se is a van der Waals solid offers prospects for large-scale production of isolated chains or bunches *via* liquid exfoliation.

Chapter 5. In this chapter, we studied mobility and charge carrier decay dynamics in one-dimensional tellurium (Te) van der Waals material. The mobility of charges in Te is thermally deactivated with a room temperature value of 190 ± 20 $cm^2V^{-1}s^{-1}$. Charges decay with near unity quantum yield *via* radiative recombination. Te, being a quasi one-dimensional van der Waals material, has a potential for in-depth studies of interesting optoelectronic properties with isolated atomic chains. Such chains can in principle be obtained by liquid exfoliation, which offers possibilities for large-scale production. Furthermore, the appreciably high mobility, near unity radiative yield opens the potential for applications in nanoelectronics like as efficient far infrared detectors with high bandwidth or lasers with high efficiency. Further, far infrared imaging applications replacing micro bolometers may be of interest.

Samenvatting

Dit proefschrift rapporteert studies aan effecten van temperatuur en dichtheid op de mobiliteit en recombinatiedynamica van ladingsdragers in laag-dimensionale van der Waals materialen.

Hoofdstuk 2. In dit hoofdstuk hebben we de mobiliteit en vervaldynamica van ladingsdragers in tweedimensionaal zwart fosfor bestudeerd met behulp van een contactloze microgolfgeleidbaarheidstechniek. Door middel van theoretische analyses werd de importantie van radiatieve landingsrecombinatie en aanwezigheid van intrinsieke ladingsdragers bepaald. De som van de elektron en gat mobiliteiten zijn thermisch geactiveerd bij lage temperaturen als gevolg van verstrooiïng aan defecten. Na het bereiken van een maximale mobiliteit bij 250 K daalt deze tot ongeveer de helft van de maximumwaarde als gevolg van deformatiepotentiaalverstrooiïng. De snelheidscoëfficiënten voor tweede-orde radiatieve recombinatie en voor stralingsloze Shockey-Read-Hall recombinatie dalen met de temperatuur. Derde-orde Auger-recombinatie is verwaarloosbaar voor de bestudeerde dichtheden van elektron-gat paren. Voor dichtheden van 2.5×10^{17} cm^{-3} recombineert een grote fractie (78%) van de elektronen en gaten radiatief. Voor hogere ladingsdichtheden in de orde van 10^{18} cm^{-3} wordt verwacht dat elektron-gat recombinatie bijna 100% radiatief optreedt. Dit maakt zwarte fosfor een interessant materiaal voor efficiënte infrarood-emitter-apparaten zoals LED's of lasers werkend bij een golflengte nabij $4\ \mu\mathrm{m}$.

Hoofdstuk 3. In dit hoofdstuk hebben we de mobiliteit van ladingsdragers en hun vervaldynamiek bestudeerd in het tweedimensionale materiaal tindisulfide (SnS_2), een indirecte halfgeleider. We vonden dat de mobiliteit van één van de ladingsdragers gelijk is aan 70 ± 12 $\mathrm{cm}^2\mathrm{V}^{-1}\mathrm{s}^{-1}$ en van de tegengestelde ladingen is deze 123 ± 12 $\mathrm{cm}^2\mathrm{V}^{-1}\mathrm{s}^{-1}$. De afname van de mobiliteit bij hogere temperaturen is typisch voor een bandachtig transportmechanisme. Theoretische analyse van de vervalkinetiek van de ladingsdragers laat zien dat elektron-gat recombinatie plaatsvindt door thermische excitatie van elektronen van de indirecte naar de directe band gap, gevolgd door radiatieve recombinatie. De fonon-geassisteerde recombinatie via de indirecte band gap is te verwaarlozen.

Hoofdstuk 4. In dit hoofdstuk hebben we de mobiliteit en vervaldynamica van ladingsdragers in trigonaal selenium (Se) bestudeerd. Dit is een ééndimensionaal

van der Waals materiaal. De ééndimensionale mobiliteit van ladingsdragers langs helische ketens van Se in de trigonale fase is minstens $0.5\ \mathrm{cm^2V^{-1}s^{-1}}$ bij kamertemperatuur, hetgeen veelbelovend is voor toepassing in nano-elektronica. Daarnaast biedt het feit dat Se een van der Waals material is, perspectieven voor grootschalige productie van geïsoleerde ketens of bundels *via* exfoliatie in een oplosmiddel.

Hoofdstuk 5. In dit hoofdstuk hebben we de mobiliteit en de vervaldynamica van ladingdragers in het ééndimensionaal tellurium (Te) van der Waals materiaal bestudeerd. De mobiliteit van ladingen in Te is thermisch gedeactiveerd met een waarde van $190 \pm 20\ \mathrm{cm^2V^{-1}s^{-1}}$ bij kamertemperatuur. Ladingsdragers vervallen met bijna 100% efficiëntie *via* radiatieve recombinatie. Een quasi-ééndimensionaal van der Waals materiaal toont potentie voor diepgaande studies aan de opto-elektronische eigenschappen van geïsoleerde atomaire ketens. Dergelijke ketens kunnen in principe worden verkregen door exfoliatie in een oplosmiddel, hetgeen mogelijkheden biedt voor grootschalige productie. Verder biedt de aanzienlijk hoge mobiliteit en efficiënte radiatieve recombinatie mogelijkheden voor toepassingen in nano-elektronica, zoals efficiënte verre infrarooddetectoren met hoge bandbreedte of lasers met hoog rendement. Daarnaast kan Te interessant zijn voor verre infrarood beeldvormingstoepassingen ter vervanging van microbolometers.

Acknowledgments

It has been more than four wonderful years since I first came to the Netherlands to pursue my doctoral studies in the group of Optoelectronic Materials Section at TU Delft. I feel being privileged to be a part of such a diverse and scientifically-engaged group. I have had a great time being in the group with so many friendly people being around.

First and foremost, I am grateful to my promoter Prof. Laurens Siebbeles for giving me such a wonderful and covetous opportunity to be a part of his research group. Laurens, thank you for constantly providing your invaluable guidance and support to me throughout my doctoral research. This thesis would not have been possible without your expert supervision. I learnt a lot from you scientifically and personally. Thank you for being a lenient, understandable, cooperative and friendly supervisor. I would also like to thank my co-promoter Dr. Ferdinand Grozema for teaching me computation chemistry. Ferdinand, thank you for sharing your expert knowledge on PR-TRMC technique and computation chemistry with me. Thank you for clearing my doubts on PR-TRMC technique and your kind support at times.

I am very thankful to Dr. Alexander Achtstein for being a wonderful daily supervisor. Alexander, I am very grateful to be able to collaborate with you, till the end of my doctoral research. Sincere appreciation for teaching me, discussing with me and for clearing my doubts during my doctoral research. You always helped me with your great ideas and solutions for diverse problems, be it scientific, analytical or even managerial. Thank you for your timely support and expert advice.

Further, I would like to thank Ing. Martien Vermeulen, for being a very friendly colleague throughout my doctoral research. Martien, I have learnt a lot from you. You are a very engaging teacher in addition to an outstanding engineer. You were always ready to explain to me things I could not grasp easily. Thank you for being cooperative and patient with me. I will always miss talking to you and miss to hear your experiences about motorsport/dirt-biking and your grandkids. Thank you for being a nice friend and please convey my thanks to Ms. Corrie Vermeulen too.

I would also like to extend my sincere gratitude to Prof. John Warman and Prof. Lee Luthjens for sharing stories about the van de Graaff electron accelerator and past practices with me. Sincere thanks to Ing. Marinus Hom and Ing. Wybe Roodhuyzen for helping me carrying out experiments at times. Sincere gratitude to Ing. John Suijkerbuijk and Ing. Jos Thieme for technical support.

I am grateful to Ing. Ruben Abellon for helping me out directly and indirectly throughout my doctoral research. Ruben, thank you for your thoughtful advice on various subjects. I have learnt a lot from you. Thank you for introducing me to various experimental infrastructures available in our laboratories. Thank you for helping me with chemicals and ordering them for me. I enjoyed assisting the PBV courses with you and of course talking with you every now and then.

I am thankful to Dr. Arjan Houtepan for explaining the TA setup to me. I would like to extend my gratitude to Dr. Tom Savijne for clarifying TRMC doubts at times. Sincere thanks to Dr. Silke Diedenhofen, Dr. Wiel Evers, Mr. Aditya Kulkarni for helping me carrying out TA and THz experiments. I would like to thank Dr. Wiel Evers, Prof. Mikhail Artemyev, Ms. Relinde Moes for providing colloidal samples for my preliminary experiments during the first two years. I would like to acknowledge Dr. Ferdinand Grozema and Dr. Nicolas Renaud for helping me learn DFT calculations.

I would like to thank Aditya, Hamit, Frank, Gianluca, Lucas, Simon, Jence and Indy for being wonderful officemates. Further, I would like to equally thank my colleagues Yu Bi, Francesca, Dengyang, Maria, Solrun, Cansel, Davide, Magnus, Ryan, Jannika, Ward, Jaco, Nick, Mikhele, Valentina, Sourav and Deepika. Furthermore, sincere gratitude to Cecilia and Wil for being so proactive and helpful in administrative tasks.

I would like to extend my special thanks to Somil, Aditya, Ravi, Swasti, Damla, Hamit, Kevin, Rajeev, Sourav, Deepika, Sumit, Birbal, Rishabh, Chirag, Himanshu, Muzaffar, Amol, Aashish, Rama and Sumit for being good and fun-loving friends. Thank you Neha, Somil, Sravani, Aditya, Ravi, Muzaffar, Amol and Himanshu for planning and executing memorable cross-country road-trips. I would like to thank Joyce for helping me find a flexible accommodation during the final months of my doctoral research. Further, I would like to extend my gratitude to Daan, Danny and Santusha for being nice landlords.

My most special gratitude goes to my papa and mummy, my sisters and brothers-in-law and my wife for always motivating me and providing me with their endless support. Ansh, Sanvi and Shrey, thank you for bringing a smile on my face with your innocent activities.

At last, my heartily thanks to all the OM group members for being around, helping me directly or indirectly in the duration of November 2014 to February 2019.

Year 2015

Year 2017

Year 2018

List of Publications

1. **P. Bhaskar**, A. W. Achtstein, M. J. W. Vermeulen, L. D. A. Siebbeles. "Unconventional Thermally Activated Indirect to Direct Radiative Recombination of Electrons and Holes in Tin Disulfide Two-Dimensional Van der Waals Material" Journal of Physical Chemistry C, **2019**, Article ASAP, DOI:10.1021/acs.jpcc.9b01842

2. **P. Bhaskar**, A. W. Achtstein, M. J. W. Vermeulen, L. D. A. Siebbeles. "*Charge Mobility and Recombination Mechanisms in Tellurium van der Waals Solid"* Journal of Physical Chemistry C, **2019**, 123, 841-847

3. **P. Bhaskar**, A. W. Achtstein, S. L. Diedenhofen, L. D. A. Siebbeles. "*Mobility and Decay Dynamics of Charge Carriers in One-Dimensional Selenium van der Waals Solid*" Journal of Physical Chemistry C, **2017**, 121, 18917-18921

4. **P. Bhaskar**, A. W. Achtstein, M. J. W. Vermeulen, L. D. A. Siebbeles. "*Radiatively Dominated Charge Carrier Recombination in Black Phosphorus"* Journal of Physical Chemistry C, **2016**, 120, 13836-13842

Biography

Prashant Bhaskar was born on 18th of January 1991, in Patna, India. After his senior secondary education at the Birla School in Pilani, he attended his bachelor's and master's education at the India Institute of Science Education and Research (IISER), Pune during 2009 to 2014. At IISER, he pursued his bachelor's and master's studies in basic sciences for five years and graduated with BS-MS dual degree with a major in Physics. During his bachelor's research, he worked on radio-astronomy, where he studied solar radiation using a two-element interferometer under the supervision of Dr. Prasad Subramanian. The project was under an outreach program by the International Heliophysical Year of the UN and Indian Institute of Astrophysics, Bangalore. During his master's education, he got fascinated with the nanomaterials and took up a project on synthesis and characterization of zinc oxide nanorods under the supervision of Prof. Sulabha Kulkarni. In the final year of his master's, he worked on chemical conjugation of gold nanorods (Au) and cadmium tellurite (CdTe) nanorods to study exciton-plasmon coupling in the Au-CdTe heterostructures. In parallel, he also worked on self-assembly of gold nanorods to study enhanced sensitivity of molecules at attomolar concentration using Raman spectroscopy. In the year 2014, he started his PhD in the group of Prof. Laurens Siebbeles, to study the recombination dynamics and mobility of charges in low-dimensional van der Waals materials.